Characterization of Mechanical and Perceptual Properties of the Human To Improve the Design of Wearable Devices

Gaurav Mukherjee

A dissertation
submitted in partial fulfillment of the
requirements for the degree of

Doctor of Philosophy

University of Washington

2020

Reading Committee:

Eric Rombokas, Co-Chair

Patrick M. Aubin, Co-Chair

Santosh Devasia

Brian C. Fabien

Program Authorized to Offer Degree:

Mechanical Engineering

University of Washington

Abstract

Characterization of Mechanical and Perceptual Properties of the Human To Improve the Design of Wearable Devices

Gaurav Mukherjee

Co-Chairs of the Supervisory Committee:

Eric Rombokas, Co-Chair

Patrick M. Aubin, Co-Chair

Mechanical Engineering

Although wearable devices are rapidly improving in features and ability, their performance and comfort remain poor when they are coupled to the wearer. Issues such as poor anchoring between the device and the body, inefficient power transfer, and variability in perception of haptic cues are some examples. Traditionally, these issues at the human device interface (HDI) are addressed by coupling the device to the body with higher pressure, by adding degrees of freedom to the device, and by implementing active feedback control of the device. However, actions taken to mitigate the issues at the HDI give rise to more challenges. For instance, tightening the device to the body increases discomfort due to pressure. Adding measures such as redundant degrees of freedom, and active control makes the device design more complicated, increases power requirements, and ultimately makes the device bulky. In summary, these device-centered approaches are unsuccessful in mitigating issues of performance and comfort for wearable devices. In this dissertation, we focus on understanding the other half of this coupling problem - The Human. We characterize the mechanical and sensory properties of the tissue structures at the HDI, and we demonstrate that measuring these

human properties allows us to improve the design of wearable devices to deliver optimized performance and comfort.

- Experiment 1: By measuring the MCP torque, we discover that anthropometric measures explain differences previously attributed to sex.
- Experiment 2: Measuring the hand dorsum stiffness distribution enabled the design of a novel HDI with improved comfort and performance.
- Experiment 3: Characterizing the stiffness and mechanical impedance about the wrist helped quantify the effect of coupling pressure at the HDI.
- Experiment 4: Characterizing the mechanical impedance and detection threshold led to the discovery that describing detection threshold in power units accounts for the effects due to coupling pressure and reduces the complexity of haptic display design.
- Experiment 5: By changing the mechanical impedance of the HDI, we discovered that we can change the detectability of a vibrotactile stimulus.

This dissertation contributes to a fundamental enrichment of our knowledge of the mechanical and perceptual properties of the human body aimed at improving the design of wearable devices. The design of the HDI has thus far been a qualitative effort, where parameters like the softness of the HDI and the coupling pressure are adjusted in iterative fashion. This dissertation quantifies the mechanical and perceptual properties that are necessary for a quantitative design of the HDI, and demonstrates how this information can be used to optimize HDI design. Specifically, this dissertation demonstrates how describing the performance of a haptic display in terms of mechanical power can simplify the design process for a wearable vibrotactile display. It also quantitatively describes the inverse relationship between comfort and performance at the HDI.

This work lays the foundation for the design of the human device interfaces of the future.

For instance, VR/AR applications require the design of physical interfaces that heighten our experience of realism. To do this we must amplify our abilities to discern subtle haptic stimuli applied to our body, while attenuating parasitic forces that threaten to destroy this experience. In prosthetic devices and exoskeletons, the advent of impedance and stiffness matched surfaces will revolutionize comfort, while heightening the sensory experience by transmitting afferent stimuli from the artificial peripheral device to the body interface. Finally, as actuators and sensors become less stiff and more conformal, the knowledge of the properties of the human body will become critical in optimizing performance of the wearable device. This work is the beginning of the next revolution in the human sensory experience.

TABLE OF CONTENTS

LIST OF FIGURES

LIST OF TABLES

Table Number Page

GLOSSARY

HDI: Human Device Interface

MCP: Metacarpophalangeal

PIP: Proximal Inter-Phalangeal

DIP: Distal Inter-Phalangeal

EMG: Electromyogram

DT: Detection Threshold

D-83: Shore Hardness Scale D with a durometer 83

A-30: Shore Hardness Scale A with a durometer 30

OO-30: Shore Hardness Scale OO with a durometer 30

ACKNOWLEDGMENTS

To the Giants whose shoulders I stand upon.

I thank my doctoral supervisory committee for helping focus this dissertation and my thoughts in the process. To my advisors, Dr. Eric Rombokas and Dr. Patrick Aubin - It turns out that the most enriching meeting that I took during the visit days of 2014 was with you. Thank you for patiently shepharding my endeavors and for demonstrating that the PhD process can be fun and exciting! This journey would have been literally impossible without your support.

I thank the Department of Mechanical Engineering at the University of Washington for housing my academic dreams and pursuits for over half a decade, while I explored the many different paths to find my own. My deepest thanks to the University of Washington Institute of Neuroengineering (UWIN) for their incredible support of my research through a Graduate Research Fellowship. Specifically, I'd like to thank Dr. Kat Steele, Dr. Tom Daniels, and Dr. Alison Mehravari for making the Fellowship experience pivotal to my growth as an individual, and as a Scientist. A big thanks to the Center for Limb Loss and Mobility (CLiMB) at the VA RR D for including me in their enthusiastic and supportive community of scientists and engineers.

I would like to thank Facebook Reality Labs for their incredible support of my work over the last three years. A dissertation bridging such vast and deep individual topics would be impossible without the conversations I had with the many experts there. In particular, I would like to thank Dr. Raymond King and Dr. Ali Israr for their steadfast belief, enthusiasm and support of my work.

I would also like to thank Dr. Robert Winglee and the folks at the Northwest Earth and Space Science Pipeline (NESSP) for including me in their work of building bridges with the local communities of the Pacific Northwest. My experience of working alongside you has left deep impressions about the work needed to lower the barriers for access to education for all. Thank you for mentoring me and for implicitly supporting my scholarship.

I would also like to thank the Center for Neurotechnology, and Dr. Eric Chudler specifically, for patiently engaging my many questions and curiosities. Eric, your enthusiasm for sharing the joys of Neuroscience and travel are extremely infectious. I am inspired by you to share this joy of learning with others in the future!

The best for last - I would like to thank my parents for their selfless sacrifices towards my wants and wishes. I cannot imagine having the luxury to study this far without you both toiling quietly in the background to make it so. Thank you for everything.

To Misha - *my moon*. Thank you for making me laugh every single day. You broaden my thoughts, far beyond the singular focus that my scientific work demands, and help me appreciate all of the diversity that this life has to offer. To a lifetime of adventures!

A big thanks to all my friends, mentors and extended family. Thank you for your contributions to this journey - a patient ear, a few precious words of encouragement, and the many excellent adventures!

DEDICATION

To my parents, Dr. Subhasish Mukherjee and Mrs. Chaitali Mukherjee. Your sacrifices and dedication fuel this endeavor and all of my endeavors.

Chapter 1

INTRODUCTION AND BACKGROUND

Although wearable devices are rapidly improving in features and ability, their performance and comfort remain poor when they are coupled to the wearer. Issues such as poor anchoring between the device and the body ([1, 2]), inefficient power transfer ([2]), and variability in perception of haptic cues ([]) are some examples. Traditionally, these issues at the human device interface (HDI) are addressed by coupling the device to the body with higher pressure, by adding degrees of freedom to the device, and by implementing active feedback control of the device. However, actions taken to mitigate the issues at the HDI give rise to more challenges. For instance, tightening the device to the body increases discomfort due to pressure. Adding measures such as redundant degrees of freedom, and active control makes the device design more complicated, increases power requirements, and ultimately makes the device bulky. In summary, these device-centered approaches are unsuccessful in mitigating issues of performance and comfort for wearable devices. In this dissertation, we focus on understanding the other half of this coupling problem - The Human. We characterize the mechanical and sensory properties of the tissue structures at the HDI, and we demonstrate that measuring these human properties allows us to improve the design of wearable devices to deliver optimized performance and comfort.

To optimize the performance and comfort of wearable devices, designs must incorporate knowledge about mechanical and perceptual properties of the human tissue at the HDI. For example, pressure at the HDI can be evenly distributed by uniformizing the overall stiffness across the HDI ([3]; [4]). This leads to better comfort and performance of the coupled wearable device. Similarly, the performance of vibrotactile haptic actuators can be amplified by matching the mechanical impedance of the actuator to the tissue ([5]). However, to apply these methods to improve the HDI design for hand and wrist-worn devices, we must first characterize the mechanical and perceptual properties of the human.

1.1 Organization of the dissertation

Chapter 2: In the first experiment, we quantify the torque required to extend the index finger about the MCP joint. We calculate torque from force and angles measured simultaneously from a custom arthrograph device. We discover that a difference in the torque required, previously attributed to sex ([6, 7]), is actually due to a difference between hand sizes. This finding allowed us to generate a single normative torque band which can be used by wearable designers as a quantitative reference for designing hand exoskeletons, and by clinicians to quantify hand function impairments.

Chapter 3: In the second experiment, we report the first ever measurement of stiffness distribution of the hand dorsum. By using a novel technique of generating stiffness gradients across locations, we improve comfort and performance at the HDI when an exoskeleton is coupled to the hand dorsum.

Chapter 4: In the third experiment, we report the first ever measurement of the stiffness and mechanical impedance at the wrist. In a first, we quantify the stiffness and mechanical impedance increase with increasing coupling pressure. However, this increase is more over the bone than over soft tissue rich areas, helping us understand why attaching wearables more tightly to the wrist causes discomfort.

Chapter 5: In the fourth experiment, we report the first ever quantification of mechanical impedance and vibrotactile sensitivity over bony and soft locations about the human wrist. We quantify, for the first time ever, how increasing coupling pressure over the wrist changes both the stiffness of the tissue as well as our sensitivity to vibration. We discover in a novel finding, that if we describe the vibrotactile sensitivity threshold in units of mechanical power, then the design of the HDI can be simplified, and parameters such as coupling pressure between the wearable device and the body do not need to be accounted for.

Chapter 6: In the fifth and final experiment, we demonstrate a novel approach to tuning comfort and our sensitivity to vibrations applied over the wrist. We change the mechanical impedance of the HDI and demonstrate quantitatively how our ability to perceive an applied vibration reduces as the HDI material gets softer. We also find that the softness of the HDI material correlates directly with the user's perceived comfort.

Chapter 7: In this last chapter, we summarize our results and argue for the necessity for broader measurements of the human body using the methods we use in this dissertation. We contextualize the utility of the properties of the human body studied here in the process of design, and end with a vision of how incorporating the human more closely in design, will help the human device interfaces evolve in the future.

Chapter 2

QUANTIFYING PASSIVE EXTENSION TORQUE ABOUT THE SECOND MCP TO IMPROVE FUNCTIONAL ASSESSMENT OF THE HAND

Gaurav Mukherjee[1], *Patrick Aubin*[1,2], *Katherine Steele*[1]
1. Department of Mechanical Engineering, University of Washington, Seattle, WA 98195, USA
2. Center for Limb Loss and Mobility (CLiMB), VA RR&D, Seattle, WA 98108, USA

2.1 Abstract

Stiffness of the joint is associated with impairment of function due to insult or injury. Quantifying joint stiffness may improve the diagnoses and treatment of diseases which result in hand function impairment. This research quantifies the passive extension torque about the second metacarpophalangeal (MCP) joint for twenty unimpaired right-handed individuals. The joint stiffness is compared between males and females, between both hands, and between the splinted and non-splinted finger. This research examines the role of anthropometric measures in explaining the observed inter-subject variability in the joint torque. Additionally, MCP joint stiffness for two individuals with hand paralysis from a long-term spinal cord injury of the C-6 vertebral level is compared to the normative joint torque data from the unimpaired individuals. This research characterizes the passive extension torques of the second MCP joint, examines the role of anthropometry in explaining the variance observed in the data, and provides a normative dataset for evaluating hand function quantitatively for different impairments of hand function, and to effectively design interventions.

2.2 Introduction

Impairments of the hand drastically impact an individual's ability to live independently. Neuromuscular injuries such as cerebral palsy, stroke, and spinal cord injury cause hand impairments for 15.2 million people in the United States alone [8]. Joint stiffness is a key characteristic of many hand impairments. Comorbidities such as paralysis of the intrinsic muscles, fixed contractures, hypertonia, atrophy due to disuse, skin burns, and spasticity affect joint stiffness [**?**]. Finger joint stiffness is a commonly evaluated and reported clinical metric, and its presence may severely affect hand function [9, 10, 7, 11]. Within the clinic, it is characterized by reduced range of motion, and greater opposition to movement due to muscle tightness, tendon adhesions and joint capsule problems [12]. Careful quantitative measurement of joint stiffness has the potential to improve the diagnosis and treatment of diseases that affect the hand [10], in addition to improving rehabilitation exercise prescription, and orthosis and prosthesis designs [7, 11].

Passive torque measured about the second metacarpophalangeal (MCP) joint during cyclic extension and flexion is a sum of the contributions of the stiffness of the passive extrinsic and intrinsic muscle tendon units, the ligaments, the synovial fluid, joint capsule, the articular cartilage and bone on bone contact [12, **?**, 13, 14]. Hysteresis loops of the torque angle observed during cyclic loading of the passive MCP joint is similar in shape to the observations at other synovial joints, such as the elbow, the hip and the knee. The second digit is an important part of grasp and manipulation tasks, and the contribution of the MCP joint to the control of this biarticular linkage system is crucial. The contributions of the viscoelastic stiffness have been shown to be the primary contributors to the passive MCP stiffness [6], and extension of this joint, the most affected function after injury [15]. While differences in passive extension torque about the second MCP have been observed between males and females, the effects of anthropometric factors in the observed variability is unknown. This study has three primary contributions – first, it quantifies the torque angle relationship for 20 unimpaired subjects, the largest sample known thus-far. The subjects are distributed equally between males and females. This study examines the effects of locking the interphalangeal and distal interphalangeal joints and compares torques between the dominant and non-dominant hands. This study also evaluates the effect of whole body, hand and finger specific anthropometric measurements on the passive MCP extension torques, and helps quantify normalized torque angle representations. Lastly, passive extension torque data from 2 male individuals with chronic hand paralysis due to spinal cord injury are compared against the normalized torque angle band from the unimpaired individuals to demonstrate the capability of this data to aid quantification of hand function.

2.3 Methods

2.3.1 Finger arthrograph design and validation

Passive joint extension torque about the second MCP joint was measured at different angles during the extension of the second digit using a device designed to apply an external torque to the digit, while constraining the wrist at 0 degrees of extension (Fig. 1). Force information (F_{LC}) was collected using a tensile compressive type uniaxial load cell (rated load, 25 lbs) synchronously with angular information, collected with a video camera. The video data (30 fps) was used to compute the angle of the MCP joint, θ_{mcp}. A system model was developed using the free body diagram approach under an assumption of quasi-static loading. In an experiment designed to validate the model, we used a torque cell attached to an indexed bar to mimic the MCP joint. By applying suspended weights to the set-up shown in (Fig. 2), we find good agreement (RMSE = 0.98) between the measured torque and the predicted torque from the model.

2.3.2 Measurement of passive extension torque about second MCP joint

In a study approved by the Institutional Review Board at the University of Washington, the extension torques for the second MCP joint were measured on both hands for 22 healthy

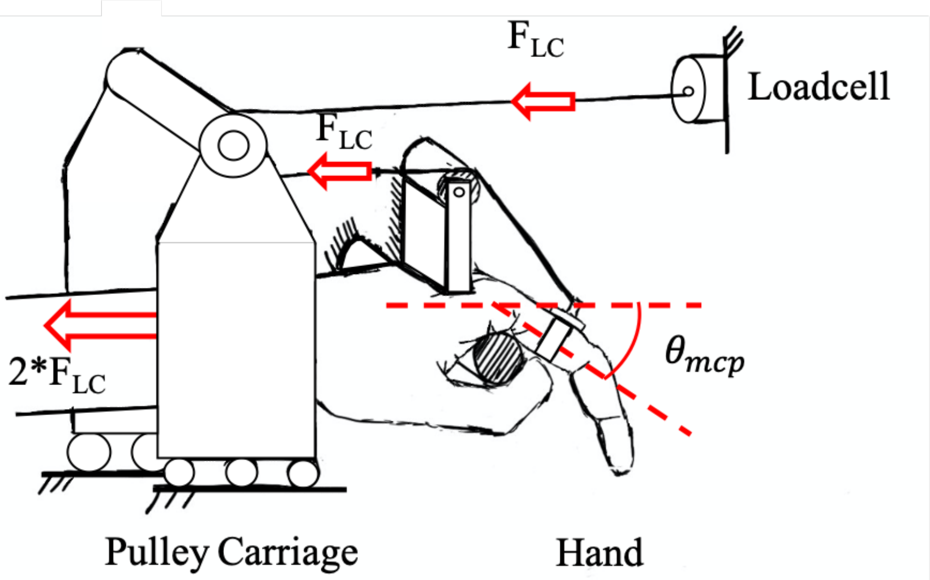

Figure 2.1: A lineart figure demonstrating the measurement system used to quantify the passive extension torque for the second MCP. The angular measurements were made with a camera tracking features on the finger at 30 fps.

subjects without hand impairments, recruited from the University of Washington. 2 subjects had incomplete datasets and were excluded. The subjects were equally distributed between males and females; all were right hand dominant. Detailed anthropometric measures, both summary body measures such as age, height, weight, and hand specific measures such as lengths and volumetric data of the hand, and index finger were collected (Table 1).

These data (30 ± 8 trials) for each hand were used to compute the net passive extension torque over the range of motion for each subject computed as the difference between the torque applied by the taut string and the torque due to gravity. Dynamics were ignored because of the quasi-static nature of the test. The finger was slowly moved from 50 degrees

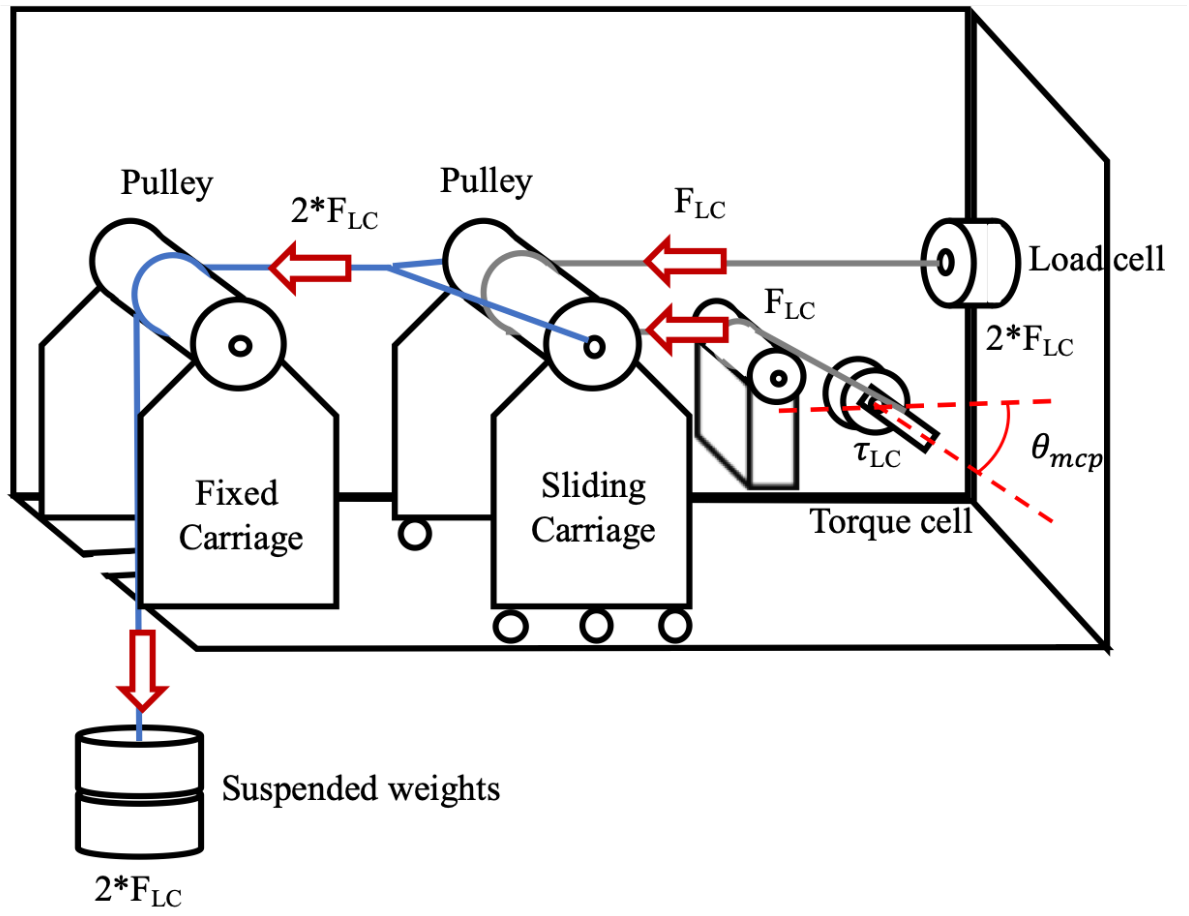

Figure 2.2: A lineart figure demonstrating a set up to validate the measurement system used to quantify the passive extension torque for the second MCP.

of flexion to 0 degrees, corresponding to the long axis of the proximal phalanx aligned with the long axis of the metacarpal. Wrist was held in extension because this position prevents the extensor digitorum communis (EDC) from being stretched tight, thus limiting the passive stretching of the extrinsic muscle from confounding the measurement of MCP passive stiffness. This is also the preferred position for hand therapy, to prevent contracture of flexors and collateral ligaments and capsules.

We measured the passive joint extension torque in two conditions randomized on each index finger: a splinted condition (S), with extended and locked proximal interphalangeal

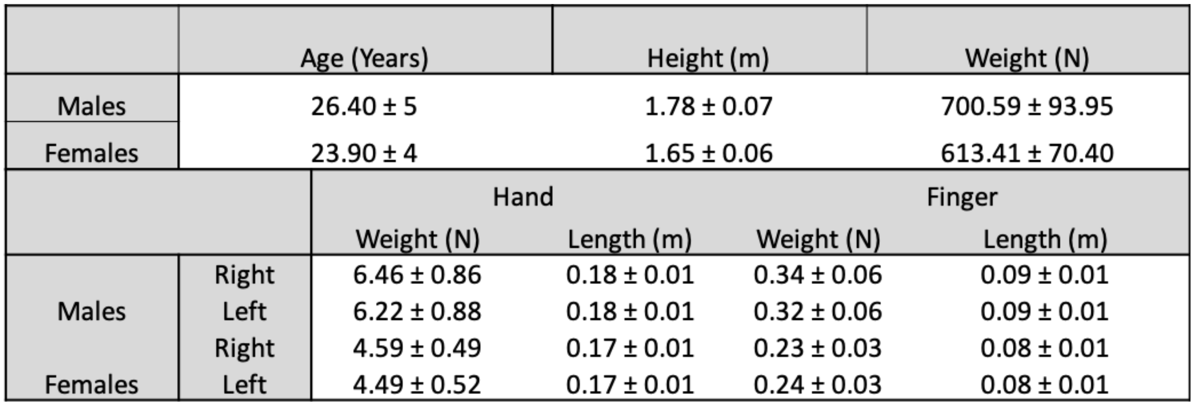

	Age (Years)	Height (m)	Weight (N)
Males	26.40 ± 5	1.78 ± 0.07	700.59 ± 93.95
Females	23.90 ± 4	1.65 ± 0.06	613.41 ± 70.40

		Hand		Finger	
		Weight (N)	Length (m)	Weight (N)	Length (m)
Males	Right	6.46 ± 0.86	0.18 ± 0.01	0.34 ± 0.06	0.09 ± 0.01
	Left	6.22 ± 0.88	0.18 ± 0.01	0.32 ± 0.06	0.09 ± 0.01
Females	Right	4.59 ± 0.49	0.17 ± 0.01	0.23 ± 0.03	0.08 ± 0.01
	Left	4.49 ± 0.52	0.17 ± 0.01	0.24 ± 0.03	0.08 ± 0.01

Table 2.1: Anthropomorphic data from 20 right handed subjects distributed equally by gender

(PIP) and distal interphalangeal (DIP) joints, and the second, the non-splinted (NS) with a neutral and unlocked PIP and DIP joint.

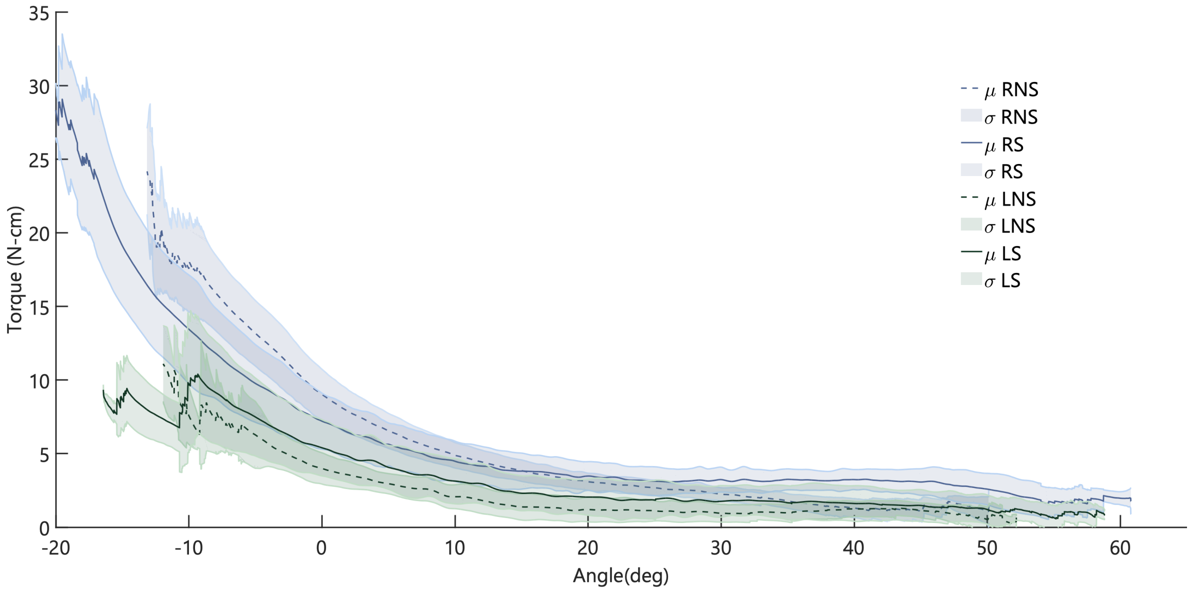

Figure 2.3: A representative torque angle plot for one subject with data from all four conditions: Right hand splinted index finger (RS), Right hand non-splinted index finger (RNS), Left hand splinted index finger (LS), Left hand non-splinted index finger (LNS)

We used a two-sample t-test for independent means and unequal variance, to test our hypothesis that the mean passive extension torque about the MCP joint at 0, 10, 20, 30, 40 and 50 degrees of flexion are the same for males and females, and for dominant and non-dominant hands. For testing the hypothesis that the mean passive extension torque about the MCP joint at 0, 10, 20, 30, 40 and 50 degrees of flexion are the same for the splinted and non-splinted conditions for each subject, we used a two-sample paired t-test. We tested our hypothesis that S and NS conditions would not affect the torque significantly with a two-sample paired t-test.

2.3.3 Normalization of MCP torque by anthropometric measures

Using regression analysis and the coefficient of determination, we quantified how whole-body measures like body weight and height, hand specific measures like hand weight and hand length, and finger specific measures like finger weight and finger length predict the passive extension torque about the second MCP. We normalized the passive extension torque with the body specific, hand specific and finger specific measures (Table 4) and computed the effect of the different methods of normalization using the coefficient of variation, or the mean normalized standard deviation.

2.3.4 Normative data and exponential model from normalized passive extension torque angle data

The statistics of the passive extension torque about the MCP normalized with finger specific measurements is used as a normative dataset. An exponential model is fit to the normative data. Finally, to demonstrate the utility of this data, the normative data is compared to 2 participants with chronic hand paralysis due to SCI.

2.4 Results

2.4.1 Raw torques measured about the passive second MCP by conditions

The passive extension torque about the second MCP, when the finger was in full extension (0 degrees, splinted, dominant hand), was $10.95 \pm 2.38 N - cm$ for males, and $5.03 \pm 1.60 N - cm$ for females (Table. 2), averaged across both hands. Males had significantly higher torques for 0, 10, 20, and 30 degrees of finger flexion ($p < 0.0029$). The passive extension torques about the second MCP joint of the dominant hand were not found to be significantly different from the non-dominant hand for males ($p > 0.6300$) or for females ($p > 0.2200$). In the non-splinted condition, the passive extension torques about the sec-

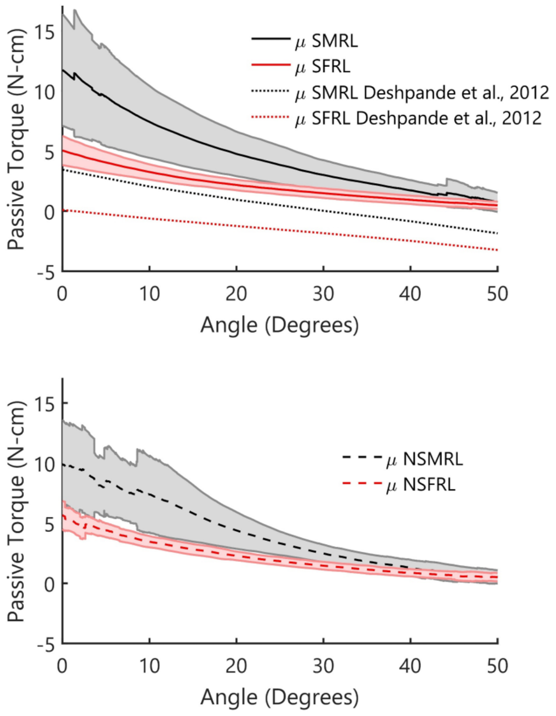

Figure 2.4: Torque angle curves for all subjects and compared across genders. We also compare to Deshpande 2012 to relate our results to literature

ond MCP were found to be significantly higher than the splinted condition among females, for 0, 10 and 20 degrees of flexion ($p < 0.0120$). No significant difference was observed in the passive extension torques about the second MCP for males between the splinted and non-splinted conditions ($p > 0.0930$), however.

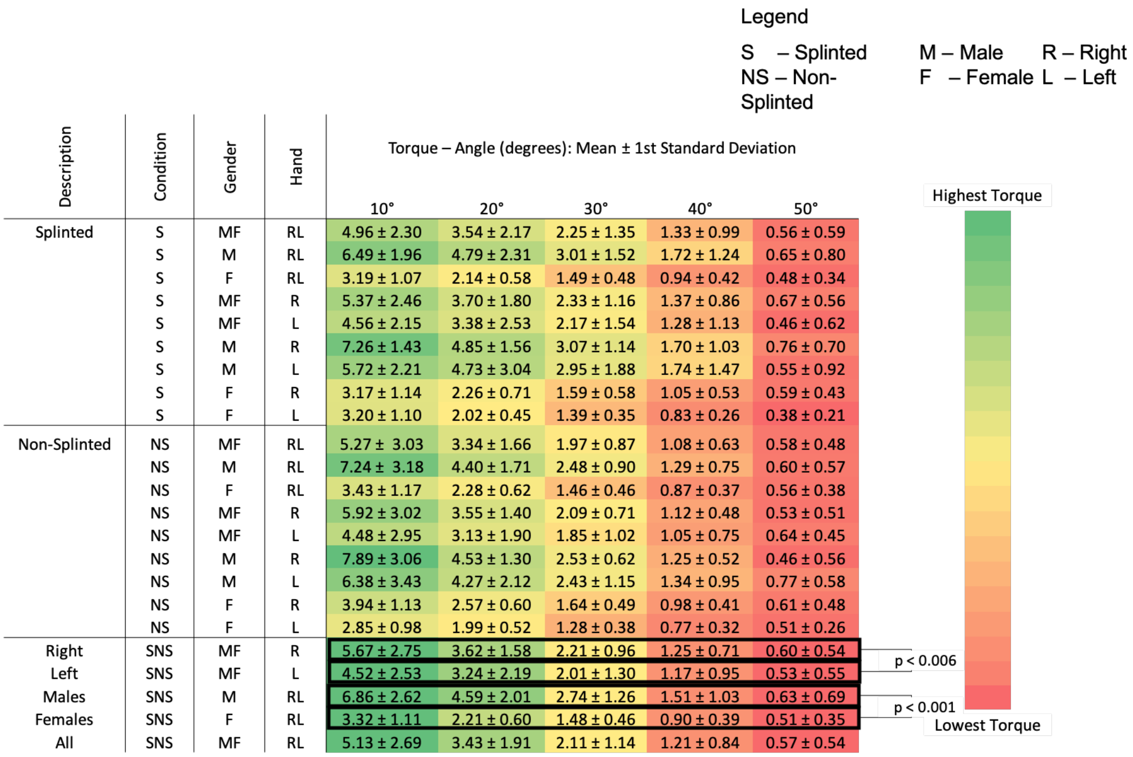

Legend

S – Splinted
NS – Non-Splinted
M – Male
F – Female
R – Right
L – Left

Description	Condition	Gender	Hand	Torque – Angle (degrees): Mean ± 1st Standard Deviation				
				10°	20°	30°	40°	50°
Splinted	S	MF	RL	4.96 ± 2.30	3.54 ± 2.17	2.25 ± 1.35	1.33 ± 0.99	0.56 ± 0.59
	S	M	RL	6.49 ± 1.96	4.79 ± 2.31	3.01 ± 1.52	1.72 ± 1.24	0.65 ± 0.80
	S	F	RL	3.19 ± 1.07	2.14 ± 0.58	1.49 ± 0.48	0.94 ± 0.42	0.48 ± 0.34
	S	MF	R	5.37 ± 2.46	3.70 ± 1.80	2.33 ± 1.16	1.37 ± 0.86	0.67 ± 0.56
	S	MF	L	4.56 ± 2.15	3.38 ± 2.53	2.17 ± 1.54	1.28 ± 1.13	0.46 ± 0.62
	S	M	R	7.26 ± 1.43	4.85 ± 1.56	3.07 ± 1.14	1.70 ± 1.03	0.76 ± 0.70
	S	M	L	5.72 ± 2.21	4.73 ± 3.04	2.95 ± 1.88	1.74 ± 1.47	0.55 ± 0.92
	S	F	R	3.17 ± 1.14	2.26 ± 0.71	1.59 ± 0.58	1.05 ± 0.53	0.59 ± 0.43
	S	F	L	3.20 ± 1.10	2.02 ± 0.45	1.39 ± 0.35	0.83 ± 0.26	0.38 ± 0.21
Non-Splinted	NS	MF	RL	5.27 ± 3.03	3.34 ± 1.66	1.97 ± 0.87	1.08 ± 0.63	0.58 ± 0.48
	NS	M	RL	7.24 ± 3.18	4.40 ± 1.71	2.48 ± 0.90	1.29 ± 0.75	0.60 ± 0.57
	NS	F	RL	3.43 ± 1.17	2.28 ± 0.62	1.46 ± 0.46	0.87 ± 0.37	0.56 ± 0.38
	NS	MF	R	5.92 ± 3.02	3.55 ± 1.40	2.09 ± 0.71	1.12 ± 0.48	0.53 ± 0.51
	NS	MF	L	4.48 ± 2.95	3.13 ± 1.90	1.85 ± 1.02	1.05 ± 0.75	0.64 ± 0.45
	NS	M	R	7.89 ± 3.06	4.53 ± 1.30	2.53 ± 0.62	1.25 ± 0.52	0.46 ± 0.56
	NS	M	L	6.38 ± 3.43	4.27 ± 2.12	2.43 ± 1.15	1.34 ± 0.95	0.77 ± 0.58
	NS	F	R	3.94 ± 1.13	2.57 ± 0.60	1.64 ± 0.49	0.98 ± 0.41	0.61 ± 0.48
	NS	F	L	2.85 ± 0.98	1.99 ± 0.52	1.28 ± 0.38	0.77 ± 0.32	0.51 ± 0.26
Right	SNS	MF	R	5.67 ± 2.75	3.62 ± 1.58	2.21 ± 0.96	1.25 ± 0.71	0.60 ± 0.54
Left	SNS	MF	L	4.52 ± 2.53	3.24 ± 2.19	2.01 ± 1.30	1.17 ± 0.95	0.53 ± 0.55
Males	SNS	M	RL	6.86 ± 2.62	4.59 ± 2.01	2.74 ± 1.26	1.51 ± 1.03	0.63 ± 0.69
Females	SNS	F	RL	3.32 ± 1.11	2.21 ± 0.60	1.48 ± 0.46	0.90 ± 0.39	0.51 ± 0.35
All	SNS	MF	RL	5.13 ± 2.69	3.43 ± 1.91	2.11 ± 1.14	1.21 ± 0.84	0.57 ± 0.54

p < 0.006

p < 0.001

Table 2.2: Table with mean torques and 1 standard deviation for all conditions across hand gender and condition, from complete extension (0 deg.) to flexion (50 deg.)

We also found that torques at full extension, (0 degrees, splinted, right hand) are significantly higher than previously reported values [6], both among males ($p < 0.0485$) and among females ($p < 0.00018$). We also observed that the males have higher variance in both the splinted and non-splinted case, which increases as the finger is extended further.

2.4.2 Normalization of passive MCP torque by anthropometric measures

To examine the cause of the observed difference between our results and the prior work, we conjectured that anthropometric measures affect the measured torque. To examine this hypothesis, we performed a correlation analysis between measured torque and body specific, hand specific and finger specific anthropometric measures. We found that body weight times height (BW*H), hand weight times hand length (HW*HL) and finger weight times finger length (FW*FL) were weak predictors of passive extension torque about the second MCP joint (Table 3). However, in general, FW*FL was a better predictor of the passive extension torque about the second MCP than HW*HL and BW*H (Fig 5). Normalizing the splinted torque by BW*H, HW*HL and FW*FL decreased inter-subject variability by 9%, 18% and 21% respectively, demonstrating that finger specific measures are a better normalizing parameter for hand torques.

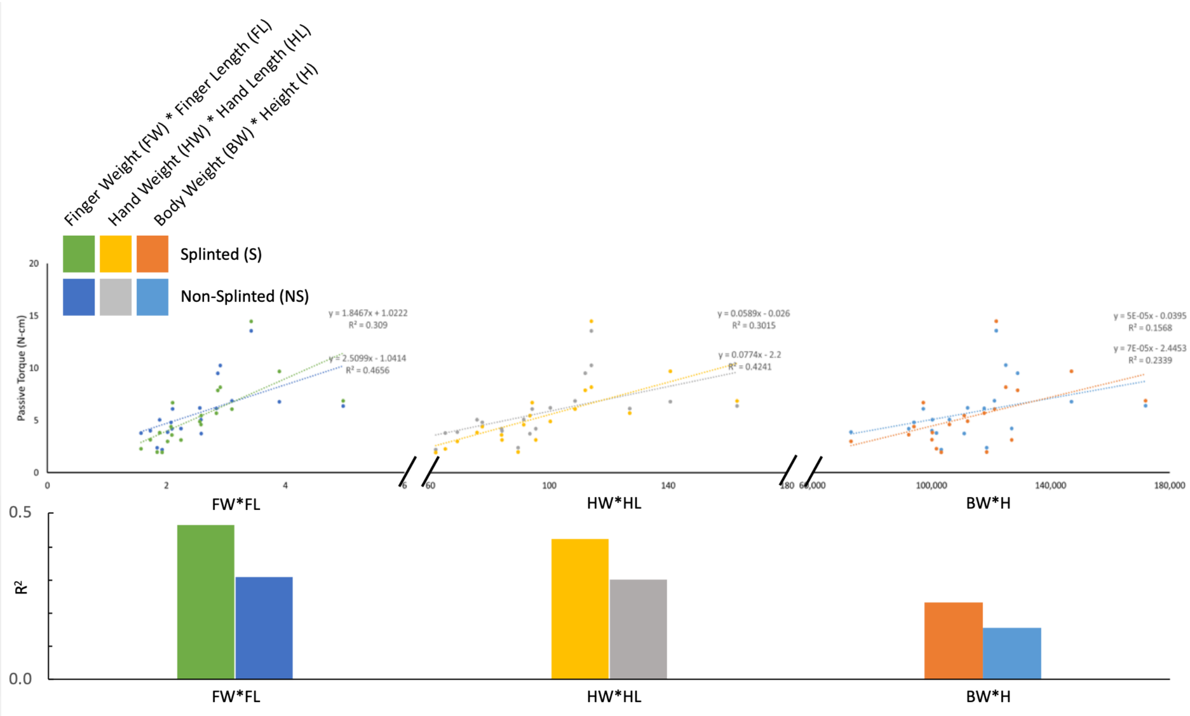

Figure 2.5: Finger specific normalization metrics are better than hand and body specific normalization metrics

Right Hand		10°			20°			30°			40°	
Non-Splinted	k	c	R^2	k	c	R^2	k	c	R^2	k	c	R^2
BW*H	0.000	-0.040	0.157	0.000	-0.276	0.262	0.000	-0.076	0.330	0.000	0.738	0.013
HW*HLR	0.059	-0.026	0.302	0.037	-0.085	0.457	0.021	0.035	0.574	0.007	0.385	0.111
FW*FLR	18.116	1.022	0.309	11.031	0.670	0.439	6.037	0.512	0.517	1.928	0.558	0.094

Splinted	k	c	R^2	k	c	R^2	k	c	R^2	k	c	R^2
BW*H	0.000	-2.445	0.234	0.000	-1.619	0.300	0.000	-0.761	0.249	0.000	0.160	0.070
HW*HLR	0.077	-2.200	0.424	0.049	-1.294	0.508	0.029	-0.537	0.414	0.012	0.218	0.123
FW*FLR	24.622	-1.041	0.466	15.478	-0.491	0.541	9.257	-0.089	0.451	4.166	0.287	0.166

Left Hand		10°			20°			30°			40°	
Non-Splinted	k	c	R^2	k	c	R^2	k	c	R^2	k	c	R^2
BW*H	0.000	-2.255	0.146	0.000	-0.813	0.151	0.000	-0.195	0.143	0.000	-0.419	0.136
HW*HLL	0.071	-1.653	0.267	0.040	-0.666	0.303	0.022	-0.239	0.324	0.016	-0.444	0.303
FW*FLL	28.757	-2.134	0.382	15.274	-0.708	0.387	7.785	-0.100	0.352	5.075	-0.221	0.275

Splinted	k	c	R^2	k	c	R^2	k	c	R^2	k	c	R^2
BW*H	0.000	-0.190	0.075	0.000	0.007	0.070	0.000	0.340	0.050	0.000	0.664	0.011
HW*HLL	0.056	0.015	0.151	0.036	-0.052	0.156	0.021	0.139	0.132	0.010	0.306	0.057
FW*FLL	23.467	-0.600	0.235	14.334	-0.220	0.215	8.679	-0.010	0.191	4.784	0.081	0.108

Table 2.3: Table with regression fit coefficients to different normalization techniques. Finger specific normalization metrics are better than hand and body specific normalization metric

2.4.3 Normalization of passive MCP torque demonstrates reduction in observed variance

We normalize the passive extension torques recorded in table 2 by finger weight times finger length specific to each subject (Table 5).

A linear mixed effects model demonstrated that only gender and angle were found to be main effects. However, the observed trend in the normalized torque demonstrated a very small effect of gender (Fig.6).

To understand this effect, we ran a post-hoc Tukey multicomparison study, and found that torque at 20 degree extension was significantly different between the genders (p¡0.005). Finally, we average all the torque profiles to form a population average or normative band of torque required to extend the passive second digit, and we fit an exponential model to the data (Table 6).

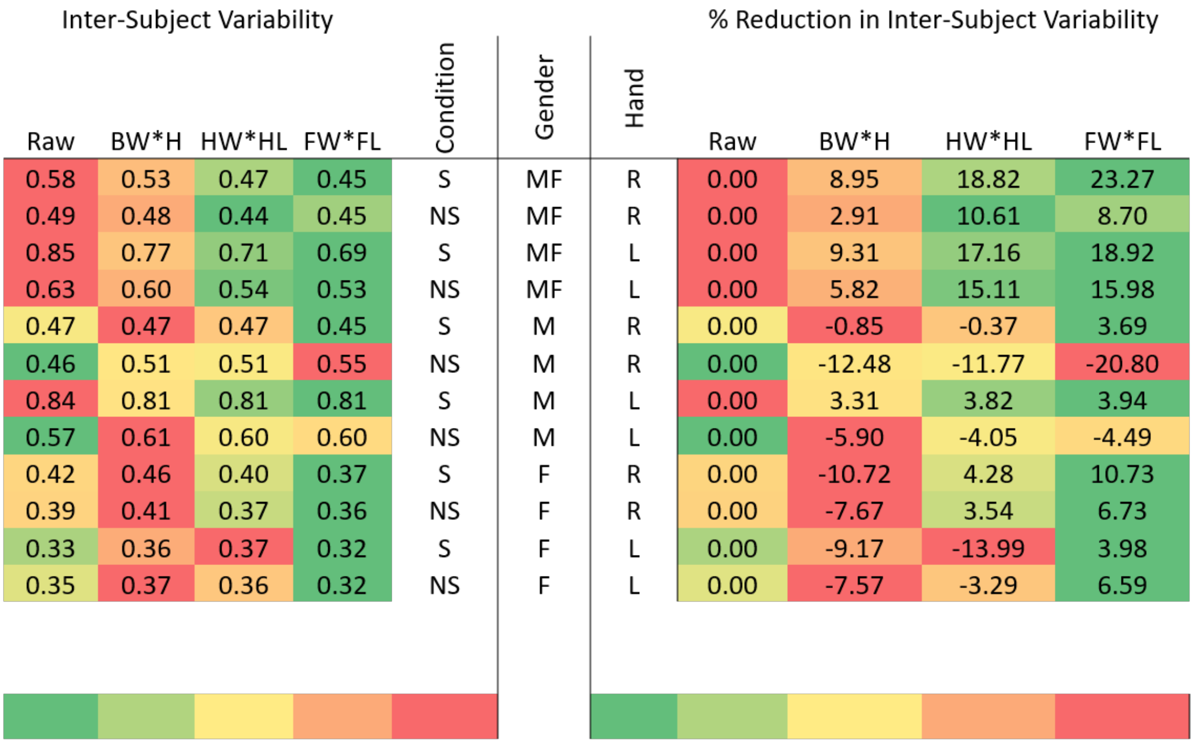

Inter-Subject Variability							% Reduction in Inter-Subject Variability			
Raw	BW*H	HW*HL	FW*FL	Condition	Gender	Hand	Raw	BW*H	HW*HL	FW*FL
0.58	0.53	0.47	0.45	S	MF	R	0.00	8.95	18.82	23.27
0.49	0.48	0.44	0.45	NS	MF	R	0.00	2.91	10.61	8.70
0.85	0.77	0.71	0.69	S	MF	L	0.00	9.31	17.16	18.92
0.63	0.60	0.54	0.53	NS	MF	L	0.00	5.82	15.11	15.98
0.47	0.47	0.47	0.45	S	M	R	0.00	-0.85	-0.37	3.69
0.46	0.51	0.51	0.55	NS	M	R	0.00	-12.48	-11.77	-20.80
0.84	0.81	0.81	0.81	S	M	L	0.00	3.31	3.82	3.94
0.57	0.61	0.60	0.60	NS	M	L	0.00	-5.90	-4.05	-4.49
0.42	0.46	0.40	0.37	S	F	R	0.00	-10.72	4.28	10.73
0.39	0.41	0.37	0.36	NS	F	R	0.00	-7.67	3.54	6.73
0.33	0.36	0.37	0.32	S	F	L	0.00	-9.17	-13.99	3.98
0.35	0.37	0.36	0.32	NS	F	L	0.00	-7.57	-3.29	6.59

Table 2.4: Table with coefficient of variations to indicate movements

2.5 *Discussion and Conclusions*

We quantified the passive extension torque about the second MCP joint of the human hand for 10 right handed males and 10 right handed females between splinted and non-splinted conditions. We examined the correlation between whole body measures like body weight and height, hand specific measures like hand weight and hand length, and finger specific measures like finger weight and finger length, and the passive extension torque about the second MCP joint. By normalizing the passive extension torque, we reduced the inter-subject variability, giving us a measure of comparison for impaired function. We demonstrated this through the two case studies with individuals with spinal cord injury related impairment of hand function.

Our results (Fig. 2) demonstrates that a narrow band of torque is required for passively

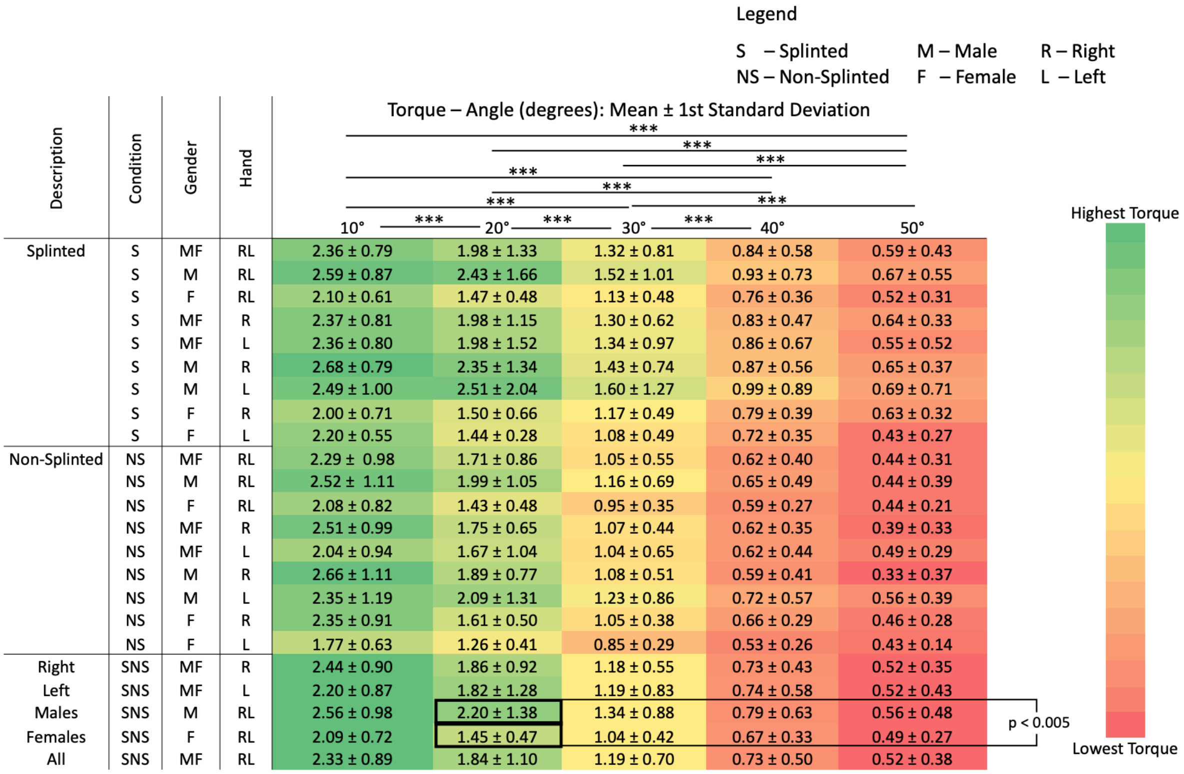

Description	Condition	Gender	Hand	10°	20°	30°	40°	50°
Splinted	S	MF	RL	2.36 ± 0.79	1.98 ± 1.33	1.32 ± 0.81	0.84 ± 0.58	0.59 ± 0.43
	S	M	RL	2.59 ± 0.87	2.43 ± 1.66	1.52 ± 1.01	0.93 ± 0.73	0.67 ± 0.55
	S	F	RL	2.10 ± 0.61	1.47 ± 0.48	1.13 ± 0.48	0.76 ± 0.36	0.52 ± 0.31
	S	MF	R	2.37 ± 0.81	1.98 ± 1.15	1.30 ± 0.62	0.83 ± 0.47	0.64 ± 0.33
	S	MF	L	2.36 ± 0.80	1.98 ± 1.52	1.34 ± 0.97	0.86 ± 0.67	0.55 ± 0.52
	S	M	R	2.68 ± 0.79	2.35 ± 1.34	1.43 ± 0.74	0.87 ± 0.56	0.65 ± 0.37
	S	M	L	2.49 ± 1.00	2.51 ± 2.04	1.60 ± 1.27	0.99 ± 0.89	0.69 ± 0.71
	S	F	R	2.00 ± 0.71	1.50 ± 0.66	1.17 ± 0.49	0.79 ± 0.39	0.63 ± 0.32
	S	F	L	2.20 ± 0.55	1.44 ± 0.28	1.08 ± 0.49	0.72 ± 0.35	0.43 ± 0.27
Non-Splinted	NS	MF	RL	2.29 ± 0.98	1.71 ± 0.86	1.05 ± 0.55	0.62 ± 0.40	0.44 ± 0.31
	NS	M	RL	2.52 ± 1.11	1.99 ± 1.05	1.16 ± 0.69	0.65 ± 0.49	0.44 ± 0.39
	NS	F	RL	2.08 ± 0.82	1.43 ± 0.48	0.95 ± 0.35	0.59 ± 0.27	0.44 ± 0.21
	NS	MF	R	2.51 ± 0.99	1.75 ± 0.65	1.07 ± 0.44	0.62 ± 0.35	0.39 ± 0.33
	NS	MF	L	2.04 ± 0.94	1.67 ± 1.04	1.04 ± 0.65	0.62 ± 0.44	0.49 ± 0.29
	NS	M	R	2.66 ± 1.11	1.89 ± 0.77	1.08 ± 0.51	0.59 ± 0.41	0.33 ± 0.37
	NS	M	L	2.35 ± 1.19	2.09 ± 1.31	1.23 ± 0.86	0.72 ± 0.57	0.56 ± 0.39
	NS	F	R	2.35 ± 0.91	1.61 ± 0.50	1.05 ± 0.38	0.66 ± 0.29	0.46 ± 0.28
	NS	F	L	1.77 ± 0.63	1.26 ± 0.41	0.85 ± 0.29	0.53 ± 0.26	0.43 ± 0.14
Right	SNS	MF	R	2.44 ± 0.90	1.86 ± 0.92	1.18 ± 0.55	0.73 ± 0.43	0.52 ± 0.35
Left	SNS	MF	L	2.20 ± 0.87	1.82 ± 1.28	1.19 ± 0.83	0.74 ± 0.58	0.52 ± 0.43
Males	SNS	M	RL	2.56 ± 0.98	2.20 ± 1.38	1.34 ± 0.88	0.79 ± 0.63	0.56 ± 0.48
Females	SNS	F	RL	2.09 ± 0.72	1.45 ± 0.47	1.04 ± 0.42	0.67 ± 0.33	0.49 ± 0.27
All	SNS	MF	RL	2.33 ± 0.89	1.84 ± 1.10	1.19 ± 0.70	0.73 ± 0.50	0.52 ± 0.38

Torque – Angle (degrees): Mean ± 1st Standard Deviation

Figure 2.6: Table with regression fit coefficients to different normalization techniques. Finger specific normalization metrics are better than hand and body specific normalization metric

extending the unimpaired joint. This torque is significantly lower for females than for males. This agrees with prior work [7, 13, 6]. Interestingly, this difference persisted even after normalization with anthropometric measures. This indicates that although anthropometric data were predictors of passive extension torque, other correlated gender specific parameters may be causing the observed differences. Females have higher joint laxity, due to estrogen, and these and other differences may contribute to the observed difference in torque.

Our measured torque values demonstrate the exponential dependency reported in prior literature but are significantly different in magnitude. This difference may be attributed

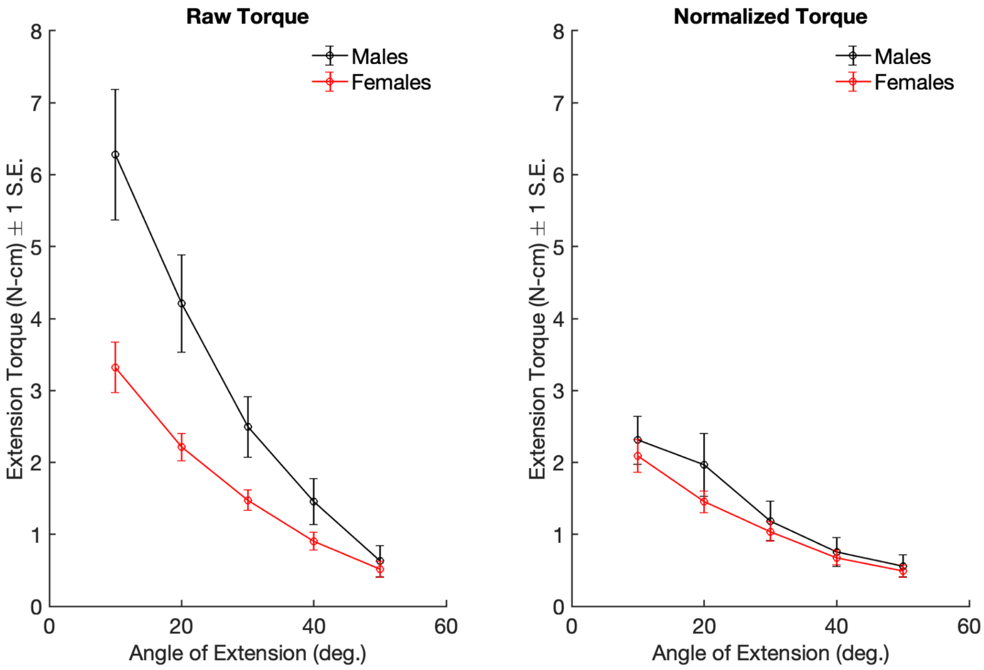

Figure 2.7: Table with regression fit coefficients to different normalization techniques. Finger specific normalization metrics are better than hand and body specific normalization metric

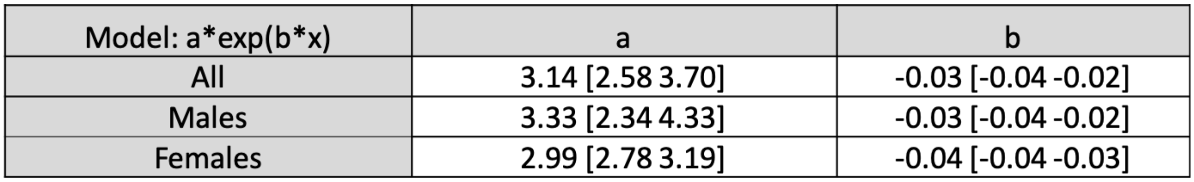

Model: a*exp(b*x)	a	b
All	3.14 [2.58 3.70]	-0.03 [-0.04 -0.02]
Males	3.33 [2.34 4.33]	-0.03 [-0.04 -0.02]
Females	2.99 [2.78 3.19]	-0.04 [-0.04 -0.03]

Figure 2.8: Table with coefficient of exponential model fit to population and each gender

to the difference in the measurement methods, and likely to a sampling bias. Where our method measured the passive torque during the entire range of motion, the previous work allowed the subjects to rest in the position of measurement for 45 seconds before making the measurement [6]. This may have led to stress relaxation and is a characteristic of viscoelastic response of tissues to applied stress [15].

Additionally, males exhibited greater variance in the passive extension torque than females, and the absolute variance grew with increasing extension of the finger (Fig.2,3 and 6). This systematic behavior may be attributed to the larger hand sizes of the male participants which results in larger moment arms through the range of motion.

Normalizing the passive extension torque by finger specific measures was better than normalizing with whole body measures, although the coefficient of determination was low in both cases. Normalizing the data resulted in a reduction in the inter-subject variability, however this reduction was most pronounced when the normalization was performed on the entire population, averaged across genders. This leads us to believe that normalizing the experimental data is valuable most when the sample is heterogenous and consists of both males and females. All participants were right-hand dominant; however, the data shows that while males have a higher coefficient of variation in the non-dominant hand, the females trend towards lower coefficient of variation (Table 4).

This study presents a sample of 20 subjects, which although is larger than other prior samples in the recent past, may still be small to detect sensitive effects. This study does not control the velocity of extension, although care was taken to remain below the subjects' spastic response threshold. The device is subject to small amounts of friction in the prismatic slider. This was minimized by lubricating the guide with graphite-based lubricants. Small amounts of rotation are observed in the mechanical interface with the finger due to tangential torque developed over the soft tissue interface with the finger. Care was taken to align the loadcell and the pulley placement in line with the finger being measured. The tracking is done semi autonomously and may contain uncertainty in measurements. However, the analyses were performed by a single experimenter and therefore a systematic effect may exist in the data.

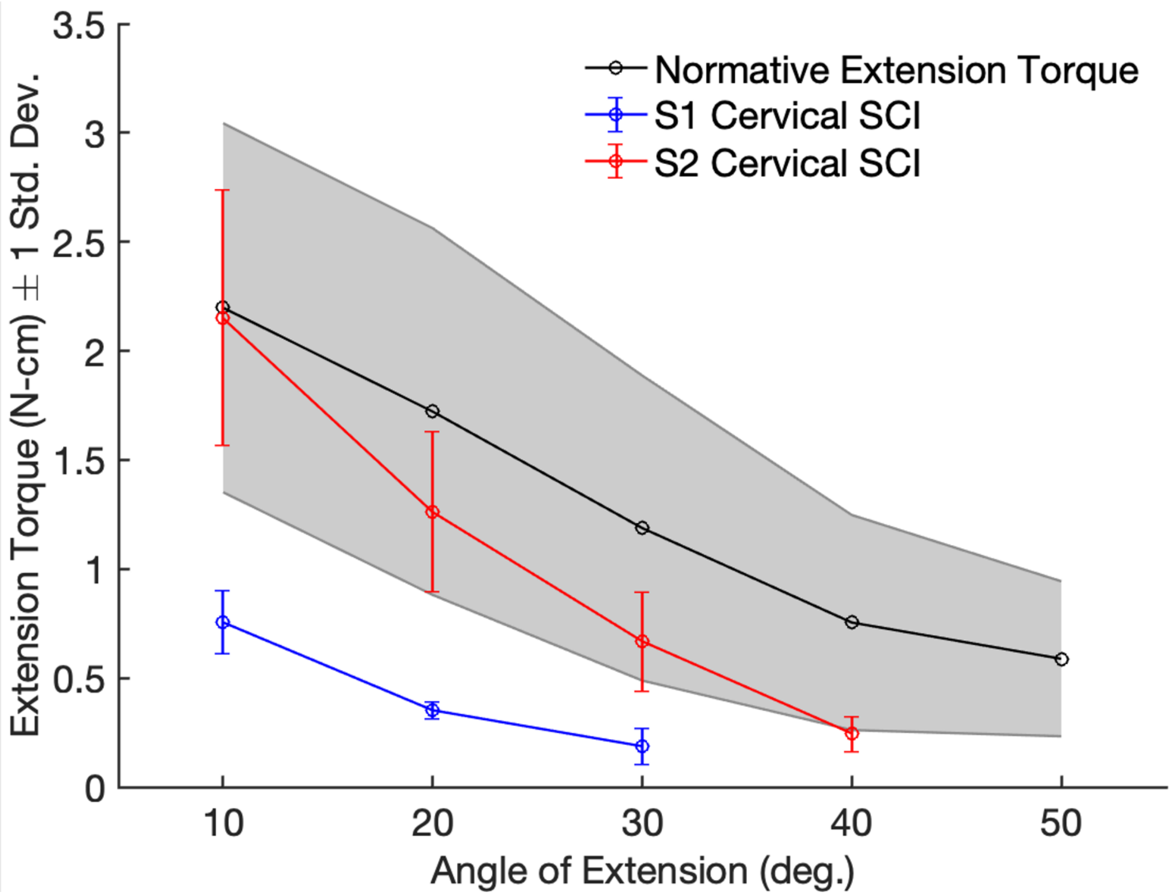

Figure 2.9: Normative dataset with passive extension torque from two subjects with hand paralysis related to chronic cervical SCI overlaid

Chapter 3

STIFFNESS MATCHING AT THE HUMAN DEVICE INTERFACE TRADES COMFORT FOR PERFORMANCE

Rohit John Varghese[1] *, *Gaurav Mukherjee*[2] *, *Raymond King*[3], *Sean Keller*[3], *and Ashish D. Deshpande*[1]

1. Department of Mechanical Engineering, University of Texas at Austin, Austin, Texas 78712, USA
2. Department of Mechanical Engineering, University of Washington, Seattle, WA 98195, USA
3. Facebook Reality Labs, Redmond, WA 98052, USA

*These two authors contributed equally

3.1 Abstract

The design of comfortable and effective physical human robot interaction (pHRI) interfaces for force transfer is a prominent challenge for coupled human-robot systems. Forces applied by the robot at the fingers create reaction forces on the dorsal surface of the hand, often leading to high pressure concentrations which can cause pain and discomfort. In this paper, the interaction between the pHRI interface and the dorsal surface of the hand is systematically characterized, and a new method for the design of comfortable interfaces is presented. The variability of the stiffness of the hand dorsum is quantified experimentally, and this data is used to minimize the peak pressure exerted on the hand dorsum, by varying the stiffness profile of the pHRI interface. This optimized design is demonstrated to improve the pressure distribution over the hand dorsum where the robot is attached to the hand. Additionally, to enable informed design choices, the effects of varying the stiffness of the pHRI interface on relative displacement between the robot and the hand dorsum are also characterized. This optimization approach to designing pHRI interface can be extended to different limbs, especially when there is a transfer of high moment loads to the

human body, provided the appropriate stiffness data is available.

3.2 Introduction

The ideal approach to attaching assistive devices to the human body remains unknown. Designs of attachments, such as shoes, backpacks, clothing, and sporting equipment have evolved to match the contours and articulations of the corresponding body part by using tensioning mechanisms and compliant contact surfaces which help mitigate the effects of moments and forces. While prostheses and wearable robots have embraced these design techniques, the areas of contact between the device and the human body still experience injury and degradation of tissue health. The current approach to designing the contact surfaces, such as sockets for prostheses, is labor intensive, and a quantified approach to generating optimal physical human robot interaction (pHRI) interface designs for high load applications is lacking.

While prosthetic and exoskeletal technology has been improving greatly, rate of disuse of assistive devices remains high [?] [16]. One crucial cause of this is discomfort due to a mismatch of the stiffness between the human limb and the pHRI interface. Designs of pHRI interfaces with uniform stiffness result in localized pressure over bony prominences, and are therefore not ideal [3]. The discomfort due to a uniform pHRI interface is commonly addressed by loosening the straps and reducing the pressure between the pHRI interface and the corresponding contact surface on the human body, also called bias pressure. Reducing the bias pressure to improve comfort between the mismatched surfaces causes relative movement between the robot and the human, which reduces the accuracy of position control [17], causes increased transmission losses [2], and gives rise to inappropriate reaction forces [18], which, ironically, again results in discomfort among users [19]. Discomfort is characterized by high localized pressures [20] [21] which over time lead to the degradation of the tissue structures underneath the points of attachment, resulting in pressure sores [3].

Our goal is to improve comfort by minimizing localized loading and by distributing the

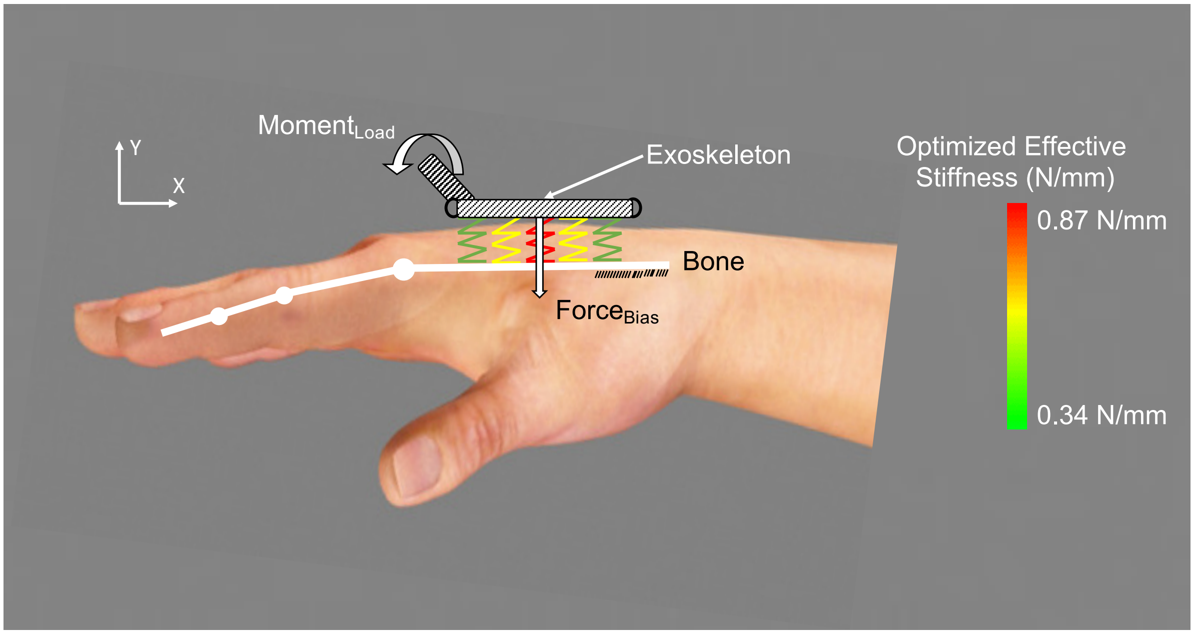

Figure 3.1: Diagram of an exoskeleton interface with optimized varying stiffness profile on the dorsum of the human hand. While the traditional approach to attaching devices on the hand does not take into account the ability to vary the stiffness of the pHRI, our method proposes an optimal stiffness profile that minimizes localized pressure concentrations.

pressure over the hand dorsum (Fig. 3.1). Our approach was to measure the spatial stiffness distribution of the hand dorsum, and using these values, to vary the stiffness of the pHRI interface to achieve our goal of minimizing the localized pressures at the contact surface between the pHRI interface and the hand dorsum. While the general idea of stiffness matching has been explored before [19], a systematic design and analysis has not been performed. To apply this approach of impedance or stiffness matching to the hand, additional constraints must be addressed. Specifically, the contact surface between the hand and hand exoskeletons such as the Maestro [22] and the HX [18] experiences acyclic dynamic forces and moments associated with the high degree of dexterity in hand movements. Therefore an ideal approach to attaching devices to the hand is dependent on multiple criteria, such as the range of external loads applied to the pHRI interface, the stiffness gradient across the surface of the hand and the static pressure that is applied to hold the attachment to the hand under no-loading conditions.

On the Maestro Hand Exoskeleton (Fig. 3.2), a linkage system is attached between the fingers and the plate strapped to the hand dorsum [23] and consequently, the reaction force and moments of all loads applied to the fingers are borne by the dorsum attachment (the pHRI interface) and the hand. The red straps (Figure 3.2) apply the pretension required to hold the plate and the linkage to the hand dorsum and the index finger.

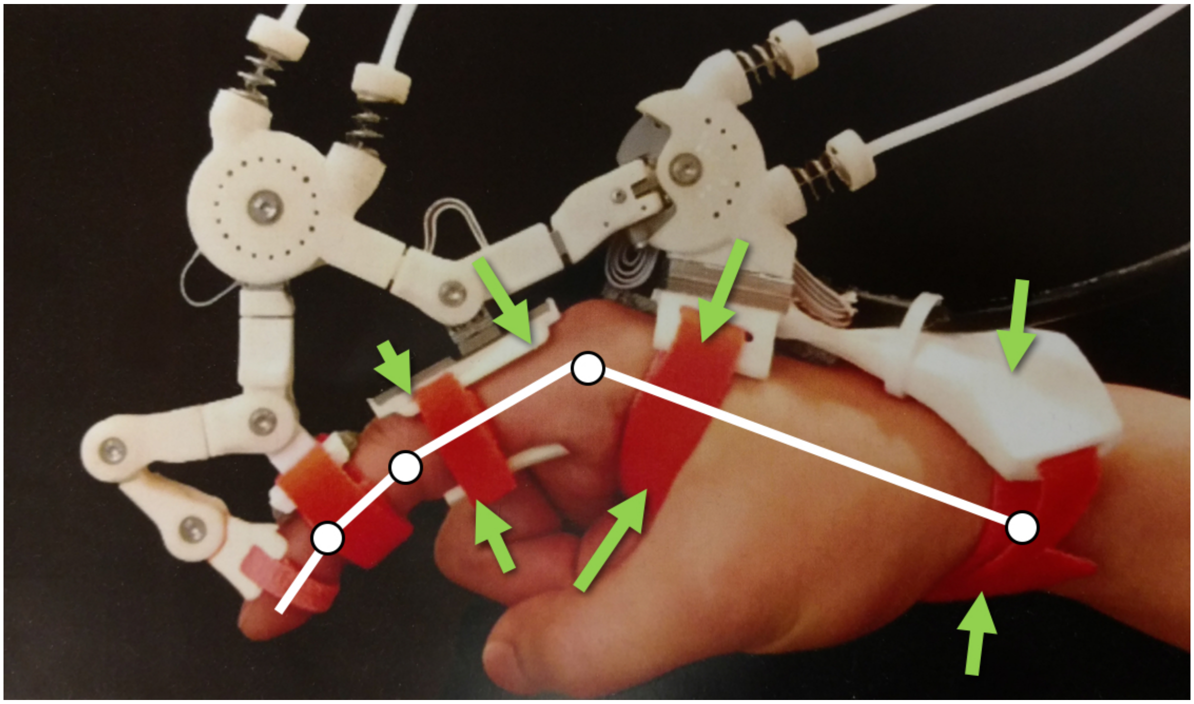

Figure 3.2: Maestro Hand Exoskeleton, with force arrows indicating various locations of pHRI interface in this system.

In this paper, we present a novel method to design a pHRI interface that minimizes localized pressures over the hand dorsum. We drive the design of the pHRI interface to achieve this optimality by measuring the stiffness of the hand dorsum, and by systematically varying the effective stiffness of the pHRI interface spatially over the region of contact with the hand. We analyze the behavior of the system using a numerical simulation environment and identify relationships between applied external load, bias force and the optimal stiffness profiles. We demonstrate that creating varying stiffness patterns of the attachment allows us to control the pressure distribution over the dorsum.

The main contribution of this work is a unique optimization based approach to engineering comfortable pHRI interfaces for attaching robotic systems to the human hand dorsum. In addition, we demonstrate the trade-offs that this design approach may have on performance metrics of the coupled human-robot system, such as relative displacement between the robot and the human. We believe that this systematic approach to creating the ideal pHRI interface for hand exoskeletons can be easily extended to other parts of the human body as well.

3.2.1 pHRI Interface Model

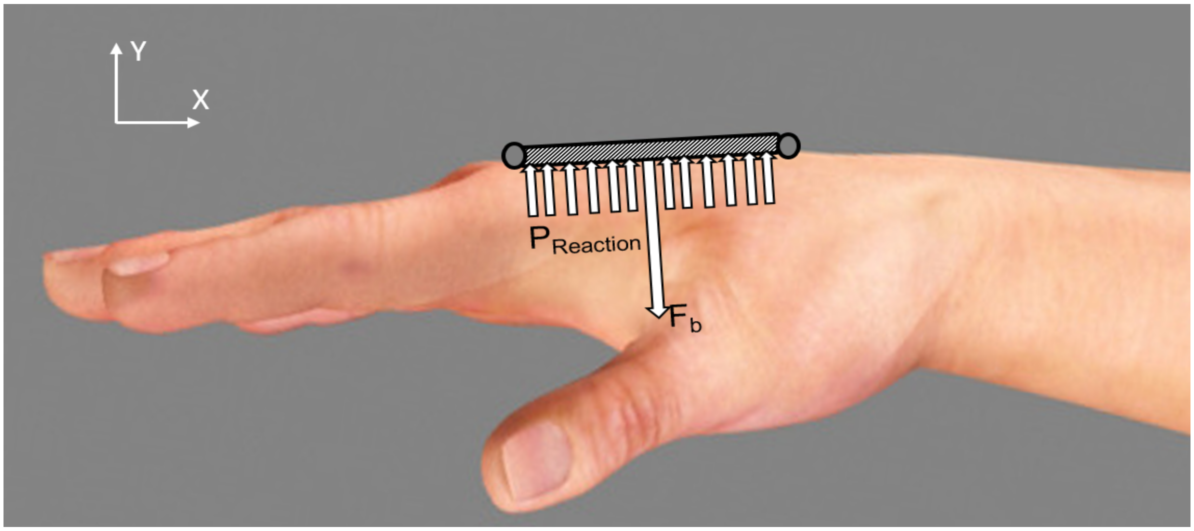

Figure 3.3: Hand dorsum and simplified pHRI with uniform stiffness, bias force (F_b), applied using straps and approximated as a point load at the center, and reaction pressure ($P_{reaction}$).

We model the pHRI (Fig. 3.3) as a discrete array of springs representing the hand dorsum (k_{dorsum}) and the pHRI (k_{pHRI}) interface respectively. These two arrays of springs are in series with each other (Fig. 3.4).

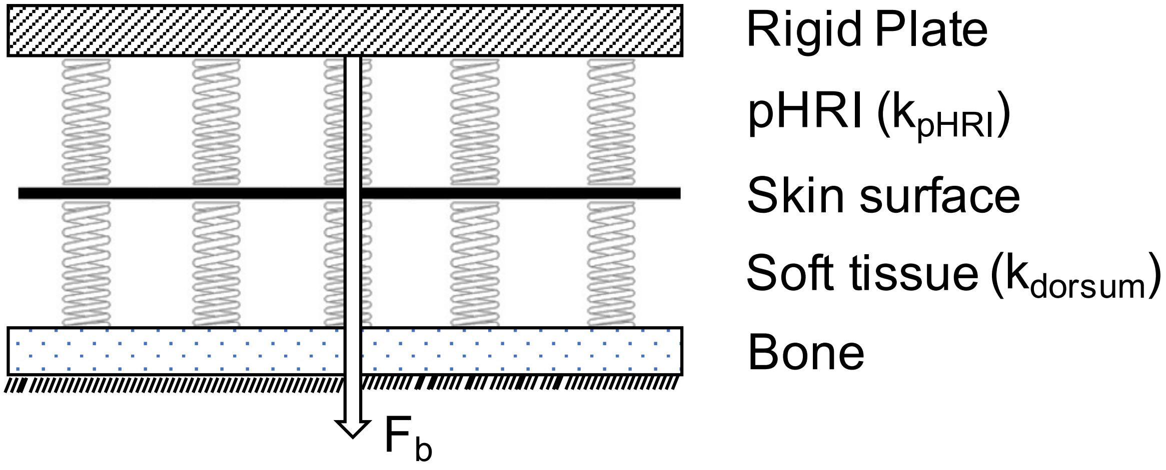

Figure 3.4: Modeling all compliant elements between the human reference structure (our skeleton) and the rigid links of the robot. The stiffness of the hand dorsum (k_{dorsum}) and the pHRI (k_{pHRI}) behave as a set of viscoelastic springs in series.

Through analysis of the simplified system under external load, we deduce the shape of the desired effective stiffness (k_{eff}) of this series spring model that allows us to minimize the peak pressures at the contact surface (Section II.B). Using a numerical simulation environment, we compute the optimal effective stiffness gradient which satisfies the deduced shape profile from the analysis, and that also minimizes peak pressure (Section II.C). Next, we quantify the stiffness profile of the experimenter's hand (k_{dorsum}) through an indentation experiment with a robot (Section II.D). The k_{eff} computed from the numerical simulation and k_{dorsum}, obtained experimentally, are then used to compute the stiffness of the pHRI interface (k_{pHRI}). With the resultant optimal pHRI interface stiffness map (Section II.E), we characterize the relationship between four parameters: the bias force (F_b), which is the representation of strap force preloading the pHRI interface to the hand dorsum under no load condition; the relative displacement, which is the shift of the plate of the exoskeleton with respect to the bone; the gradient of stiffness, which is the ratio of difference between the stiffness at the center and the edge over the stiffness at the center of the pHRI interface (k_{mid} - k_{edge}/k_{mid}); and the peak pressure on the hand dorsum, as a result of external loading due to the hand exoskeleton.

3.2.2 Analytical determination of optimal stiffness profile for the pHRI interface

To design an optimal pHRI interface for the hand dorsum, (Fig. 3.1), we simplify the complex interaction at the interface of the hand dorsum and the pHRI interface as two plates of length L and uniform width sandwiched between the the rigid reference plate of the Maestro robot, and the rigid human bone. The robot reference plate is held to the dorsum by a bias force mimicking a strap (F_b), applied normally and at L/2 (Fig. 3.5).

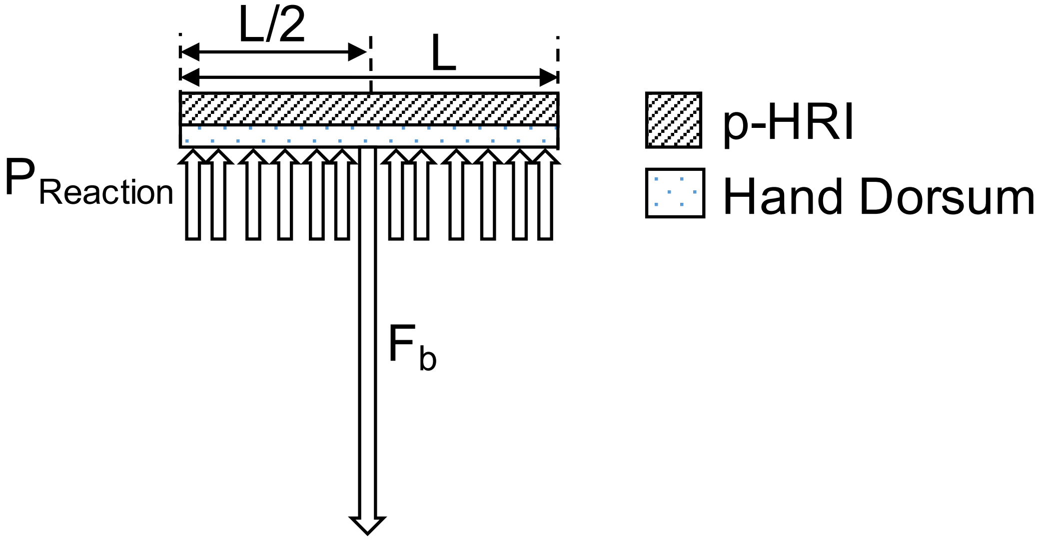

Figure 3.5: Model of hand dorsum and pHRI interface with uniform stiffness, bias force (F_b), and uniform reaction pressure ($P_{reaction}$) distribution.

We then load the pHRI interface with an external force mimicking the reaction forces from the Maestro actuators. Using the principle of transmissibility, we express the applied external force to the attachment plate as a combination of an equivalent force and moment applied at the center of the plate, placed coaxially with the bias force. The resulting reaction pressure ($P_{reaction}$) distribution balances the net force (F_b plus the normal component of F_L) and the external moment (M_L) (Fig. 3.6). Shear loading is considered to be independent and neglected in this section, however, it is considered later in the paper in our overall numerical simulations.

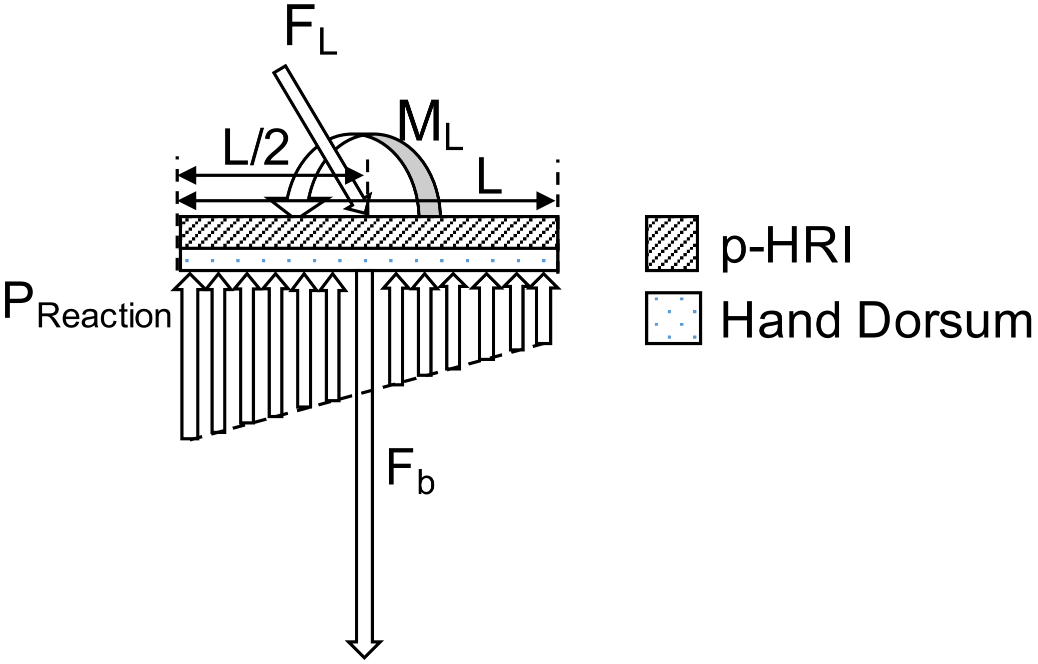

Figure 3.6: Model of hand dorsum and pHRI interface with uniform stiffness, bias force (F_b), externally applied force (F_L), moment load (M_L) and reaction pressure ($P_{reaction}$) distribution.

Our objective is to balance the applied force and moment while minimizing peak reaction pressure (C_i) along the contact surface between the two plates.

$$C_i = max(P_{reaction}) \tag{1}$$

Under the counter-clockwise external moment, M_L, applied on the system, minimizing the cost function, C_i gives us a pressure distribution with two regions of optimized uniform reaction pressure (P_{opt}) below the plate (Fig. 3.7).

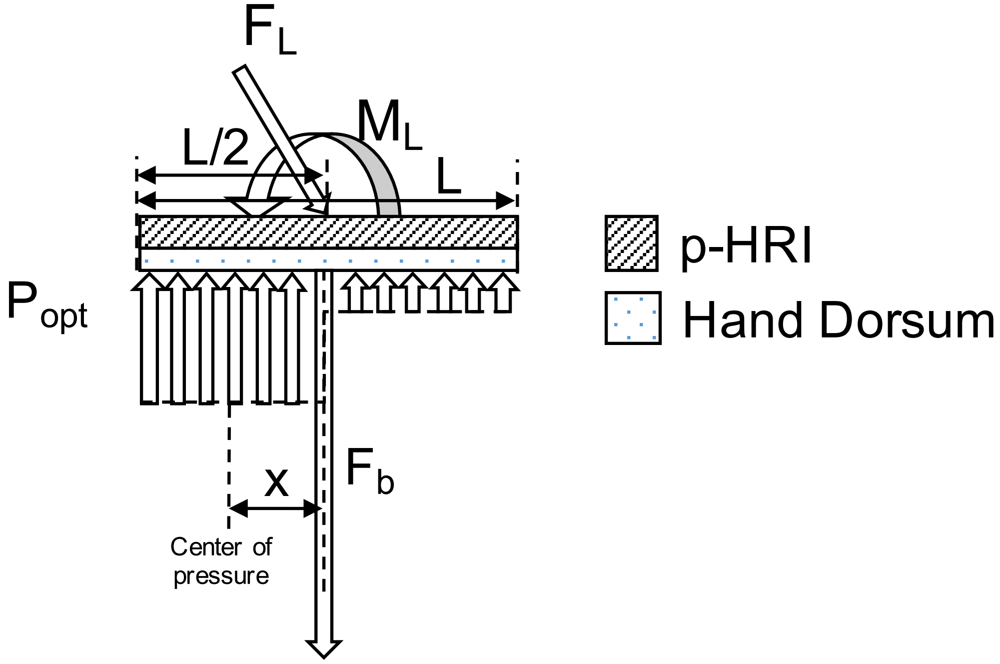

Figure 3.7: Model of hand dorsum and pHRI interface with minimized pressure distribution, bias force (F_b), externally applied force (F_L), moment load (M_L) and resulting two regions of optimal reaction pressure (P_{opt}) distribution.

Since we assume that the sum of pressure is equal to the applied load, minimizing the peak pressure would distribute it over a larger area giving us a region of uniform pressure. However, uniform pressure across the entire plate cannot balance the counter-clockwise applied moment, which explains the existence of two sections of different uniform pressure. This orientation of this reaction pressure distribution depends on the direction of the external loading and reverses itself when the external loading is in the clockwise direction. The boundaries of the regions of uniform pressure shift depending on the ratio of external applied moment (M_L) to the external applied force (F_L). The position of 'x', the center of the highest pressure region in the optimal distribution (P_{opt}), and 'P_{peak}', the magnitude of the highest pressure between the two uniform distributions, are computed in (2) and (3).

$$x = \frac{M_L}{F_L + F_b} \tag{2}$$

$$P_{peak} = \frac{F_L + F_b}{L - 2x} \tag{3}$$

The optimal value of bias force, F_b of the attachment against the dorsum, to minimize C_i for the given force and moment loading configuration, is calculated to be the lowest value that gives us a non-negative pressure region (4):

$$F_b = \frac{4M_L}{L} - F_L \tag{4}$$

The profile of optimal effective stiffness that achieves the optimal pressure (P_{opt}), is a hyperbola with high stiffness in the center of the plate which tapers off towards the edge in the direction of the applied moment, M_L. We simplified this hyperbolic representation to a linear stiffness profile, decreasing from the highest stiffness at the middle of the attachment (k_{mid}), and symmetrically tapering off to a minimum at each edge (k_{edge}). The symmetry allows the resulting profile to be ideal for external moment loads in either direction. To obtain k_{pHRI}, we need to obtain k_{dorsum} in addition to knowing k_{eff}.

3.2.3 Numerical computation of the desired stiffness profile

In order to compute the effective spatial stiffness gradient that minimizes peak pressure, as described in section II.A, and to characterize the relationship between the bias force, the gradient of stiffness, relative displacement between the robot and the human, and the peak pressure over the hand dorsum, we used a pHRI interface simulation environment [24] that was developed to model the forces, pressures and displacements at the pHRI interface under the application of external loads.

Within this environment, the human skeleton, and the links of the coupled robot system are represented as rigid bodies. The necessary constraints are implemented by the method

of Lagrange multipliers [25], and simulated through time with an ODE45 solver in the MATLAB 2017b (MathWorks Inc., Natick, MA) environment. The viscoelastic properties of human skin and soft tissue, and any compliant elements of the robot are incorporated as non-linear stiffness and damping elements between the constituent rigid components of the system. These elements are discretized or lumped based on the level of complexity that we wish to simulate at any given surface, with high discretization at surfaces of interest and single lumped parameters on peripheral regions. This allows us to simulate the behavior of a system under the application of internal and external loads, and observe trends in behavior of the complex interaction system. This is especially useful in pilot study experimentation such as ours where large population samples of humans cannot be recruited.
For this study, the dorsum surface was discretized into 15 total points, with the pHRI interacting with the underlying human metacarpal through the stiffnesses k_{pHRI} and k_{dorsum} in series at each point. Piece-wise linear values for both stiffness were used, with k_{dorsum} taken from our experimental results. The system was simulated for varying applied force (F_L) and moment loads (M_L) with varying k_{pHRI} profiles to examine the resulting pressure distribution. The relative displacement of the pHRI interface with respect to the underlying bone, due to F_L, was also captured for each stiffness profile, and these results are presented in the next section.

3.2.4 Measurement of hand dorsum stiffness

To measure k_{dorsum}, we designed an indentation system comprised of a Phantom Premium 1.5 high force haptic renderer, which has a high positional accuracy of the end effector ($7 * 10^{-6}$m). This was used along with an ATI Nano 17 force torque transducer (having a high force torque sensing accuracy of 0.001N) attached at the end of the linkage as an indenter to probe the hand dorsum (Fig. 3.8).
We selected five points along a line between the metacarpophalangeal joint and the radial styloid process along the 2^{nd} metacarpal bone, the 3^{rd} metacarpal bone, and along a line between the two metacarpal bones, in the inter-metacarpal region. This region was se-

lected to correspond to the area of the attachment plate on the Maestro exoskeleton. Fig. 3.9 shows the regions selected for indentation.

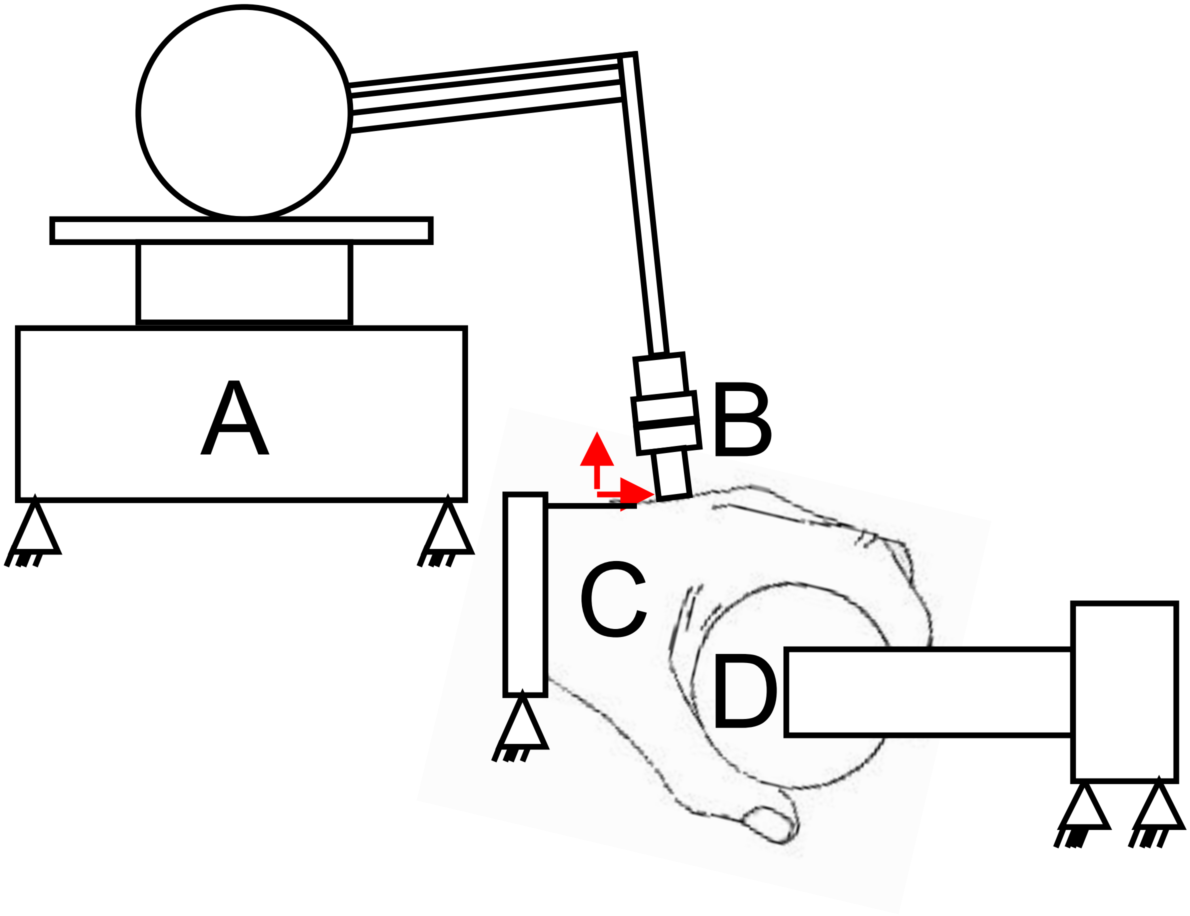

Figure 3.8: Phantom premium 1.5 high force haptic renderer (A), instrumented with an ATI nano 17 6-axis force torque transducer (B), probing the hand dorsum (C) over a spatial grid while the subject grasps a spherical object instrumented with an ATI Nano 17 (D).

A spherical object of diameter 3inches (0.077m), embedded with a 6-axis force torque transducer, was provided to mimic a naturalistic spherical power grasp, and to measure grasp force. The object was grasped with minimum force (0N). The spherical power grasp is a major type in grasp taxonomy [26] and is characterized by thumb abduction and movement of all the metacarpal bones and soft tissue structures in the dorsum. This pose provides a stable surface for the indentation measurements. A consistent grasp pattern was used across trials to minimize its influence on stiffness distributions due to the changes in bone locations and muscle recruitment strategy.

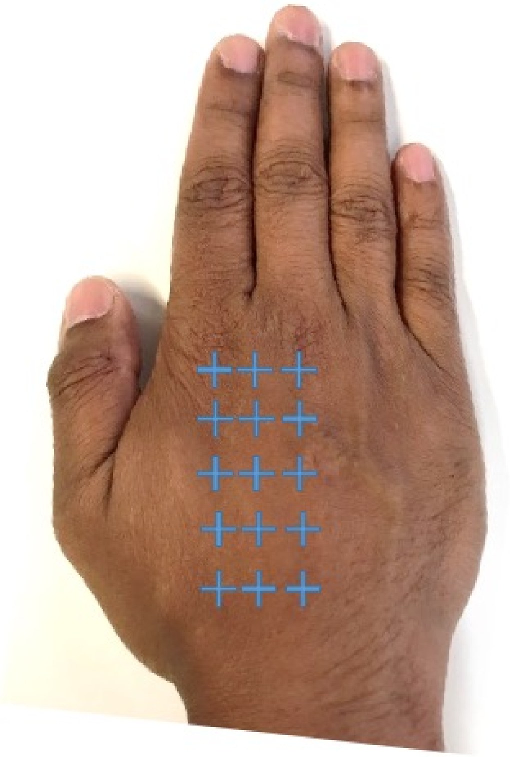

Figure 3.9: Locations of measured stiffness measured over the 2nd & 3rd metacarpal, and 2nd-3rd intermetacarpal region. The blue "+" symbols represent the sites of indentation on the hand dorsum

The wrist and arm were supported in braces, and the grasp object, and the wrist and arm supports were repositioned to level the hand dorsum in the transverse anatomical plane (Fig. 3.8). The phantom probe is then manually led once to each point marked on the dorsum for indentation. The probe uses these points as input into an interpolator to compute a spatial trajectory to follow. The phantom is driven in an open-loop position controlled configuration.

3.3 Methods

Quantifying the stiffness of the indentation system in the direction normal to the hand dorsum demonstrated the need to account for this value in estimating the stiffness of the hand dorsum. The stiffness of the indentation system ($k_{indenter}$) was found to be 2.67 N/mm along the workspace. We account for this stiffness in the measurement of the hand dorsum stiffness (k_{dorsum}) by modeling the interaction between the indentation system and the hand dorsum as two springs in series. The measured stiffness of the hand dorsum, $k_{measured}$, (Fig. 3.10) is used along with $k_{indenter}$ to calculate the k_{dorsum} (5).

$$k_{dorsum} = \frac{k_{measured} * k_{indenter}}{k_{indenter} - k_{measured}} \tag{5}$$

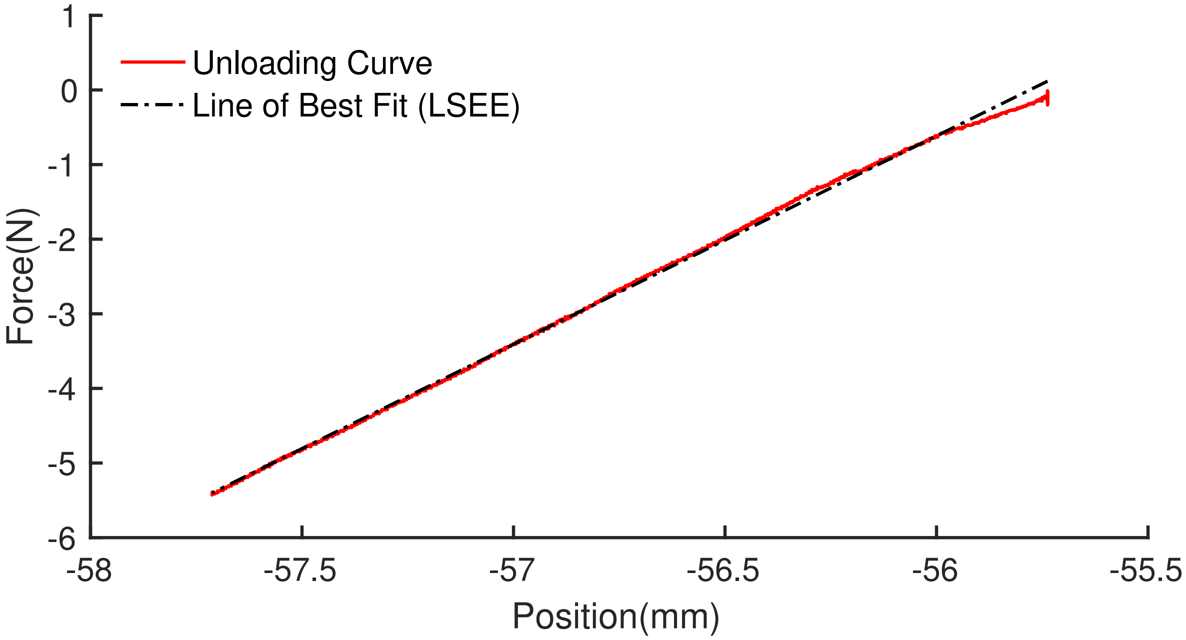

Figure 3.10: Fitting a line to the force deflection curve from indentation experiments. The slope of the fitted line corresponds to the measured stiffness.

We made five sequential repeated measures to estimate the variance in the measured stiffness at each point. The observed variance was attributed to movement in the hand. The hand dorsum stiffness data is collected from one pilot subject only, and with a probe having a square base with $4mm$ edges and $1.5mm$ fillets on each edge to minimize discomfort during indentation. The indenter profile and size were chosen iteratively based on the relative distribution of the hard and soft tissue structures in the hand. Increasing the resolution of the grid beyond the current levels introduced errors due to partial overlap of soft and hard tissue at the points of measurement.

3.3.1 Calculating the optimized padding stiffness

In our model, k_{eff} between the human bone and the Maestro robot's reference plate is comprised of k_{dorsum} and k_{pHRI} in series. Therefore, once we have numerically computed k_{eff}, and measured k_{dorsum} through the indentation experiment, the required k_{pHRI} can be calculated at every point on the attachment surface (6). This gives us a pHRI interface stiffness profile that should generate the minimum peak pressure, or the optimal pressure profile (P_{opt}) on the hand dorsum for the given F_L and M_L.

$$k_{pHRI} = \frac{k_{eff} * k_{dorsum}}{k_{dorsum} - k_{eff}} \tag{6}$$

3.4 Results

3.4.1 Analytical determination of the optimal stiffness distribution

Through an analysis of a simplified two plate model representing the contact between the pHRI interface and the hand dorsum, we found that in order to minimize peak pressures over the hand dorsum, the optimal pressure distribution is comprised of two distinct spatial regions of uniform magnitude (Fig. 3.7). To achieve this optimal pressure distribution profile, we showed that a linear gradient profile of the effective stiffness,((k_{mid} - k_{edge})/k_{mid}) tapering from the center to the edges was a possible solution.

3.4.2 Numerical computation of the desired stiffness profile

From the linear gradient profile of the desired effective stiffness described in the analysis (Section III.A), we evaluated the behavior of the entire system, across a range of parameters, with the custom-built numerical simulation environment (Section II.C). Through repeated simulation across the space of applied external moments, bias forces which represent the strap force holding the pHRI interface to the hand dorsum, and stiffness gradient which describes the spatial distribution of the effective stiffness over the pHRI interface, we characterized the effects of these parameters on our primary performance metric, the peak pressure P_{peak}, experienced over the hand dorsum.

From the results of the numerical simulation (Fig. 6.4), we observed that P_{peak} is minimum at the stiffness gradient of 0.6 for $15N$ of bias force under M_L of 0.3 Nm. This surface is a visual representation of the sensitivity of P_{peak}, a proxy for user discomfort, to stiffness gradient and the bias force.

3.4.3 Hand dorsum stiffness

The stiffness of the hand dorsum was measured and characterized with five repetitions over each of the 15 chosen points, distributed equally over the 2^{nd} metacarpal, 3^{rd} metacarpal and the inter-metacarpal gap between these bones on a single subject's hand (Fig. 6.5).

On average, k_{dorsum} was measured to be 1.0876 ± 0.40 N/mm over a range of from 0.54 N/mm to 1.59 N/mm. The region of the dorsum above the metacarpal bones was found to be stiffer (1.1285 ± 0.43 N/mm) than the region between the bones (1.0060 ± 0.36 N/mm) that accommodate soft tissue. Increasing force of grasp led to an increase in measured dorsum stiffness (Fig. 6.5), however, the pHRI interface stiffness computed here is for a grasp force of 0 N.

3.4.4 Optimal pHRI interface stiffness

The stiffness of the optimal pHRI interface was computed from the numerically determined k_{eff} and the k_{dorsum} (6), for each point on the hand dorsum (Fig. 3.13), for a force

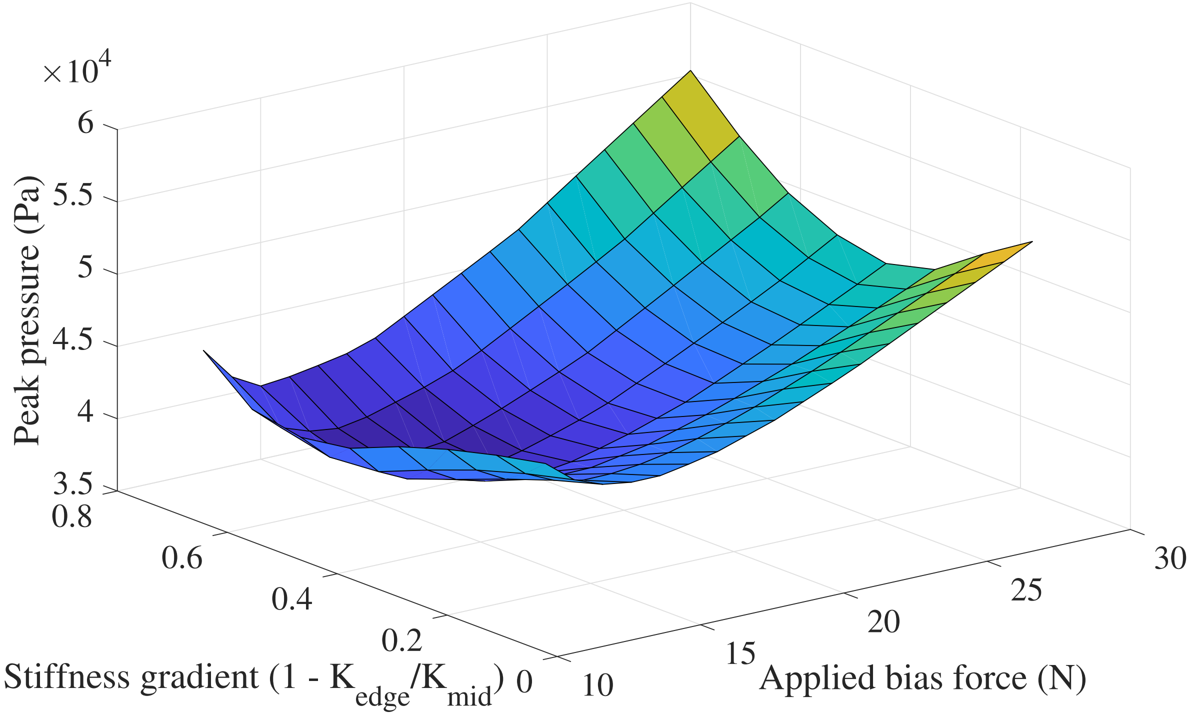

Figure 3.11: Effect of varying bias force and stiffness profiles on the peak pressure across the interface. The minimum satisfies the calculated values of optimal bias force in equation 3.

of grasp of 0N. On average, the k_{pHRI} was found to be 1.6460 ± 1.47 Nm. The pHRI interface over the metacarpal bones was less stiff (1.3478 ± 0.8054 Nm) than the pHRI interface between the bones (2.2424 ± 2.33 Nm), demonstrating that loading the soft tissue to a higher degree minimizes the P_{peak}.

3.4.5 Relationship between design parameters

From the numerical simulation outlined previously (Section II.B), we quantify the effects of varying applied moments, bias forces and stiffness gradients on our primary performance metric of peak pressure experienced at the interface. When compared to a uniform stiffness distribution (stiffness gradient of 0), we observe an improvement in P_{peak} for all cases of M_L when the k_{eff} is varied as a gradient from the center to the edge. With increasing

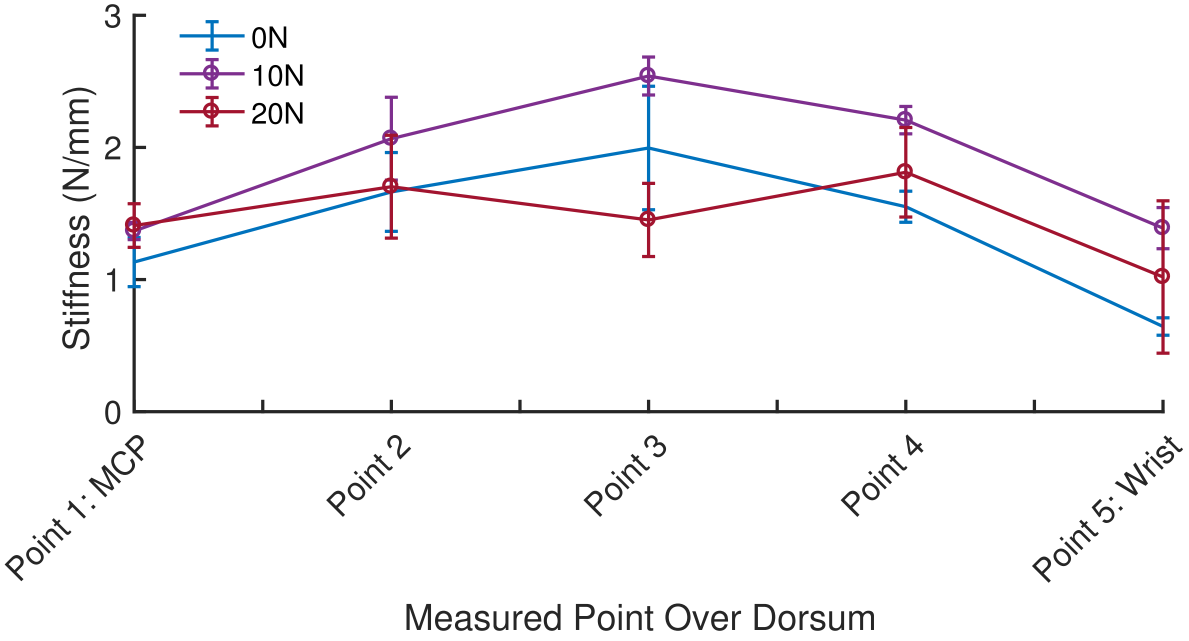

Figure 3.12: Measured stiffness of the hand dorsum for five equally spaced points along the second metacarpal at three levels of grasp force applied by the subject.

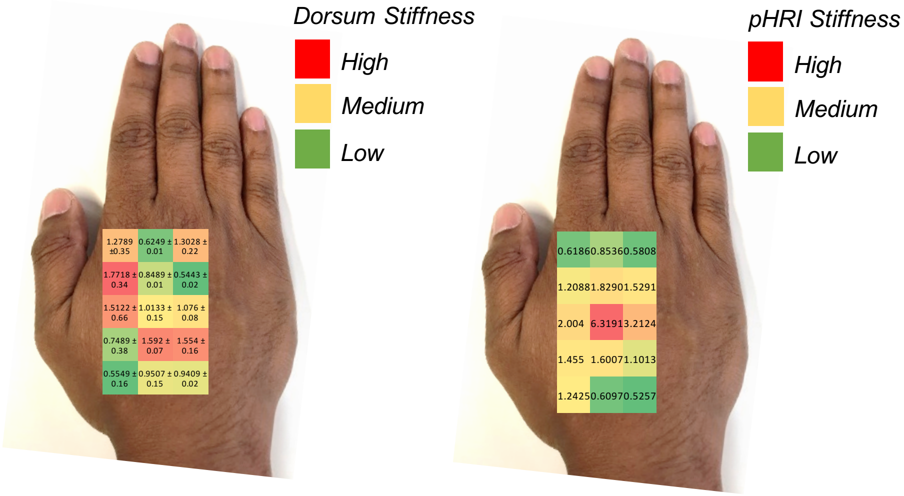

1.2789 ±0.35	0.6249 ± 0.01	1.3028 ± 0.22
1.7718 ± 0.34	0.8489 ± 0.01	0.5443 ± 0.02
1.5122 ± 0.66	1.0133 ± 0.15	1.076 ± 0.08
0.7489 ± 0.38	1.592 ± 0.07	1.554 ± 0.16
0.5549 ± 0.16	0.9507 ± 0.15	0.9409 ± 0.02

0.6186	0.8536	0.5808
1.2088	1.8290	1.5291
2.004	6.3191	3.2124
1.455	1.6007	1.1013
1.2425	0.6097	0.5257

Figure 3.13: Heat maps of the measured dorsum stiffness (left) and the calculated optimal pHRI stiffness for each corresponding point (right).

M_L, we observe the percentage improvement to become more pronounced (Fig. 3.14). Additionally, the optimal value of stiffness profile gradient is dependent on M_L, and is seen to increase linearly with the ratio (M_L/F_L).

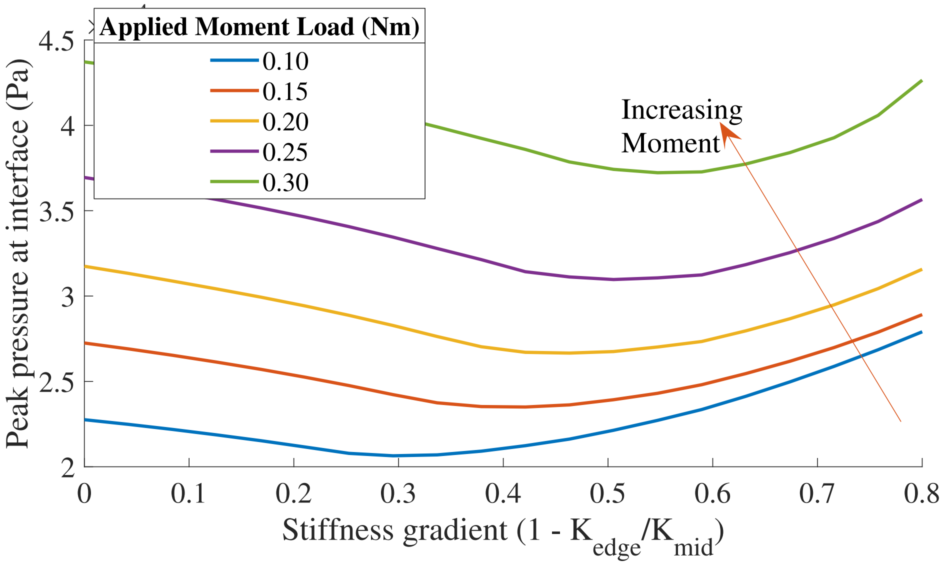

Figure 3.14: Plot of peak pressure on the interface surface for varying stiffness profile gradients, at each value of applied moment load, with the applied bias force held constant.

The simulation confirms the expected outcome that the highest values of P_{peak} are observed at the highest M_L for all conditions of the k_{eff}. Therefore, the optimal stiffness profile is tuned for the highest M_L that the specific device will experience. With this condition, we can observe a 15% improvement in P_{peak} experienced by using a stiffness profile gradient of 0.6 from the center to the edges of the attachment, for the highest M_L of 0.3Nm. These loading conditions are derived from the Maestro exoskeleton.

While minimizing user discomfort is critical, other performance metrics including the relative displacement across the pHRI interface can also be examined with this approach. When considering the effect of these same input variables of bias force and stiffness gradient on the relative displacement, it becomes evident that we have a trade-off between our performance metrics of comfort and relative displacement. Fig. 3.15 shows the effect on relative displacement due to a change in stiffness profiles with the applied force and moment loading held constant. Contrary to the effect on peak pressure shown earlier, the relative displacement increases with the stiffness profile gradient.

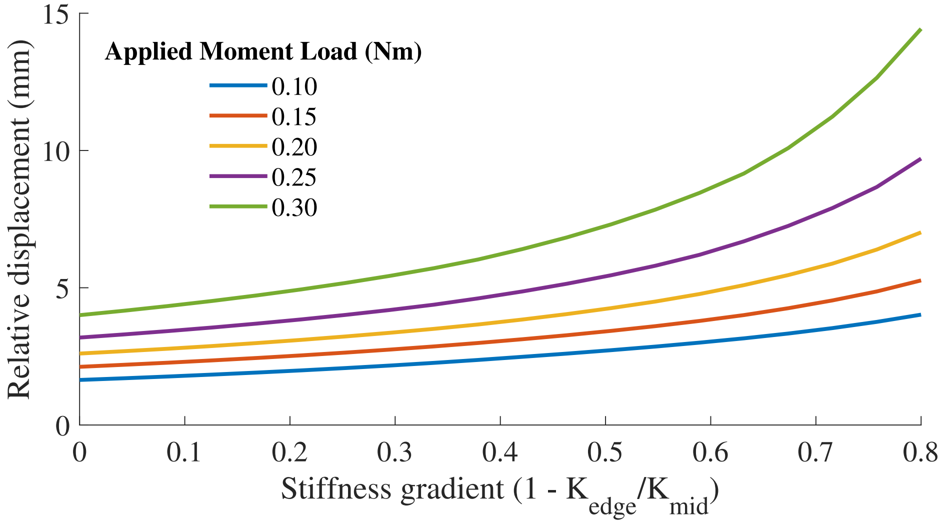

Figure 3.15: Plot of the effect on relative displacement between the robot reference and the human skeleton on changing the stiffness profile gradient of the pHRI. Each line represents the effect due to a change in the pHRI stiffness gradient while holding the applied moment constant.

This is more clearly illustrated in Fig. 3.16, where the two output metrics are plotted against the stiffness profile gradient on identical x-axes. It shows that increasing the stiffness profile gradient to improve the peak pressure across the interface has an adverse effect on the relative displacement.

We also observe a similar trade-off between peak pressure at the interface and relative displacement while varying bias force (Fig. 3.17).

3.5 Discussion

Our analysis of the force distribution at the pHRI interface showed that under force and moment loading, the performance metric of peak pressure at the contact surface can be minimized by using a spatially varying stiffness distribution of the pHRI interface. A so-

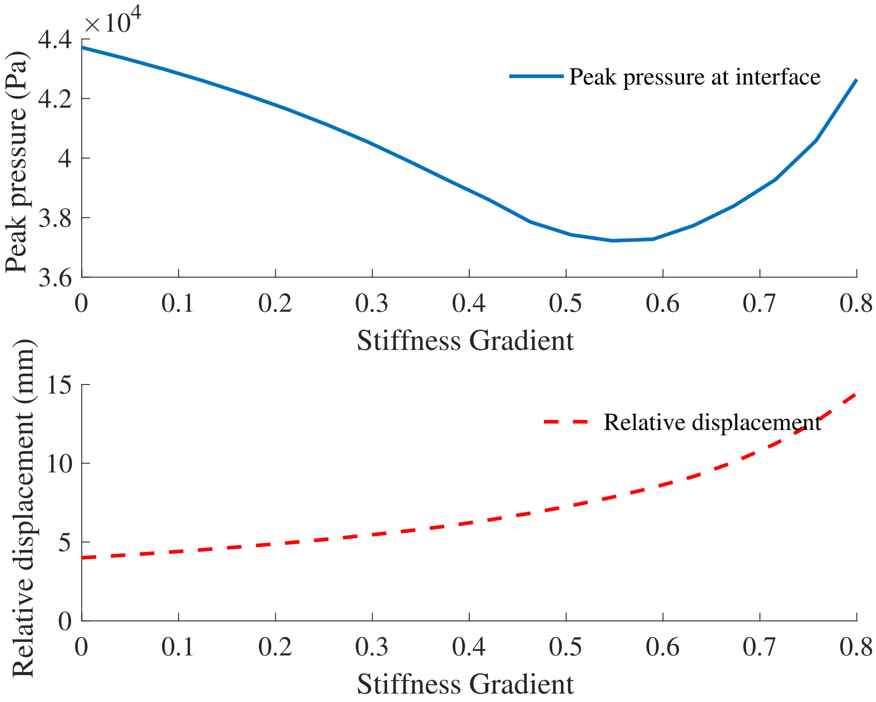

Figure 3.16: Trade-off between peak pressure (as a measure of user comfort) and relative displacement on varying the stiffness profile gradient.

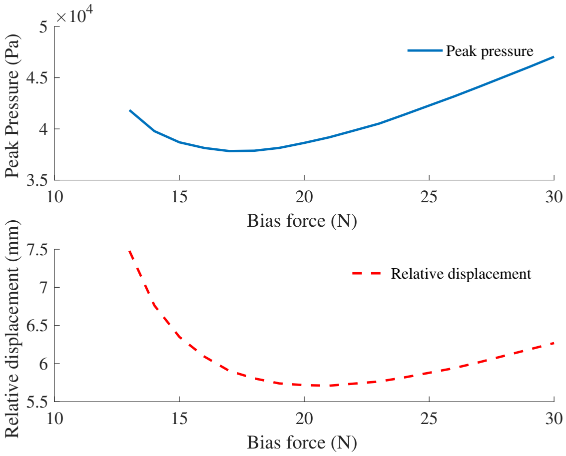

Figure 3.17: Trade-off between peak pressure and relative displacement on varying the bias force applied.

lution that gives us this optimal force distribution was shown to be a linearly decreasing stiffness gradient from the center to the edges of the pHRI interface.

The performance of the effective stiffness gradient was numerically quantified using a MATLAB based simulation engine. By simulating a range of applied bias force and stiffness gradients, we are able to show a minimum in the peak pressure as predicted by our analytical model. This optimal stiffness gradient showed a 15% reduction in peak pressure over the hand dorsum when compared with uniform stiffness, under external loading of 0.3Nm. It should be noted though, that the value of optimal stiffness gradient between the human and the exoskeleton is dependent on the applied moment, M_L. Since the largest peak pressures experienced by this system are always under the conditions of highest applied moment loading, we must therefore consider the highest moment that our system is likely to experience when computing the k_{eff}.

The optimal effective stiffness gradient described above denotes the effective stiffness of the pHRI interface and the soft tissue on the human dorsum acting in series. Therefore, in order to design the pHRI interface to a desired stiffness profile, the knowledge of the dorsum stiffness is an important parameter to quantify. Our pilot experimental study characterized the spatial range and distribution of dorsum stiffness on a single hand. The measured stiffness values at the MCP joint are lower than originally anticipated, which could potentially be due to the soft extensor tendon hood over this region. The measured dorsum stiffness data provides us with initial values necessary for pHRI interface design methods presented here. Systematically characterizing the dorsum stiffness across the hand pose and grasp force for multiple subjects will help further clarify the underlying relationships dictating optimal pHRI design that we have demonstrated here, for the first time.

With numerical values available for both the desired effective stiffness distribution and the measured dorsum stiffness, we are able to inform the design of the pHRI interface stiffness. This is the only stiffness property available to controllably design, as the properties of the human tissue cannot be changed. Since the optimal effective stiffness (between the human bone and the robot reference) is the series equivalent of the pHRI interface stiffness and the stiffness of the human dorsum, the optimal pHRI stiffness is calculated from the knowledge of both the optimal effective stiffness and the measured dorsum stiffness. This is why the characterization of both is essential to this method. A generalizable takeaway from this study is that a pHRI interface designed to reduce P_{peak} exerted under moment loading must have regions of low k_{eff} towards the edges. In design, this region of low stiffness can be achieved by using more compliant padding near the edges.

The design changes presented can potentially help reduce user discomfort by reducing the peak pressure applied on the human at the contact surface. However, we showed that these same changes can adversely affect another performance metric of coupled human-robot systems: the relative displacement of the attachment with respect to the human skeleton. The trade-off between the two performance metrics of user comfort and relative displacement on varying our design inputs of stiffness gradients and bias forces will help make informed design choices, driven by the desired requirements of our application.

3.6 Conclusion

The primary contribution of this paper is a new design method for pHRI interfaces that minimizes the peak values of concentrated pressure applied to the hand dorsum by the use of a spatially varying stiffness profile. This method is informed by calculations of the optimal pressure distribution as well as experimental measurement of stiffness of the human hand dorsum. By characterizing the effect of the proposed non-uniform pHRI interface stiffnesses on the relative displacement between the hand and the exoskeleton, we highlight the need to keep relative displacement in mind while optimizing for the minimal peak pressure distribution. This is also the first study, to our knowledge, that leverages the measured biomechanical characteristic of stiffness of the human hand to design an optimal interface stiffness profile.

This study provides a starting point for our ongoing work of in-depth characterization of the interaction between exoskeletons and the human hand. The analytical and simulation results based on performance metrics shown to influence user comfort provide us with an important direction in designing better pHRI interfaces. Further research involving human subject studies will be important in validating the results presented here and for examining user comfort and sustained use of devices. Further study will also focus on extending the generalizability of the findings in this paper. These methods can be expanded to characterize more complex bias or strap systems, and will be used for proposing further design guidelines for the development of attachment devices in coupled human-robot systems. This novel approach of quantifying body stiffness, and optimizing pHRI interface designs to minimize irregularities in pressure distribution at contact surfaces between humans and exoskeletons can be used to design other wearable devices for the hand, and should be extendable to designs for other limbs.

Chapter 4

CHARACTERIZATION OF STIFFNESS OF TISSUES AT THE WRIST FOR THE DESIGN OF WEARABLE DEVICES

Gaurav Mukherjee[1], *Ali Israr*[2], *Elia Gatti*[3], *Patrick Aubin*[1,4], *Eric Rombokas*[1,4], *Raymond King*[2]
1. Department of Mechanical Engineering, University of Washington, Seattle, WA 98195, USA
2. Facebook Reality Labs, Redmond, WA 98052,
3. Dr. Gatti is now with Amazon, London, W6 9LA, UK, 4. Center for Limb Loss and Mobility (CLiMB), VA RR&D, Seattle, WA 98108, USA

4.1 Abstract

Wearable devices such as orthoses and vibrotactile haptic devices experience loss in performance when physically coupled to the body. Coupling to soft tissue reduces the device's ability to exert force to induce the desired motion. Significant mechanical power is expended in compressing the viscoelastic tissues of the body. Currently, these issues are overcome by increasing the coupling pressure between the device and the body. However, this leads to increased discomfort.

To couple wearable devices to the body comfortably and to maximize device performance, we must design the human device interface (HDI) by considering the mechanical characteristics of the tissue structures. A necessary first step, and the focus of this work, is to identify and characterize the appropriate mechanical properties of the tissue structures of the body. Using a custom robotic indenter, we characterize the stiffness of human tissue at the wrist for the design of comfortable and efficient wearable devices.

We find that stiffness of tissues changes with locations around the wrist, and with coupling

pressure. We find that stiffness is higher over bone rich locations as compared to soft tissue rich locations. As coupling pressure increases, the stiffness over both bone rich and soft tissue locations increases. These findings demonstrate that the mechanical response of the tissue to loading changes with coupling pressure, and location on the wrist. Therefore, to truly optimize the design of the wearable device, we must account for the different properties of the human wrist.

4.2 Introduction

The skin and the underlying tissues at the wrist act as the interface for wearable devices, including prostheses, exoskeletons and haptic displays. Whether we aim to couple devices comfortably to the body, or to convey rich information via touch, this tissue interface forms the natural conduit. Designing wearable devices without considering the mechanical behavior of the underlying tissues may cause injury due to the mismatch of mechanical impedance [4], or it may result in poor communication of signals from a haptic display to the body [27].

While the mechanical behavior of the skin layer to perturbation have been quantified at different discrete locations on the body with an abundance of soft tissue [[**?**, **?**, 4]], wearable devices such as haptic displays are coupled to entire anatomical cross-sections with varying tissue composition. As a result, the mechanical behavior at the device-body interface may have a vastly heterogenous profile around a cross-section of a limb [28]. The wrist is a popular anatomical cross-section for coupling wearable haptic displays. Cutaneous displays such as those in smart watches (Apple Watch and Fitbit Surge), as well as novel kinesthetic displays [**?**, 29] are being developed to transmit haptic information across this anatomical region, however, the mechanical response of the wrist have not been characterized. The goals of this paper are to quantify the variability of mechanical response about the wrist, and to present a candidate path for modeling this behavior to assist in the development of wearable haptic displays.

We address these goals by quantifying the mechanical response of the tissue structures, at candidate sites about the wrist, to static and dynamic loads. Prior research has quantified the use of indentation and suction type techniques to quantify the mechanical response of the skin layer alone to small static loads [30]. Of these methods, indentation tests are the closest emulation of the coupling forces present at the device-body interface for both, cutaneous and kinesthetic squeeze type displays. This paper's specific contributions are as follows:

- Quantification of the force displacement relationships around the wrist across 13 subjects.
- An analytical model of the mechanical response of the wrist based on the force displacement data.
- Quantification of the relative effects of anatomical locations, indenter sizes and velocity of indentation about the wrist on the mechanical response to indentation loading.

The following sections describe the design of the experiments, the design and validation of the apparatus, and our approach to modeling the wrist's response to large quasi-static indentations, and harmonic oscillations at different frequencies and coupling pressures.

4.3 Methods

4.3.1 Study Design

The biomechanical response to indentation of tissue about a cross-section of the wrist is composed of the individual mechanical responses of different layers of tissues, ranging from skin, adipose tissue, fascia, tendons, vascular structures, ligaments and bones. To examine the variability in the mechanical response to the static loading of the wrist cross-section, we designed an experiment driven by the hypothesis that the stiffness of the wrist tissue composition is a function of the location around the wrist. We further hypothesized that the stiffness of the tissue varies as a function of the depth of indentation into the skin.

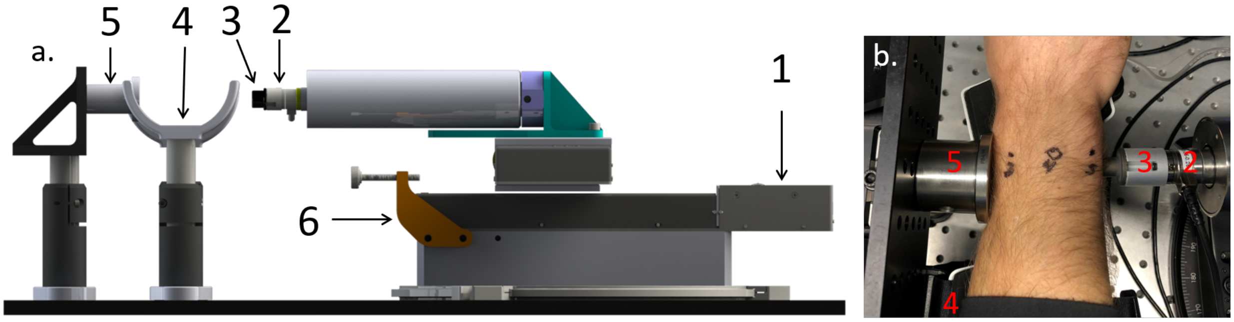

Figure 4.1: a. Wrist Impedance Measurement Platform: 1. Translation Stage, 2.6-axis load cell, 3.Contactor, 4.Arm rest, 5.Reaction wall, 6. Adjustable mechanical stop; b. Arm resting on arm rest and being indented over position corresponding to ulnar bone. Note that the reaction wall and indenter are angled to support the arm with a flat surface, and to indent the arm in the normal direction to the anatomical topology, respectively.

To test these hypotheses, we designed an experiment to quantify the force and displacement during indentation of four distinct anatomical locations (tendon, radial styloid process, dorsum and ulnar styloid process) about a cross-section of the wrist across 13 subjects. We decided to vary indenter diameters (10 mm and 15 mm), across two velocities (1 mm/s and 4 mm/s.) and 3 forces (1 N, 3 N, 5 N). We used a block design for locations and indenter sizes, and we randomized across target forces and velocities with six trial repetitions for each condition for a total of 288 trials per subject.

A two pronged approach was adopted for the data analysis: In the first approach, we decided to estimate the stiffness of the tissue independently from the loading and unloading sections of the measured force and displacement data at each location, for a depth of indentation between 0.5 mm to 3 mm at 0.5 mm increments. We fit a first order linear model using the maximum likelihood estimation over a 100ms window around the depth of interest across the six repeated trials for each condition. In the second approach, we decided to fit single exponential curves independently to the loading and unloading sections of the trials corresponding to the maximum loading (5 N) in our experiment.

4.3.2 Apparatus Design And Characterization

Design: Wrist Impedance Measurement Platform

The wrist impedance measurement platform (WIMP) is a custom robotic indentation system, which is designed to deliver a precise displacement at different points about a participant's wrist, and to measure the resulting reaction force. The WIMP is comprised of an indentation stage and an arm rest attached to a vibration isolation optical table (Thorlabs, UK). The indentation stage is equipped with an ATI Nano 17 load cell (ATI Inc., USA), coupled to a translation stage (LTS 150 Thorlabs, Inc., UK). The overall stiffness of the indentation system is $k_{system} = 1.128 \times 10^3 N/mm$. This was calculated based on a series spring model, comprised of the load cell ($k_{loadcell} = 1.1 \times 10^4 N/mm$) and the translation stage ($k_{stage} = 1.256 \times 10^3 N/mm$), which is similar to the reported stiffness of cortical bone in prior indentation studies ($k_{bone} = 1.595 \times 10^4 N/mm$). Indentation force is applied on the location of interest by punch-type flat circular contactors of either 10 mm or 15 mm diameter. The contactor is hard anodized (Type 3) to ensure electrical and thermal isolation from the subject. The indentation system is assembled on a rotating optical plate to allow for angular alignment with the participant's arm.

The arm clamp was designed with cup type supports below the elbow and palm, and a cylindrical reaction wall which opposed the movement of the arm when an indentation was applied. The elbow and hand supports as well as the reaction wall were adjustable in height as well as in planar location on the optical tabletop. This design allowed the experimenter to adjust the fitting to accommodate variations in the participant's height and arm dimensions to maximize comfort and to minimize unintentional movement.

The WIMP is equipped with redundant safety features - An adjustable stage translation limiter (Fig. 4.1. a.) allowed us to set the maximum travel for the stage towards the participant's arm such that the highest achievable force was 5.5 N. This adjustment was performed during the wrist calibration process with the participant's arm in place. Additionally, an electrical stop was placed within arm's reach of the participant which cut off power supply to the translation stage of the WIMP. In conjunction with quick releases on the arm rest, this allowed a redundant physical safety feature. Software safety features such as a pause functionality and a default off state were programmed into the device and tested repeatedly before experimentation. A second investigator was present as a spotter for the participant during the entire experiment.

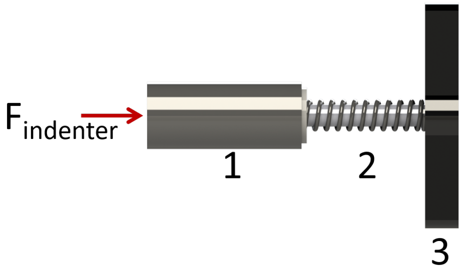

Figure 4.2: A precision compression spring mechanism to characterize the WIMP. The parts of the mechanism are: 1. Aluminum cap with a centering hole of diameter 15mm with an oiled brass sleeve insert; 2. Precision compression spring on a pull-out dowel guide; 3. Aluminum base plate with mounting holes; $F_{indenter}$ represents the force applied by the WIMP indenter to compress the spring.

Device Characterization

To characterize the WIMP, we developed a custom low friction spring loading mechanism (4.2) to quantify how well the device would be able to estimate the stiffness of a spring with a known spring rate. The characterization mechanism is comprised of a pull-out dowel housed in a steel plate on one end, with mounting holes matching those on the bracket attached to the reaction wall on the WIMP (4.1). The pull-out dowel acts as a guide for a cup with an oiled sleeve bearing, a washer and a precision compression spring captured between the steel plate base and the washer. The cup has a 15 mm diameter centering hole to align the indentation stage. A precision compression spring of known spring rate (

$k_{spring} = 0.359 N/mm$: Part No. C10-022-048, Jones Spring Co., Kentucky, USA) was compressed to a target force of 5N using the WIMP, and the spring rate was estimated from a linear curve fit on the loading and unloading curves of the resulting force displacement curves.

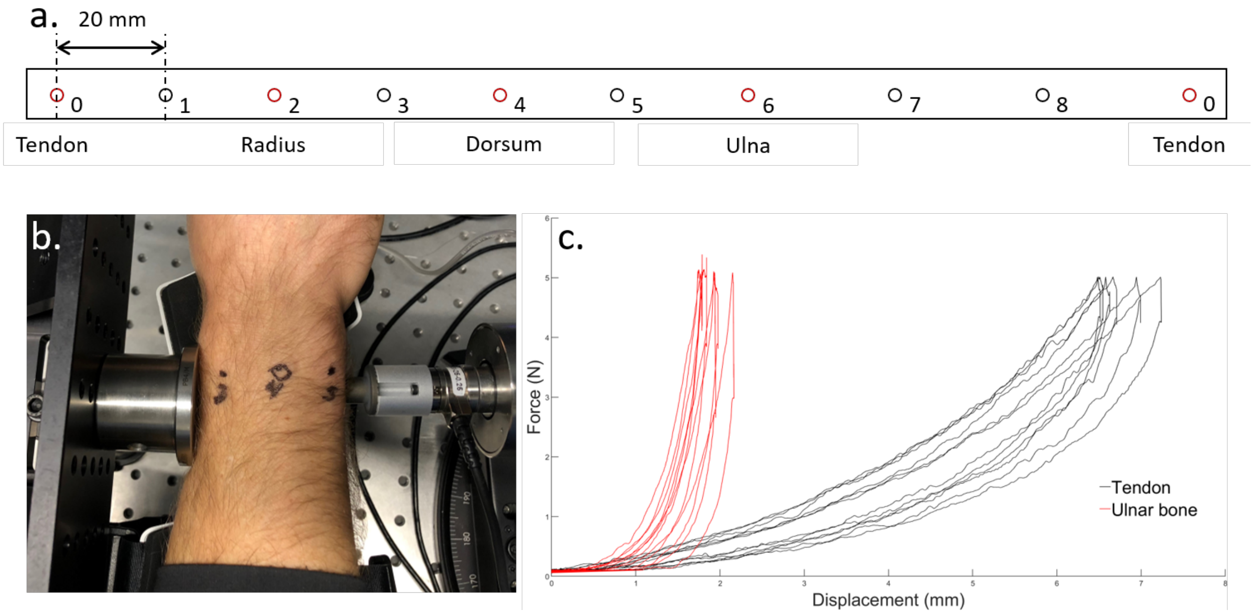

Figure 4.3: Wrist Calibration And Measurement Approach a. A representation of the paper metric scale with holes used to align the anatomical landmarks on the wrist to a common measure. The red circles demonstrate the points that aligned with the anatomical landmarks for a sample participant; b. A calibrated wrist being indented over the ulna, with support from the reaction wall to prevent movement; c. A representative force displacement plot from 6 repetitions from one participant - indentations over ulna and tendon.

4.3.3 Experimental Protocol

14 healthy participants (4 female, median age: 31 Years (male), 27 Years (female), median wrist circumference: 173.5 mm (male), 152 (female)) volunteered to participate in a study approved by an internal environmental health and safety review at the Facebook Reality Labs, Redmond, WA. One participant was excluded due to difficulties in maintaining a

static pose throughout multiple trials in the prescribed duration of the session.

The subjects were introduced to the experiment, the apparatus and the safety protocol for the experiment. After obtaining consent, measures such as height, weight and wrist circumference were collected.

To account for the variability in the size and shape of wrists across participants, we mapped the locations of the four indentation locations to a linear graduated scale. Participants were seated at a table and a metric paper tape measure (width, 22 mm), punched with holes of 4 mm diameter placed 20 mm apart, (Fig. 5.2. a.) was attached to the wrist on the right arm such that the center of the holes were 11 mm proximal to the prominence of the ulnar styloid process on the wrist. The first location, indexed at 0, was aligned to lie on the volar aspect of the wrist along the long axis of the forearm, between the elbow and the third digit of the outstretched hand over the flexor tendons. The holes in the paper tape which were closest to three other anatomical landmarks, namely the radial styloid process, the dorsum and the ulnar styloid process, were used to mark the wrist for indentation (Fig. 5.2. b.). Following the calibration procedure, participants were seated on a height adjustable lab stool with their right forearm placed in the arm clamp (Fig. 4.1). The participant's arm was rotated to ensure flat contact of the target position on the wrist with the indenter (Fig. 5.2. b.), and the participant was given detailed instructions about the experiment, and was asked to drive the indentation stage to experience the highest loading levels expected during the trial. Participants also familiarized themselves with the use of the emergency stop button and the pause functionality. The mechanical stop was adjusted to prevent the movement of the translation stage towards the arm once the highest target force had been achieved.

4.4 Results

4.4.1 Characterizing the WIMP

To characterize the WIMP, we indent a precision compression spring of known spring rate ($k_{spring} = 0.359 N/mm$) to the maximum loading in our proposed experimental protocol (5N) and estimate the stiffness from a linear fit to the loading and unloading curves. Fitting a linear model to the loading curves for 6 trials using the maximum likelihood estimation algorithm yields a stiffness estimate of 0.376 N/mm (p-value = 0.00) which is an overestimation by 4.76% (Fig. 4.4).

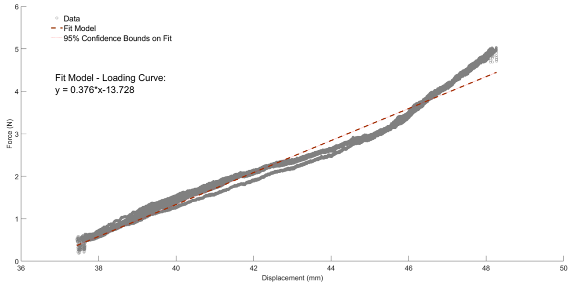

Figure 4.4: Estimation of spring stiffness from a linear fit over loading data

4.4.2 Quantification of stiffness about the wrist

In this study we indented four tissue sites about the right wrists for 13 participants under different velocities, indenter diameters and at different load levels as described in the methods above. We recorded the reaction force and displacements throughout the indentation and relaxation phases. We took two approaches to analyzing the force displacement data. We computed stiffness at the different locations about the wrist at depths of indentation ranging from 0.5 mm up to a depth of 3 mm by fitting a straight line using the maximum likelihood estimate algorithm to a 100 ms window (100 data points) centered at the target depth of indentation on the loading and unloading curves separately (Fig. 4.5). In both the loading and the unloading sections, as seen on the semi log plots (Fig. 4.5), the average stiffness estimated from the empirical data were significantly higher at the two positions corresponding to the location of the radial and ulnar styloid processes $(1.85 + / - 0.7N/mm)$ as compared to the the softer tendon and dorsum $(0.47 + / - 0.13N/mm)$. We also observe that the stiffness tends to increase with increase in indentation depth, with the rate of increase over the bony regions being greater than that over the regions of relative abundance of soft tissue structures.

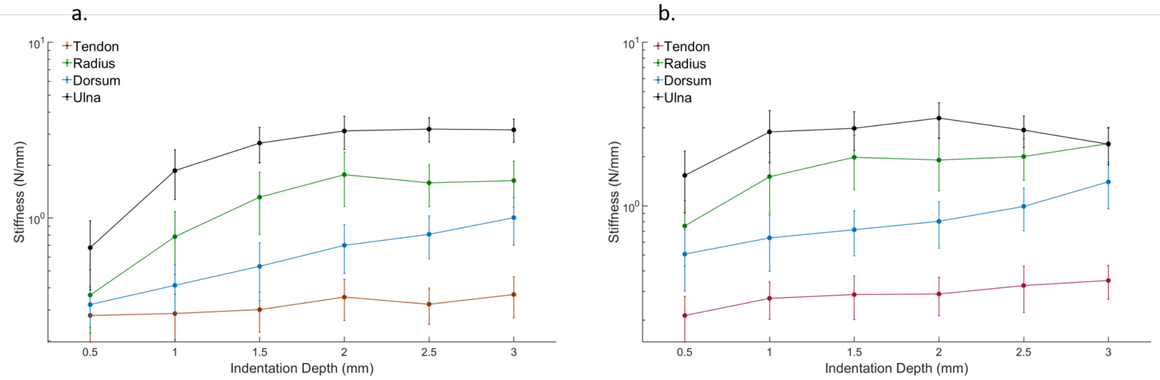

Figure 4.5: Stiffness computed from measured data. Panel a. represents fits to loading section data. Panel b. represents fits to unloading section data

4.4.3 Modeling the mechanical response of the wrist

From the indentation experiments, we approximated the variation of force from the loading and unloading phases with two separate exponential functions of the form: a ex p(bx) (one for each phase). The a and b parameters were obtained by fitting the data using a maximum likelihood estimation-based algorithm. The average goodness of fit was $R^2 = 0.82 + / - 0.12$ in the unloading phase, and $R^2 = 0.88 + / - 0.08$ in the loading phase.

The coefficients a and b represent the gains or coefficients of the base and exponent for the exponential functions fit to the data. Physically, they represent the rate of change in force with indentation of the tissue. In this analysis, we tested whether the experimental conditions, namely location of the indentation, velocities of indentation, and indenter size

Location	Loading		Unloading	
	Coefficient a	**Coefficient b**	**Coefficient a**	**Coefficient b**
Tendon	0.37 ±0.19	0.25 ±0.07	0.21 ±0.08	0.29 ±0.08
Radial Styloid Process	0.18 ±0.21	1.03 ±0.46	0.09 ±0.08	1.35 ±0.53
Dorsum	0.35 ±0.28	0.47 ±0.20	0.13 ±0.09	0.62 ±0.26
Ulnar Styloid Process	0.38 ±0.44	1.13 ±0.60	0.11 ±0.09	1.91 ±0.70

Figure 4.6: Average fit coefficients from the exponential functions fit to the loading and unloading section respectively

had a statistically significant effect on the coefficients of the exponential function fit to the data.

To test this, we run a multiple-way repeated measures MANOVA. The fit coefficients for loading and unloading are treated as separate dependent variables, and the 4 locations, the 2 indenter sizes and the 2 indentation velocities are treated as independent variables. Modified ANOVA Type Statistics (MATS) for the velocity and indenter size showed no significant effect on the gain coefficients of the exponential function ($p > 0.22$). Location was the only statistically significant variable ($pvalue < 0.001$).

We ran follow-up repeated measures one-way ANOVAs and post-hoc t-tests with Bonferroni corrections for each coefficient (a and b) with location held as the independent variable. Results showed that during loading, the base coefficient a was significantly different across all the locations ($p < 0.05$) except for the pairwise comparisons between tendon and dorsum ($p = 0.07$), between radius and ulna ($p = 0.46$), and between dorsum and ulna ($p = 0.06$). The exponent coefficient b was significantly different for all the pairwise comparisons between locations ($p < 0.001$).

In the unloading phase, the base coefficient a was statistically different between tendon and all the other locations ($p < 0.01$). No difference was found in any other pairwise comparison ($p - value > 0.25$). Similar to the loading phase, the exponent coefficient b in the unloading phase was significantly different for every pairwise comparisons between locations ($p < 0.05$).

Differences in the exponential fit between the loading and unloading phases

After assessing the effects of location, velocity, and indenter size on the fit coefficients of the exponential functions, we focused our analysis on the difference between the coefficients obtained from loading and unloading data. This analysis was aimed at identifying any hysteretic behavior of the tissue in the loading and the unloading phase.

We run a 2-ways repeated measures MANOVA on the base and exponent coefficients of the exponential functions with phase (loading or unloading) and location as independent variables. We decided to include location in the current statistical model to test interactions between phase and location, that is: whether hysteretic behavior was a function of locations around the wrist. Results from the MANOVA showed that location, phase, and interaction between phase and location where statistically significant ($p - value < 0.001$) confirming the presence of hysteresis. We then run separate post-hoc ANOVAs and pair-wise t-test with Bonferroni correction for both the exponent and the base coefficients.

The ANOVAs on the two coefficients showed main effects of both phase and location, as well as a significant effect of the interactions ($p < 0.0001$). The main effects of phase and interaction can be discussed as follow: the exponent coefficient was higher during unloading, indicating a faster change in the reaction force obtained from the displacement of the skin. On the other hand, the base coefficient a, was significantly higher during the loading phase, meaning that given the same displacement, during the loading phase the skin was delivering higher reaction forces than during the unloading phase. Moreover, the significant effect of the interaction showed that the extent of such hysteretic behavior, although always present (main effect of phase) was different across locations (Fig. 4.7).

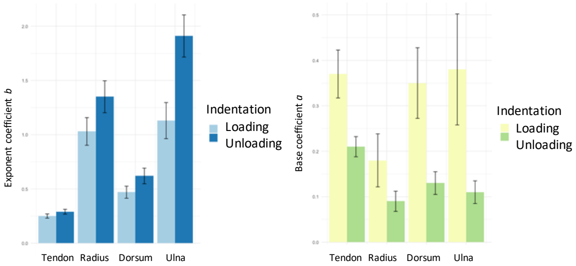

Figure 4.7: Stiffness varies significantly with location

4.5 Discussion

4.5.1 A simple exponential model is predictive of empirical data

The stiffness estimated from the exponential models fit to the loading and unloading curves demonstrate similar behavior to that observed from the local linear fits applied to the measured data (Fig. 4.8). This observation demonstrates an interesting path forward for prescribing engineering metrics for haptic display design.

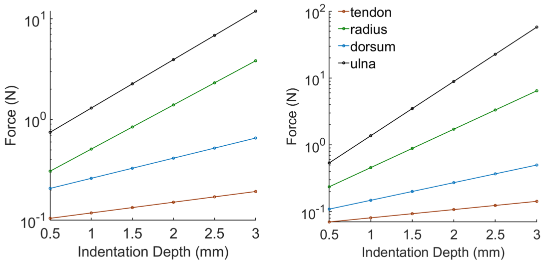

Figure 4.8: Stiffness computed from exponential fit. Panel a. represents fits to loading section data. Panel b. represents fits to unloading section data

4.5.2 Classical approaches to modeling the mechanical impedance to indentation may be insufficient for deeper tissue indentation

The mechanical impedance response for a low load appears to be similar for both bony and soft tissue regions (Fig. 4.5). Our data indicates that there is a 1 mm range over soft tissue and bone that represents the skin (Fig. 5.2 c.). Beyond this, non-linear regions are engaged at relatively low loads. If the target range of coupling force or squeeze force is greater than 0.5 N then deep tissue mechanics over a given anatomical region need to be accounted for in the haptic display design process.

4.5.3 Implications of the knowledge of mechanical impedance on haptic actuator design

High variability in stiffness impacts the design of the haptic display, especially resonators with sharp frequency bandwidths or high q-factors. Also, as compliant wearable haptic displays become more prevalent [**?**], the relative effect of the tissue mechanical properties on display design will increase. The ability to prescribe desired haptic signals with increasing coupling force require a quantification of the response of the tissue site to mechanical coupling loads. As an example, the field of squeeze haptics presents an interesting case study where the variation of coupling force between the display and tissue sites around the coupling region on the body may affect the signal that is transmitted to the user. The high variability observed in the mechanical impedance at different indentation depths around the wrist demonstrates a need to account for this variability in the design of the haptic signals targeted at different squeeze levels [**?**].

4.6 Conclusion

We quantified the mechanical response of the tissues at the wrist to indentation loading at 4 candidate sites across 13 participants. We presented a modeling approach for the observed mechanical response data and demonstrated that location about the wrist significantly affected the mechanical behavior of the wrist to indentation forces. We also demonstrated a clear increase in mechanical stiffness with indentation depth, which implies that the mechanical behavior of the tissues about an anatomical cross-section change when devices are coupled to them. This finding is important to consider for the design of wearable devices including haptic displays to ensure that we can transmit desired information to the users of these wearable devices.

In the characterization of our indentation device, an average error of 4.76% in the estimated stiffness was observed. This can be attributed to the tolerance between the sleeve bearing and the pull-out dowel used as a guide for the bearing. The surface contact can be reduced by employing ball bearings. The variation in the anatomical layout of wrists between subjects is considerable, and this introduces experimental challenges in identifying and aligning target positions repeatably. Additionally, constraining the high number of degrees of freedom of the arm is difficult and minor movements have been observed to cause significant variability in the estimated mechanical impedance. This study also investigated only 4 candidate sites around the wrist and future studies should investigate the effects of including a more detailed topological representation of the wrist. Extending this investigation into dynamic regimes may help us understand the role of soft tissue in the mechanical behavior of the wrist. It would also be interesting to examine paths to generate impedance matched surfaces with this data.

Chapter 5

CHARACTERIZATION OF DDDVIBROTACTILE SENSITIVITY THRESHOLD AT THE WRIST TO IMPROVE HAPTIC DEVICE PERFORMANCE

Gaurav Mukherjee[1], *Ali Israr*[2], *Elia Gatti*[3], *Majed Samad*[4], *Patrick Aubin*[1,5], *Eric Rombokas*[1,5], *Raymond King*[2]

1. Department of Mechanical Engineering, University of Washington, Seattle, WA 98195, USA

2. Facebook Reality Labs, Redmond, WA 98052,

3. Dr. Gatti was with Facebook Reality Labs, and is now with Amazon, London, W6 9LA, UK,

4. Dr. Samad was with Facebook Reality Labs, and is now with Google SEA - South Lake Union, Seattle, WA 98109,

5. Center for Limb Loss and Mobility (CLiMB), VA RR&D, Seattle, WA 98108, USA

Before reaching the mechanoreceptors, vibrotactile signals are filtered by the surrounding skin tissues. As the mechanical properties of such tissues vary with location and coupling pressure between the vibrotactile actuator and the tissues, the same external vibration will induce different somatosensory responses at different anatomical locations and coupling pressures. To compensate for this, it is necessary to first characterize the mechanical impedance and detection threshold for vibrotactile stimuli at different locations as well as to understand the effect of coupling pressure between the vibrotactile actuator and the tissue. We quantify the mechanical impedance and detection threshold at two biomechanically distinct locations about the wrist. We measure the mechanical impedance of the tissues on a log contrast scale in decibels of newton seconds per meter (Ns/m), and the detection threshold in terms of displacement, force and finally in a novel representation in terms of peak mechanical power. We demonstrate that bony regions are stiffer and more perceptually sensitive to vibrotactile stimuli than tendinous regions, and that increasing coupling pressures increases the mechanical impedance, while it decreases the detection threshold when described in displacement and position. We also find that upon describing the detection threshold in terms of the peak mechanical power, we no longer have to worry about the coupling pressure between the actuator and the tissue. This gives rise to the conjecture that the detection of a vibrotactile stimulus may be influenced predominantly by the mechanical power filtered through the tissues to the mechanoreceptors.

5.1 Introduction

Skin is a multi-layered viscoelastic organ which is embedded with afferent sensory organs called mechanoreceptors. Mechanoreceptors are specialized in detecting different types of stimuli that exceed a threshold of mechanical stimulus (Cholewiak et al., 1991). This threshold or limen of stimulus that activates the mechanoreceptors is of interest to engineers who design wearable robots, such as prostheses, exoskeletons, and haptic displays. While prior research has characterized the detection threshold for vibrotactile stimulus for glaborous and hairy tissues (Bolanowski, 1988), the anatomical locations selected for examination tend to be rich in soft tissues. The difference in the threshold between anatomical locations that are richer in bone and those where soft tissue is more prevalent is not clearly understood. Also, since wearable robots are physically coupled to entire cross-sections of anatomical regions with diverse mechanical properties, the effect of coupling pressures between actuators and the body on the detection threshold is of particular interest.

The wrist is one such important and common anatomical location where wearable robots are coupled to the body. The cross-section of the wrist is biomechanically diverse, and has regions such as the carpal tunnel which is rich in soft tissue structures such as tendons, vasculature and fascia. This region is enclosed by the carpal bones, and the radius and the ulna. When wearable robots are coupled to the wrist, they apply coupling pressures over skin and the underlying tissues, over both bony and tendinous regions. Therefore, to characterize the variation in mechanical properties and the vibrotactile sensitivity as a function of the tissue structures under the skin, this work quantifies the mechanical impedance and detection threshold under three coupling pressures applied at two regions about the wrist - over the tendinous area proximal to the carpal tunnel, and over the radius bone, along the long axis of the carpometacarpal bone. As the mechanical properties of the composite tissues vary with location, we hypothesize that the same external vibration will induce different somatosensory responses at the two anatomical locations with the bone rich, "radius" location being more sensitive than the soft tissue rich, "tendon" location.

The following sections describe the design of our experiment, followed by the quantification of the mechanical impedance in Ns/m units and detection threshold in units of position, force and finally mechanical power for vibrotactile stimuli chosen from a perceptually relevant frequency band spanning 10 to 320 Hz.

5.2 *Methods*

5.2.1 Apparatus

We use the Wrist Impedance Measurement Platform for this experiment (Fig. 1). The design and characterization of the device have been described in chapter 4.

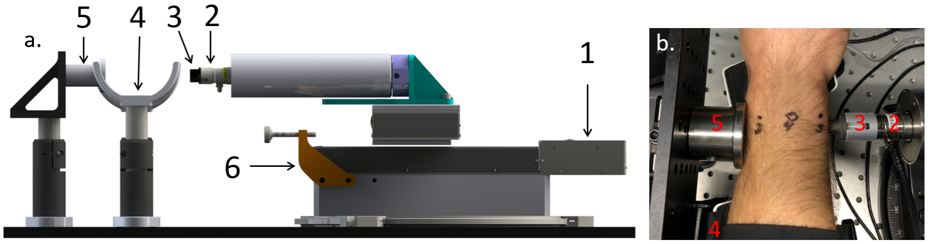

Figure 5.1: Schematic of the Wrist Impedance Measurement Platform showing the actuator and arm rest

5.2.2 Design of experiment

18 participants consented and took part in an experiment approved by the Washington Internal Review Board, aimed at characterizing the change in detection threshold as a function of wrist locations and coupling pressures. Data from 3 subjects were excluded for excessive arm movement and for poor compliance with instructions during the experiment. We characterized the biomechanical property of mechanical impedance, and the perceptual property of absolute detection threshold, simultaneously.

The mechanical impedance is the resistance of the structure to motion applied to it. It is quantified as the gain between the reaction force and the applied harmonic velocity at a given frequency. The absolute detection threshold is the lowest signal that can be reliably perceived by an individual. We quantified both our metrics using a 3 alternate forced choice (AFC) design with a maximum likelihood based estimation of the detection threshold from a staircase method called QUEST [31]. Our experiment utilized a C++ implementation of the QUEST paradigm based on the Matlab PsychToolbox [32, 31, 33]. Each QUEST comprised of a staircase of stimuli. The intensity of the stimuli increased if the participant failed to identify the correct window, and the stimulus intensity decreased if the window was identified correctly. The QUEST was considered converged when a constraint of 30 trials and 6 reversals was achieved.

The factors, location and coupling pressure had 2 and 3 levels, respectively. We measured the mechanical impedance and detection threshold at 1N, 3N, and 5N of force, which translated to 5.7 kPa, 17 kPa, and 28.3 kPa over a contactor with diameter 15 mm, respectively. Location had the levels, tendon and radius. Tendon refers to the soft tissue rich location on the wrist proximal to the carpal tunnel, and radius refers to the bone rich location along the radial bone, just proximal to the radial styloid process. We quantified mechanical impedance and detection threshold values at 5 frequencies spaced logarithmically between 10 Hz and 320 Hz. Using a block based design, we measured the detection threshold and mechanical impedance for each location as an independent block, randomized between subjects. Within each block, each QUEST was quantified for a randomized combination of frequency and coupling pressure, for a total of 15 QUESTS per location. For every trial, the contactor between the load cell and the wrist was made of Delrin (Shore hardness, D-83). Since every participant experienced all conditions, this is a within subjects design.

5.2.3 Experiment - Measurement of mechanical impedance and detection threshold

The participants were introduced to the experiment, the apparatus and the safety protocol for the experiment. After obtaining consent, measurements of the location of the indentation points on the wrist were made. To account for the variability in the size and shape of wrists across participants, we mapped the locations of the four indentation locations to a linear graduated scale.

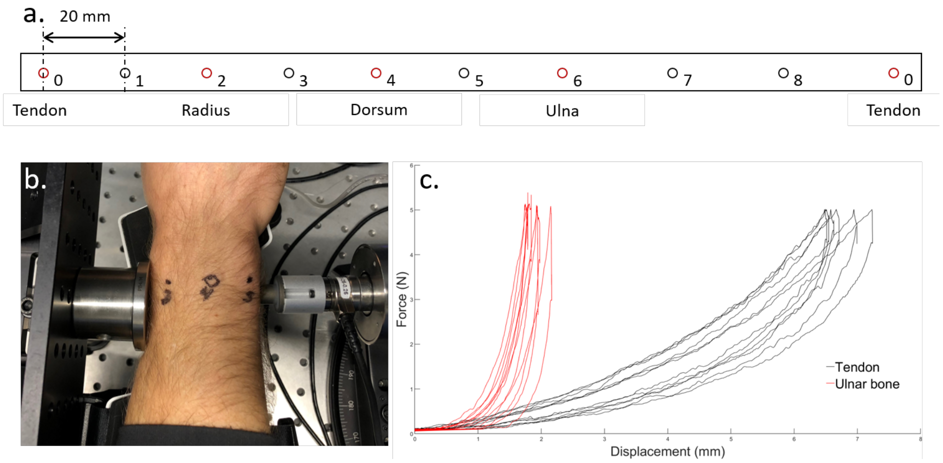

Figure 5.2: a. Calibration of the wrist to a measuring tape to map variability in locating anatomical features on the wrist across participants, b. Trial in progress, c. Coupling force applied at the tendon and the ulnar bone.

Participants were seated at a table and a metric paper tape measure (width, 22 mm), punched with holes of 4 mm diameter placed 10 mm apart, (Fig. 5.2. a.) was attached to the wrist on the right arm such that the center of the holes were 11 mm proximal to the prominence of the ulnar styloid process on the wrist. The first location, indexed at 0, was aligned to lie on the volar aspect of the wrist along the long axis of the forearm, between the elbow and the third digit of the outstretched hand over the flexor tendons. The holes in the paper tape closest to three other anatomical landmarks, namely the radial styloid process, the dorsum and the ulnar styloid process, were used to mark the wrist for indentation (Fig. 5.2. b.).

Following the calibration procedure, participants were seated on a height adjustable lab stool with their right forearm placed in the arm rest (Fig. 4.1). The participant's arm was rotated to ensure flat contact of the target position on the wrist with the indenter (Fig. 5.3, Fig. 5.4).

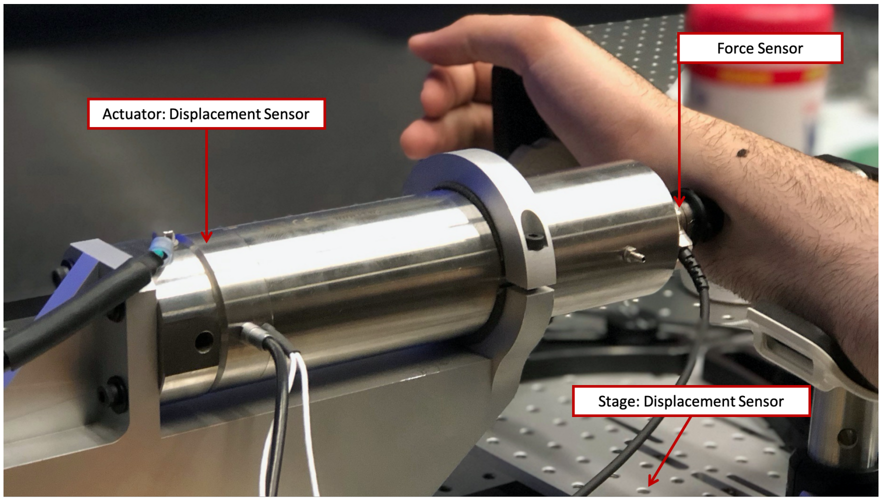

Figure 5.3: Trial in progress: Stack actuator is shown with a displacement sensor at the left end of the actuator. The force sensor is connected to the actuator head, and to the Delrin flat contactor. The contactor is applying a coupling pressure of 28.3 kPa over the tendinous region of the wrist. The stage displacement sensor is used to measure the displacement of the arm rest to apply the coupling pressure to the wrist.

The participants were then given detailed instructions about the experiment, and were asked to drive the indentation stage to experience the loading levels to be expected during the trial. Participants also familiarized themselves with the use of the emergency stop button and the pause functionality. The mechanical stop was adjusted to prevent the movement of the translation stage towards the arm once the highest target force had been achieved.

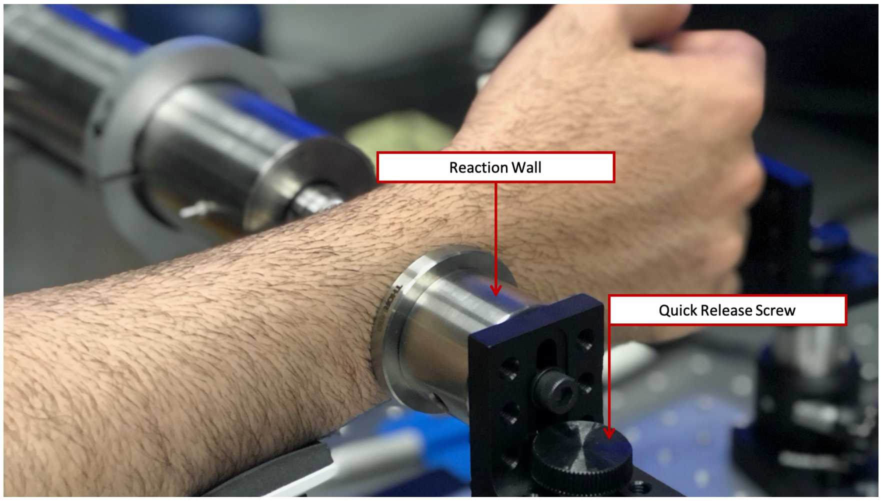

Figure 5.4: The dorsal aspect of the arm is supported by a reaction wall. This wall is held in place with a quick release screw that allows the participant to recover their arm from the test set-up in the eventuality of an emergency.

The stimulus applied to the wrist is a displacement corresponding to a windowed pure tone sine wave at a frequency and peak to peak amplitude, with a rising segment of 0.1 second duration, a steady section of 1 second duration, and a fall of 0.1 second duration 5.5. The stimulus is generated at the piezoelectric stack actuator in response to a reference control waveform generated by a NI 9125 data acquisition system with an on-board function generator.

When the sine wave stimulus is applied as a displacement to the tissue, the response is measured as a reaction force. The phase lag of the reaction force with respect to the displacement demonstrates the expected causal relationship. Additionally, we see a slow oscillatory wave modulated with the reaction force. We believe that this is due to the residual unconstrained movement of the arm in the arm rest 5.6.

During the experiment, subjects wore noise cancelling headphones that played pink noise to remove the effect of ambient noise. Further, subjects were instructed to focus on the

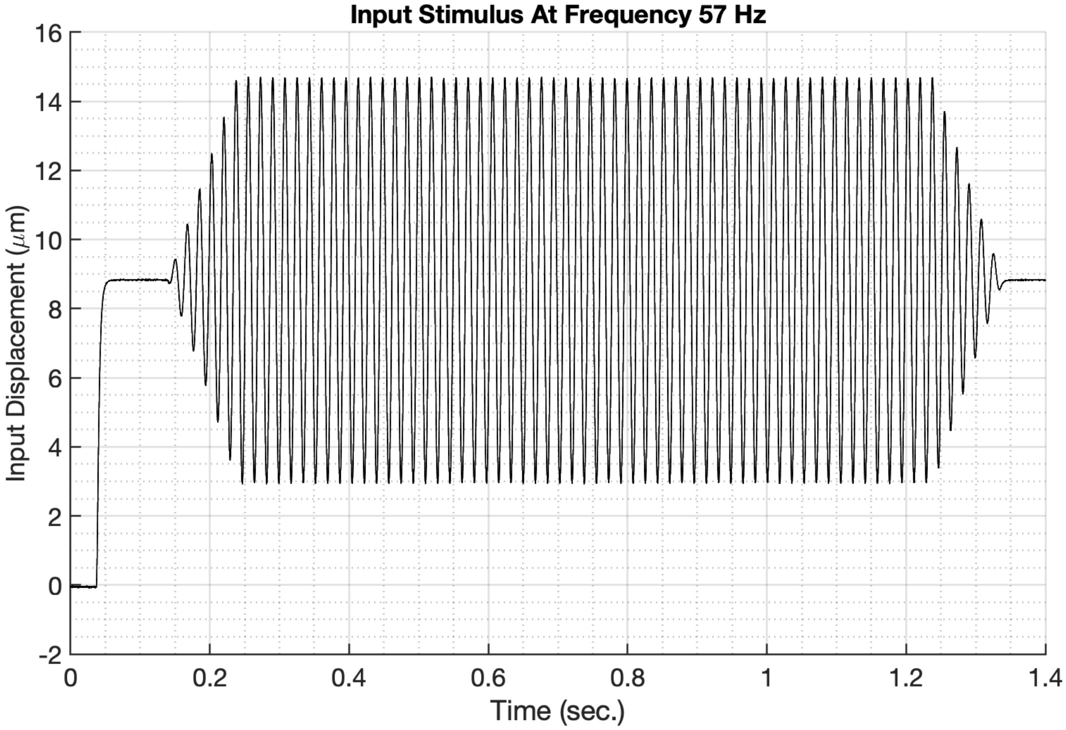

Figure 5.5: Windowed pure tone sinusoidal stimulus at 57 Hz.

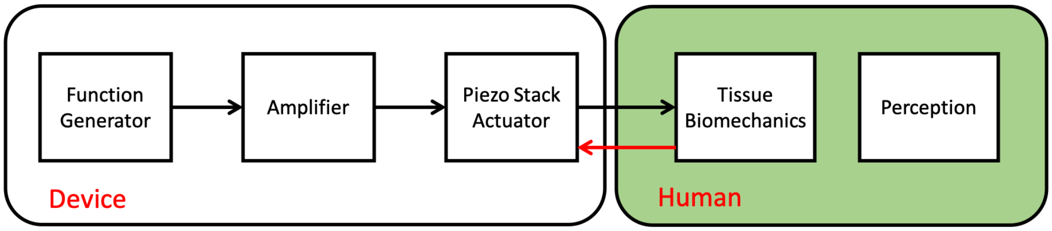

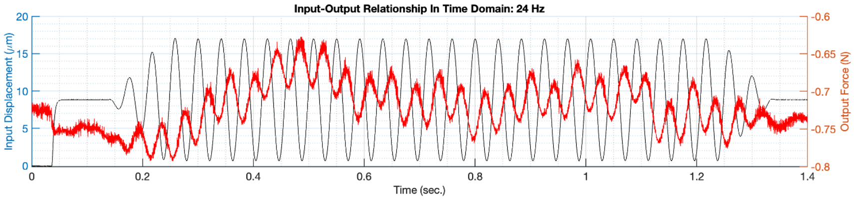

Figure 5.6: Input windowed pure tone sinusoidal displacement stimulus at 24 Hz and output force response.

screen placed in front of them where a visual feedback was provided to indicate the force fluctuation at the contact point. This was done to allow the subject to self regulate the microscopic movements of their arm while being seated for the duration of the experiment. This visual indicator was removed during the actual trial so as to not bias the subject's tactile estimation of the presence of the stimulus with a visual indicator.

For each location, three coupling pressures and five frequencies were tested. For each combination of coupling pressure and frequency. participants completed a QUEST, which were a series of trials with decreasing or increasing intensity levels of the stimulus, intended to estimate the detection threshold. The quest was considered converged at 30 trials, unless the total number of reversals, the occurrence of either an incorrect trial following a correct trial, or vice versa, was less than 6. If the number of reversals was less than 6, the quest continued until this criteria was met.

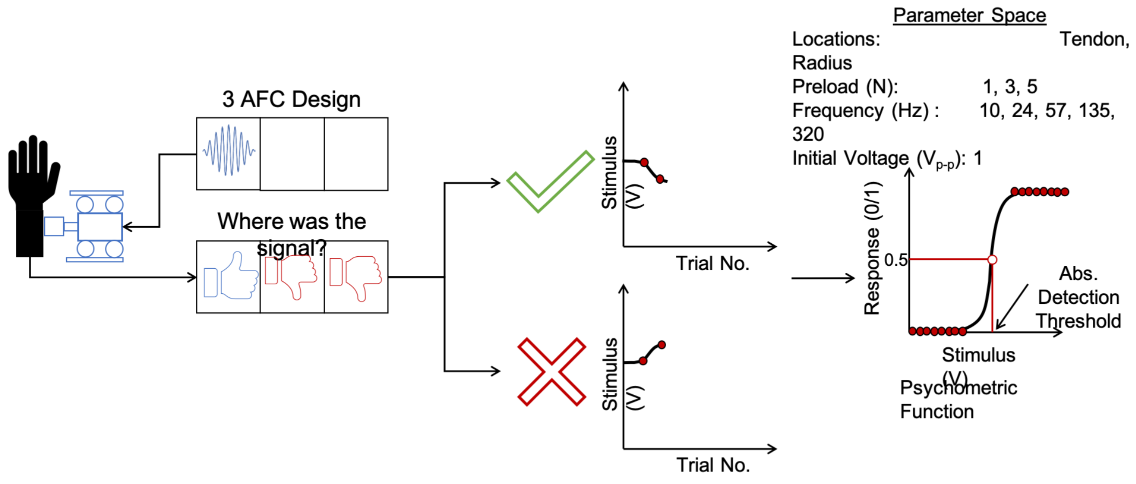

Figure 5.7: 3 AFC based estimation of absolute detection threshold

In each trial there were 3 phases - the first phase of each trial, the stage on which the arm rests, moved towards the static actuator at 5 mm per second. Once the actuator made contact with the wrist, the actuator proceeded to indent the site at 2mm per sec., until the prescribed coupling pressure of 17 kPa, or 3N of force has been reached. At this point the indentation stage stopped moving and the visual force feedback indicator disappeared from the screen. In the second phase of the trial, 3 windows were provided to the subject, delineated by auditory beeps played over the headphones. One of the windows contained the stimulus applied to the wrist. The subject's task was to identify which of the three auditory windows also contained the stimulus. The location of the stimulus was randomized in each trial. When the subject correctly identified the stimulus window, the subsequent trial would have an identical stimulus at a lower peak to peak displacement amplitude. If the subject failed to identify the correct window, the subsequent trial would have a stimulus with a higher amplitude of displacement. The displacement amplitude of the stimulus for each trial was estimated using the QUEST methodology. In the third and last phase of each trial, the indentation stage would drive the arm back at 2 mm per sec. until loss of contact between the robot and the arm. This marked the end of the trial.

The QUEST toolbox estimated the detection threshold by fitting a psychometric function to the array of the correct or incorrect responses for each trial and the amplitude of the stimulus. This detection threshold in voltage units is then multiplied by a gain value for the specific frequency to estimate the detection threshold in displacement units. The displacement data and the force data are then used to compute the mechanical impedance for each frequency and coupling pressure.

5.3 Results

5.3.1 Mechanical Impedance Measurements

The mechanical impedance was measured in decibels for each frequency and coupling pressure. We find that as the frequency increases from 10 Hz to 320 Hz, the mechanical impedance decreases over the radius location. This trend is true for all 3 coupling pressures. For the tendon, at the lowest coupling pressure of 5.7 kPa, the mechanical impedance decreases until 135 Hz, and then begins to rise again. This inflection point is pushed to a higher frequency beyond the measured band when the coupling pressure is increased. The mechanical impedance over the tendon also increases with increasing coupling pressures. The mechanical impedance of the tendon location is lower than that for the radius location for the same coupling pressure.

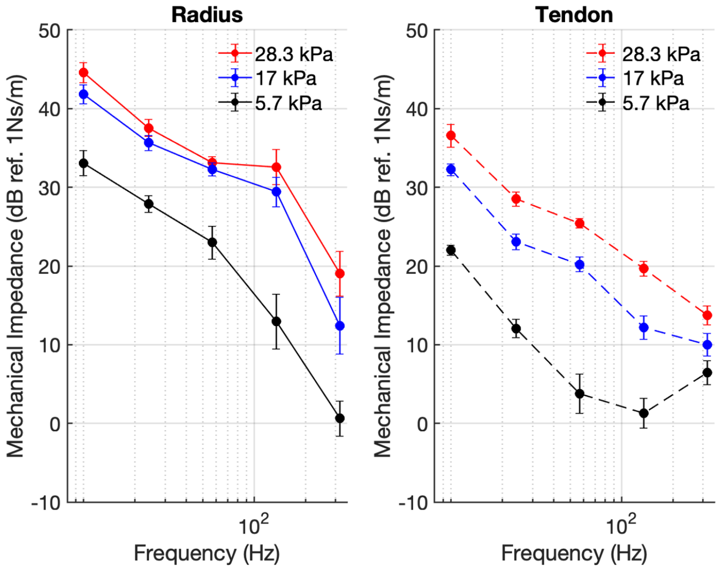

Figure 5.8: Mechanical Impedance over radius and tendon

5.3.2 *Detection Threshold Measurements*

Position Detection Threshold

The position detection threshold represents the smallest displacement that the participants can perceive reliably. It is measured in terms of peak-peak displacements and is reported in meters. The position detection threshold changes with frequency, and coupling pressure for a given location. Also, the position detection threshold is higher over the tendon as compared to the radius location, for the same coupling pressure. As the coupling pressure increases, the displacement detection threshold decreases.

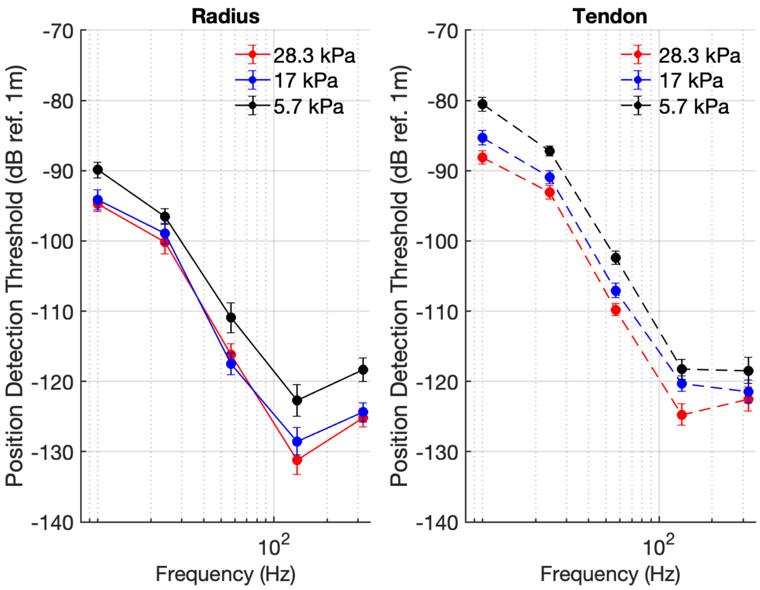

Figure 5.9: Position Detection Threshold over radius and tendon

Force Detection Threshold

The force detection threshold, derived from the concurrent force measurements made during each trial represents the smallest stimulus force that the participants can perceive reliably.

It is measured in terms of peak-peak force values and is reported in Newtons. The force detection threshold changes with frequency, and coupling pressure for a given location. The force detection threshold is higher over the radius as compared to the tendon location, for the same coupling pressure. Intuitively, but interestingly, as the coupling pressure increases, the force detection threshold increases.

Power Detection Threshold

Since the detection threshold demonstrated variations in both force and position units, we describe the detection threshold in terms of a function that captures the effects of both force and displacement, mechanical power. The power detection threshold, derived from the

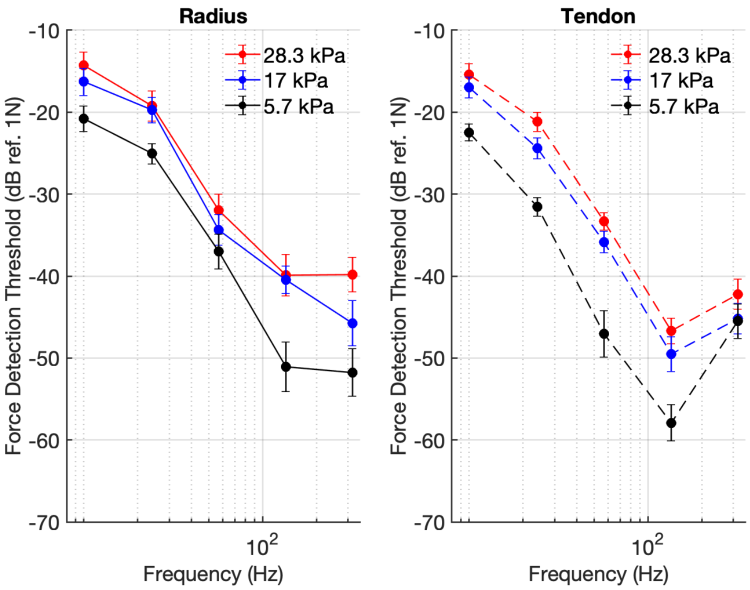

Figure 5.10: Force Detection Threshold over radius and tendon

force and displacement measurements made during each trial, represents the lowest peak mechanical power transmitted to the tissue that makes the stimulus reliably detectable. The power detection threshold changes with frequency, and location. However, the power detection threshold does not vary with coupling pressure. The power detection threshold is higher over the tendon as compared to the radius.

5.4 Discussion

We measured the input-output relationship between the displacement and force signals when a vibration is applied to the wrist over bony and soft regions. We find that the mechanical impedance is higher over the bone than it is over the tendinous region. By increasing the coupling pressure over both regions, we increase the tissue mechanical impedance. Interestingly, as we increase the coupling pressure over the tendons, we find that the tissue changes behaviour in our frequency band, from a second order viscoelastic system to a primarily elastic system. Anecdotally, all the participants reported feeling more comfortable when the

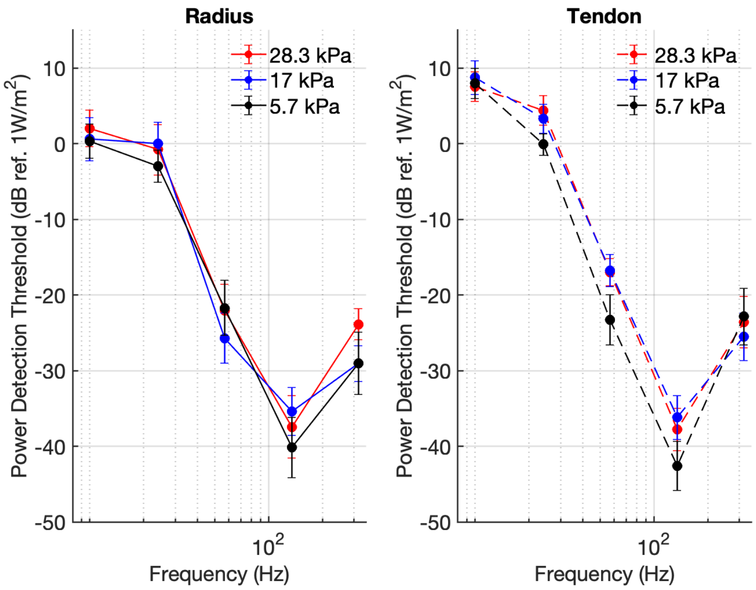

Figure 5.11: Power Detection Threshold over radius and tendon

pressure was applied over the bony region, which may be due to the vasculature, tendon structures, and nerves that pass through the carpal tunnel.

We measured the vibrotactile detection threshold using a 3 AFC bayesian method called QUEST. The detection thresholds were reported in the standard position units of meters, force units of Newtons and in a novel extension, in terms of the normalized peak mechanical power unit of $Watts/meter^2$.

The position detection threshold varies with frequency for a given location. When compared to prior literature, there is good agreement with Bolanowski's reported detection threshold values. However, Bolanowski reported detection threshold results estimated from the thenar eminence. There is no prior literature on detection thresholds from the wrist. It appears that the thenar eminence is more sensitive than the wrist, particularly when compared to the region over the tendons. However, the trend demonstrate by Bolanowski's data for this range is similar to the wrist data from our experiments. No comparisons were found for the effect of coupling pressure.

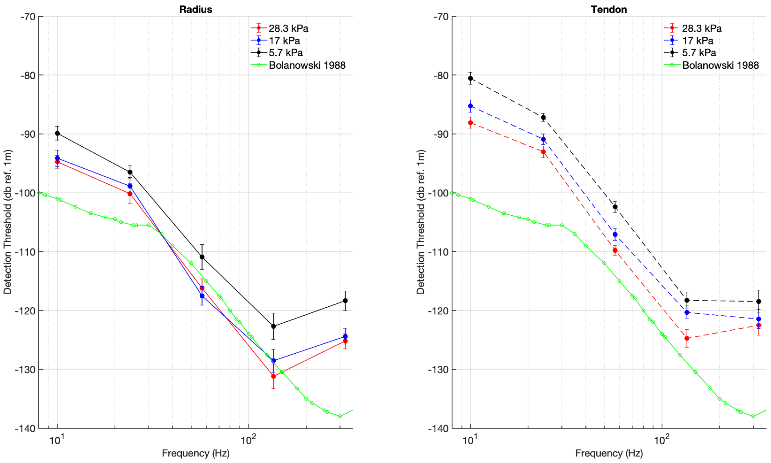

Figure 5.12: Position Detection Threshold over radius and tendon. Comparison with Bolanowski 1988

The force detection threshold was measured in Newtons and has never been reported for the wrist. Interestingly, the force detection threshold demonstrates an increase in force required for stimulus to be detectable, when coupling pressure is increased. This result seems intuitive since as coupling pressure increases, the mechanical impedance of the tissue increases, making the required force to deform tissue to a detectable limit higher.

The power detection threshold has not been reported before, to our best knowledge. We report this in $Watts/m^2$, normalizing the power for the contactor area. This data accounts for coupling pressure and demonstrates that as long as the peak mechanical power transmitted to the tissue remains at or above the threshold, irrespective of the coupling pressure, the stimulus would be detectable.

5.5 Conclusion

The detection threshold is a key metric of perception reported for different anatomical locations (Bolanowski, 1988; Cholewiak et al., 1991; Cholewiak et al., 2003). However, this metric had never been quantified for the wrist. The wrist is both interesting and challenging to study since the mechanical impedance of the tissue is diverse and the bony regions require actuators with higher mechanical impedance to deliver unchanged actuation. In this experiment, we observe that the position detection threshold over tendon is higher than that over the radius. Further, the increasing coupling pressure led to higher sensitivity to the stimulus. Finally, the novel power detection threshold demonstrates that the coupling pressure ceases to matter as long as the mechanical power delivery can be assured. The higher detection threshold over the bony region could be due to a higher density of mechanoreceptors at that location. However, we observe that the detection threshold decreases with increasing coupling pressure. Since detection threshold is mediated by the power per unit area transferred to the tissue and onward to the mechanoreceptors, we conjecture that if we change the power transmitted to the tissue, then the detection threshold will change as well.

Chapter 6

TUNING THE SENSITIVITY TO A VIBROTACTILE STIMULUS THROUGH THE MECHANICAL IMPEDANCE OF THE HUMAN DEVICE INTERFACE

Gaurav Mukherjee[1], *Ali Israr*[2], *Majed Samad*[3], *Patrick Aubin*[1,4], *Eric Rombokas*[1,4], *Raymond King*[2]

1. Department of Mechanical Engineering, University of Washington, Seattle, WA 98195, USA
2. Facebook Reality Labs, Redmond, WA 98052,
3. Dr. Samad was with the Facebook Reality Labs, and is now with Google SEA - South Lake Union, Seattle, WA 98109,
4. Center for Limb Loss and Mobility (CLiMB), VA RR&D, Seattle, WA 98108, USA

6.1 Abstract

Somatosensory mechanoreceptors in the skin on the human wrist are activated at a fixed threshold of deformation (Biswas et. al. 2015). This implies that the perceptual sensitivity to tactile stimuli on the wrist depends on the mechanical power that is transmitted to the mechanoreceptors. To test this theory, we first measured the detection threshold to a vibrotactile stimulus applied by a piezo stack actuator in direct contact with wrist tissue, and then in the presence of materials of different mechanical impedance at the human device interface (HDI). We demonstrate that as the mechanical impedance of the HDI material decreases, vibrotactile stimuli with higher input peak mechanical power are required for the stimulus to reach detection threshold, since the HDI material absorbs a significant proportion of the input power. This implies that the transmission of a vibrotactile stimulus to the mechanoreceptors can be tuned by changing mechanical impedance alone, assuming equal density of mechanoreceptors all around the wrist.

6.2 Introduction

In literature, and industry a common issue that plagues haptic device design is the variability of perceived intensity of stimulus across anatomical locations for identical stimuli (Cholewiak et al., 2003). One such anatomical location commonly used to couple haptic displays is the wrist. The wrist is biomechanically diverse, with soft tissue rich tendinous regions encapsulated by bone rich locations. Our prior research has characterized both mechanical and perceptual properties at these diverse locations about the wrist cross-section and we found that, across locations, mechanical impedance and vibrotactile detection thresholds change with frequency, location, and coupling pressures. We also discovered that the detection of a stimulus could be described in terms of mechanical power, which accounted for the variations in coupling pressure. This finding supported prior literature (Biswas 2015) to suggest that perceievability of a stimulus is dependent on the mechanical power that is transmitted to the mechanoreceptors through the tissues. our goal is to examine if changing the proportion of total input mechanical power from the actuator that is transmitted to the tissues changes the perceivability of a stimulus. We achieve this goal by quantifying the absolute detection threshold with materials of different mechanical impedance attached at the human device interface (HDI) (Fig. 6.1). We hypothesize that as we decrease the mechanical impedance of the system (tissue + HDI), we will see an increase in detection threshold across the HDI and Tissue system. If this hypothesis is true, then for the first time we will have demonstrated a way in which perceptual sensitivity to a vibrotactile signal may be modulated by the design of the HDI.

6.3 Methods

6.3.1 Apparatus

We use the Wrist Impedance Measurement Platform for this experiment (Fig. 1). The design and characterization of the device have been described in chapter 4.

We modify the device by customizing the hardness of the contact surface by adding cylin-

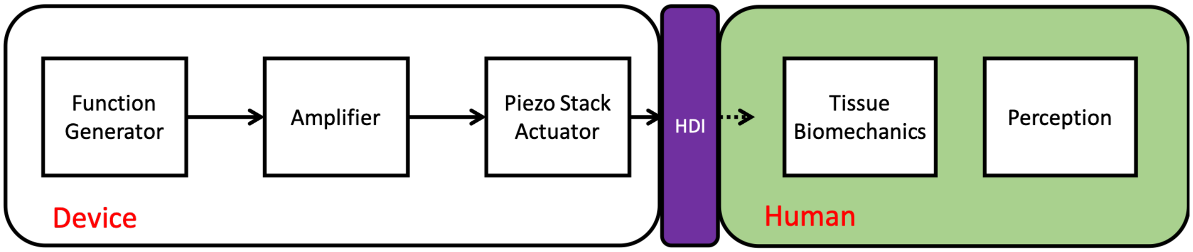

Figure 6.1: We change the transmitted power to the tissue by introducing a material of reduced stiffness in series between the actuator and the tissue

drical plugs (15mm diameter, 2 cm height) made from materials with hardness spanning shore scales in series between the actuator and the tissue locations on the wrist. In the first condition with no material, the Delrin contactor (shore hardness, D-83) makes direct contact with the tissues over the wrist locations. In the second condition, a material plug of intermediate hardness (shore hardness, A-30) is attached to the end of the Delrin contactor, and in the last condition, a material plug with soft hardness (shore hardness, OO-30) is attached to the contactor (Fig.2).

6.3.2 *Analytical model of transmission of mechanical power across the human device interface*

The material plugs are connected to the tissue in series, which means that under equilibrium, when the coupling pressure is applied to the contactor and the wrist tissue, the force at the loadcell-contactor, contactor-material, and the material-tissue interfaces are all equal. However, the total displacement applied by the actuator is distributed between the material and the tissue. Series impedances sum as shown in equation 1.

$$z_{HDI} = \frac{z_{material} * z_{tissue}}{z_{material} + z_{tissue}} \tag{1}$$

6.3.3 Design of experiment

9 participants consented and completed an experiment approved by the Washington Internal Review Board, aimed at characterizing the change in detection threshold as a function of change in the mechanical impedance of materials at the human device interface. We characterized the absolute detection threshold, or the lowest signal that can be reliably perceived by an individual. We used a 3 alternate forced choice (AFC) design with a maximum likelihood based estimation of the detection threshold using a staircase method called QUEST (cite Pelli 1994). In addition to the constraint of 30 trials, we added an additional constraint of 6 reversals required for convergence to occur.

The factors, location and material had 2 and 3 levels, respectively. Frequency was fixed at 57 Hz. This value was shown to be predominantly spring like in its behavior in Chapter 4, thus making it a good candidate for this experiment. The preload was fixed at 3N. Location had the levels, tendon and radius. Tendon refers to the soft tissue rich location on the wrist proximal to the carpal tunnel, and radius refers to the bone rich location along the radial bone, just proximal to the radial styloid process. Material has 3 levels, NoMat, A30 and OO30. NoMat refers to the direct contact between the Delrin contactor and tissues, which is also the hardest material condition with shore hardness, D-83. A30, is a rubber polymer with intermediate shore hardness, A30, and OO-30 refers to Ecoflex material which is soft with a shore hardness of OO-30. In the results, the NoMat condition is referred to as Hard, the A-30 material condition is referred to as Intermediate, and the OO-30 material condition is referred to as Soft. Since every participant experienced all conditions, this is a within subjects design. The experiment consists of 2 blocks corresponding to the locations, which were sequenced alternately for each subject. Within each block, the three material conditions were interchanged according to an incomplete lattice.

6.3.4 Measurement of mechanical impedance and detection threshold

The participants were introduced to the experiment, the apparatus and the safety protocol for the experiment. After obtaining consent, measurements of the location of the indentation points on the wrist were made. To account for the variability in the size and shape of wrists across participants, we mapped the locations of the four indentation locations to a linear graduated scale. Participants were seated at a table and a metric paper tape measure (width, 22 mm), punched with holes of 4 mm diameter placed 10 mm apart, (Fig. 5.2. a.) was attached to the wrist on the right arm such that the center of the holes were 11 mm proximal to the prominence of the ulnar styloid process on the wrist. The first location, indexed at 0, was aligned to lie on the volar aspect of the wrist along the long axis of the forearm, between the elbow and the third digit of the outstretched hand over the flexor tendons. The holes in the paper tape closest to three other anatomical landmarks, namely the radial styloid process, the dorsum and the ulnar styloid process, were used to mark the wrist for indentation (Fig. 5.2. b.).

Following the calibration procedure, participants were seated on a height adjustable lab stool with their right forearm placed in the arm rest (Fig. 4.1). The participant's arm was rotated to ensure flat contact of the target position on the wrist with the indenter (Fig. 5.2. b.). The participants were then given detailed instructions about the experiment, and were asked to drive the indentation stage to experience the loading levels to be expected during the trial. Participants also familiarized themselves with the use of the emergency stop button and the pause functionality. The mechanical stop was adjusted to prevent the movement of the translation stage towards the arm once the highest target force had been achieved.

The stimulus applied to the wrist is a displacement corresponding to a windowed pure tone sine wave at a frequency and peak to peak amplitude, with a rising segment of 0.1 second duration, a steady section of 1 second duration, and a fall of 0.1 second duration. The stimulus is generated at the piezo stack actuator in response to a reference control waveform generated by a NI 9125 data acquisition system with an onboard function generator.

During the experiment, subjects wore noise cancelling headphones that played pink noise to remove the effect of ambient noise. Further, subjects were instructed to focus on the screen placed in front of them where a visual feedback was provided to indicate the force fluctuation at the contact point. This was done to allow the subject to self regulate the microscopic movements of their arm while being seated for the duration of the experiment. This visual indicator was removed during the actual trial so as to not bias the subject's tactile estimation of the presence of the stimulus with a visual indicator.

For each location, there were three material conditions at the HDI to be tested. For each material condition, participants experienced a quest, which were a series of trials with decreasing or increasing intensity levels of the stimulus, intended to estimate the detection threshold. The quest was considered converged at 30 trials, unless the total number of reversals, the occurrence of either an incorrect trial following a correct trial, or vice versa, was less than 6. If the number of reversals was less than 6, the quest continued until this criteria was met.

In each trial there were 3 phases - the first phase of each trial, the stage on which the arm rests, moved towards the static actuator at 5 mm per second. Once the actuator made contact with the wrist, the actuator proceeded to indent the site at 2mm per sec., until the prescribed coupling pressure of 17 kPa, or 3N of force has been reached. At this point the indentation stage stopped moving and the visual force feedback indicator disappeared from the screen. In the second phase of the trial, 3 windows were provided to the subject, delineated by auditory beeps played over the headphones. One of the windows contained the stimulus applied to the wrist. The subject's task was to identify which of the three auditory windows also contained the stimulus. The location of the stimulus was randomized in each trial. When the subject correctly identified the stimulus window, the subsequent trial would have an identical stimulus at a lower peak to peak displacement amplitude. If the subject failed to identify the correct window, the subsequent trial would have a stimulus with a higher amplitude of displacement. The displacement amplitude of the stimulus for each trial was estimated using the QUEST methodology. In the third and last phase of each trial, the indentation stage would drive the arm back at 2 mm per sec. until loss of contact between the robot and the arm. This marked the end of the trial.

The QUEST toolbox estimates the detection threshold by fitting a psychometric function to the array of the correct or incorrect responses for each trial and the amplitude of the stimulus. This detection threshold in voltage units is then multiplied by a gain value for the specific frequency to estimate the detection threshold in displacement units.

Mechanical impedance is the gain between the output force and input displacement at a given frequency. In this experiment, the mechanical impedance we measure is that for the combined material and tissue, or the system mechanical impedance. We obtain the system mechanical impedance by subtracting the mechanical impedance at the driving point due to the weight of the contactor attached to the load cell from the total system mechanical impedance measured from the experimental data. We measure the mechanical impedance for each trial from the dataset generated while estimating the detection threshold.

6.3.5 Measurement of subjective comfort and ease of perception of stimulus under different material conditions

At the end of each location block, participants were asked to rank the contactor material conditions according to relative comfort and relative ease of perceiving the stimulus with one being the least comfortable and easiest to perceive and 3 being the least comfortable and hardest to perceive.

6.4 Results

6.4.1 Estimation of the absolute detection threshold for vibrotactile stimuli in power units

The absolute detection threshold in power units was plotted against the normative data for the 3N or 17 kPa condition from the data set characterized in Chapter 5. We find that the Hard condition which corresponds to no material being attached to the contactor, lies within the range for the normative data. As we add materials of increasing softness, the system's power detection threshold for both radius and tendon increases (Fig 6.1). The increase in the system power detection threshold is greater over the bone than over the tendon however. Over the tendon, the softest material does not cause an increase in the power detection threshold.

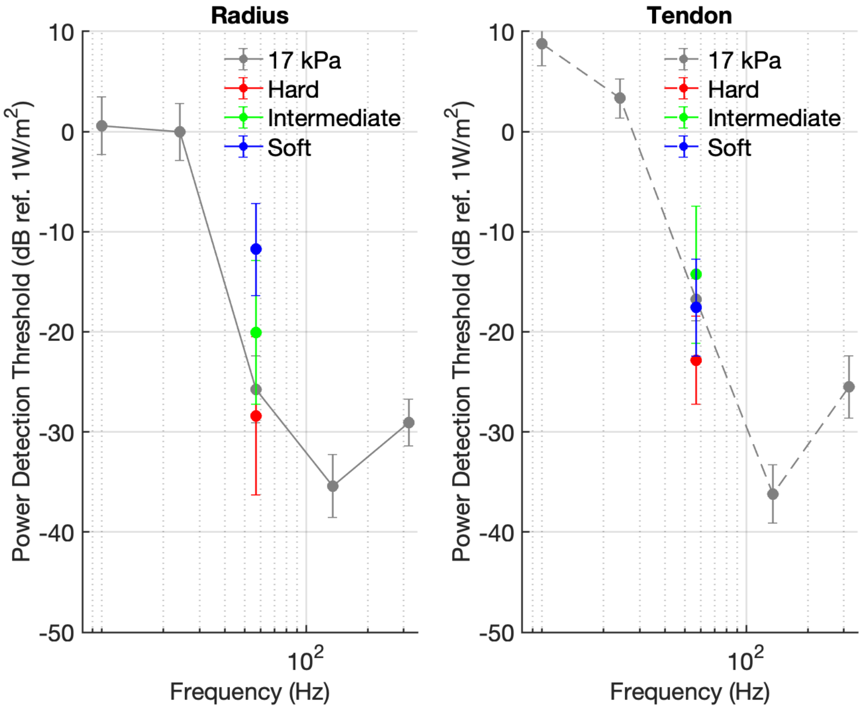

Figure 6.2: Changing the HDI material affects the power detection threshold for both the bony and tendinous regions

When we plot the detection threshold vs the material condition, the data demonstrates a general trend towards increasing detection threshold with decreasing hardness of the HDI material.

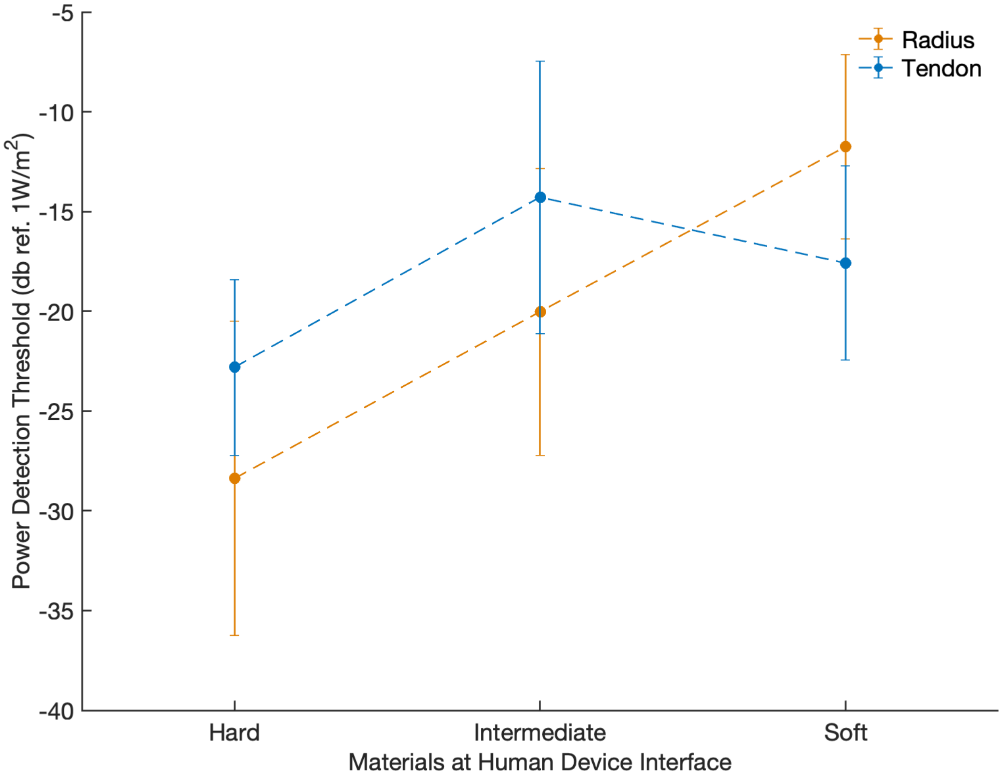

Figure 6.3: The power detection threshold increases as the softness of the material increases

6.4.2 Measurement of mechanical impedance of the tissue and HDI material system

The mechanical impedance was plotted against the normative data for the 3N or 17 kPa coupling pressure condition from the data set characterized in Chapter 4. We find that the Hard condition which corresponds to no material being attached to the contactor, lies within the range for the normative data. As we add materials of increasing softness, the total mechanical impedance for both radius and tendon reduces (Fig 6.1). The reduction of the system impedance is greater over the bone than over the tendon.

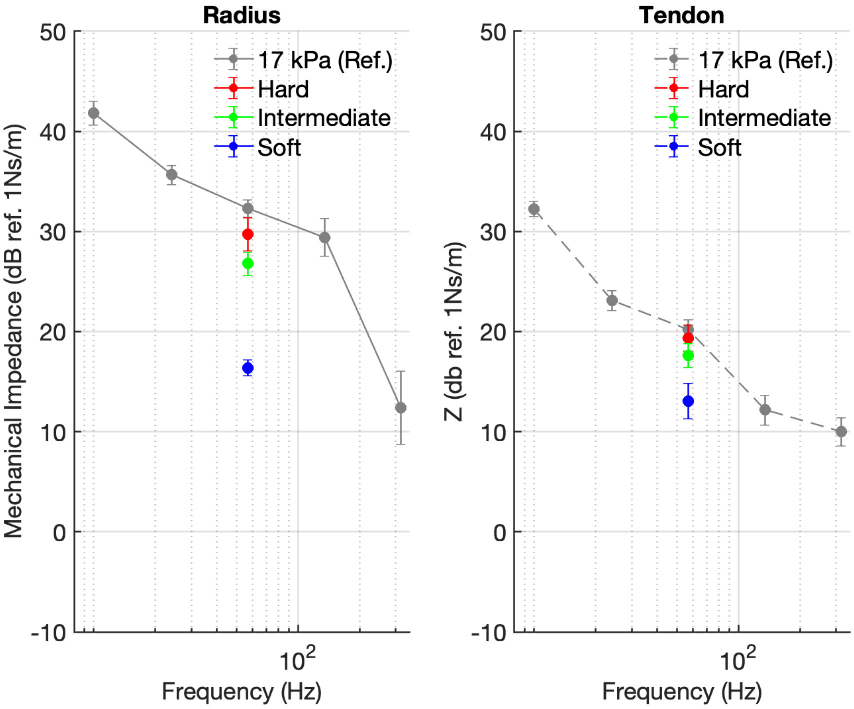

Figure 6.4: Effect of changing the system mechanical impedance is observed for both the bony and tendinous regions.

6.4.3 The change in system impedance is correlated with change in the system detection threshold

When we plot the absolute detection threshold versus the mechanical impedance, we find an inverse correlation between the two metrics for both locations.

6.4.4 Subjective comfort and ease of perception of stimulus under different material conditions

Participants ranked the materials on the basis of relative comfort and on the ease of perceiving stimulus. On average, participants found the softer materials to be more comfortable. However, the softer the material, the harder it was for participants to perceive the

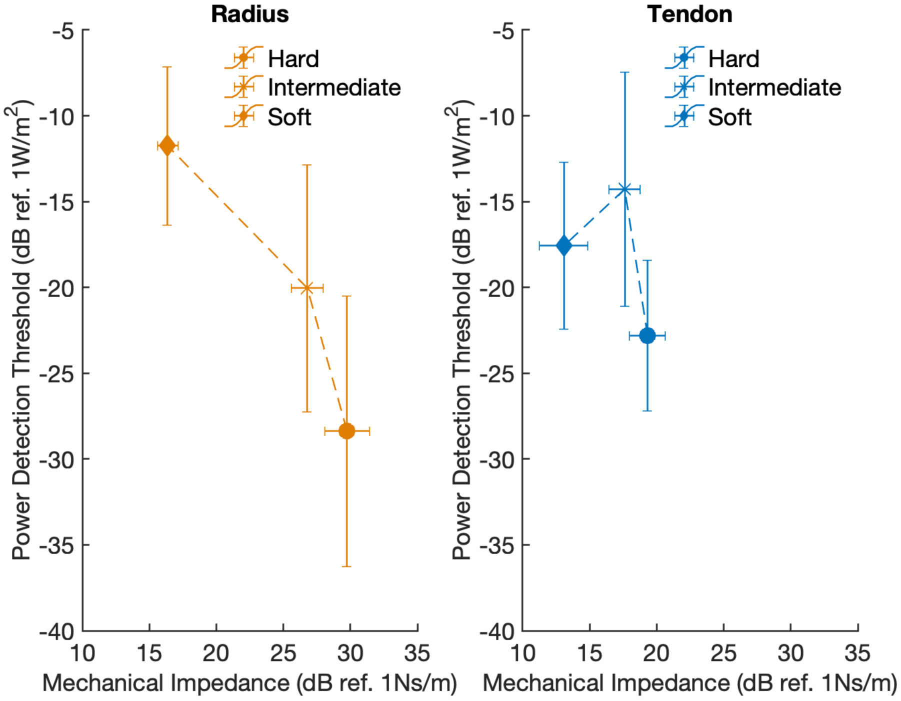

Figure 6.5: Measured stiffness of the hand dorsum for five equally spaced points along the second metacarpal at three levels of grasp force applied by the subject.

signal. This behavior correlated positively with the trends observed for the system mechanical impedance and the detection threshold, respectively.

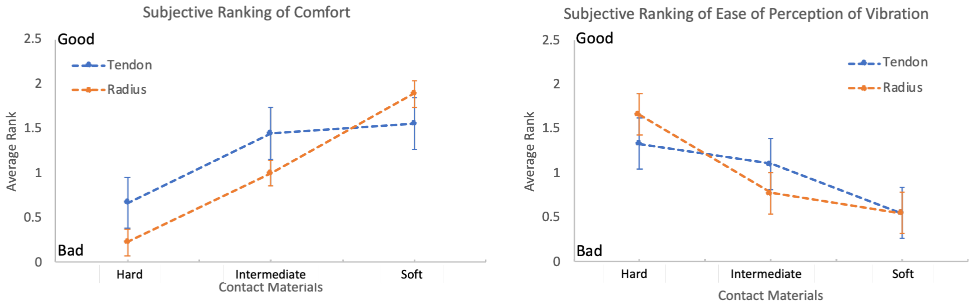

Figure 6.6: Results from relative ranking of contactor material conditions on the basis of comfort and ease of perceivability of stimulus

6.5 Discussion

6.5.1 Estimation of the absolute detection threshold for vibrotactile stimuli and mechanical impedance

The absolute detection threshold or the power required for the stimulus to be perceivable increases with increasing softness of the material. This increase is monotonic over the bone and the largest change with respect to the baseline (Hard condition) is observed for the softest material over the radius. This trend is not observed for the tendon, however. Here the softest material requires more power than the baseline condition, but not as much as the intermediate condition. The reason for this behavior is likely due to the series coupling of the tissue and the material. In series coupling of mechanical impedances, the softest material dominates the overall mechanical response of the system. Also, this observation tells us that the boundary condition matters - bony locations behave differently than soft tissue rich tendinous locations, where the overall effect of attaching materials on the detection threshold and mechanical impedance was low.

6.5.2 The change in system impedance is correlated with change in the system detection threshold

Estimation of detection thresholds is prone to uncertainty. However, there is a trend for increasing power requirement for the stimulus to be perceivable as the material impedance decreases.

6.5.3 Subjective comfort and ease of perception of stimulus under different material conditions

Interestingly, increase in comfort correlates positively with difficulty in perceiving the stimulus. This implies that the perceptual performance and comfort under coupling are inversely related. This inverse relationship is also reflected in the relationship between mechanical impedance and the detection threshold of the system, suggesting that comfort and performance of the coupled vibrotactile device can be modulated by changing the mechanical impedance of the system.

6.6 Conclusions

In this study, we examined the role of power transmission to the tissue in changing the vibrotactile sensitivity to a vibrotactile system. We do this by subjectively querying the relative ease of perception of the stimulus as we change materials between the actuator and the tissue, as well as quantitatively measuring the detection threshold and mechanical impedance of the system.

We find that as the mechanical impedance of the system reduces, the detection threshold increases for both bony and tendinous locations, implying that the ease of perceiving the stimulus decreases. We also find that as the mechanical impedance of the system decreases, the subjective report of comfort increases. Therefore, by changing the mechanical impedance of the material between the actuator and the tissue, we can change both the perception of the stimulus as well as comfort.

Chapter 7

CONCLUSIONS

This dissertation demonstrates that the development of the next generation of human device interfaces is possible only through gaining a clear understanding of properties of the human body.

In the first experiment, we quantify the torque required to extend the index finger about the MCP joint. We discover that a difference in the torque required, previously attributed to sex, is actually due to a difference between hand sizes. This finding allowed us to generate a single normative torque band which can be used by wearable designers as a quantitative reference for designing hand exoskeletons, and by clinicians to quantify hand function impairments.

In the second experiment, we report the first ever measurement of stiffness distribution of the hand dorsum. By using a novel technique of generating stiffness gradients across locations, we improve comfort and performance at the HDI when an exoskeleton is coupled to the hand dorsum.

In the third experiment, we report the first ever measurement of the stiffness and mechanical impedance at the wrist. In a first, we quantify the stiffness and mechanical impedance increase with increasing coupling pressure. However, this increase is more over the bone than over soft tissue rich areas, helping us understand why attaching wearables more tightly to the wrist causes discomfort.

In the fourth experiment, we report the first ever quantification of mechanical impedance and vibrotactile sensitivity over bony and soft locations about the human wrist. We quantify, for the first time ever, how increasing coupling pressure over the wrist changes both the stiffness of the tissue as well as our sensitivity to vibration. We discover in a novel finding, that if we describe the vibrotactile sensitivity threshold in units of mechanical power, then the design of the HDI can be simplified, and parameters such as coupling pressure between the wearable device and the body do not need to be accounted for.

In the fifth and final experiment, we demonstrate a novel approach to tuning comfort and our sensitivity to vibrations applied over the wrist. We change the mechanical impedance of the HDI and demonstrate quantitatively how our ability to perceive an applied vibration reduces as the HDI material gets softer. We also find that the softness of the HDI material correlates directly with the user's perceived comfort.

The coupling between a wearable device and the human body is often characterized as an interaction between the device and the environment. This interaction is considered a source of loss of performance [1, 34, 18] for an otherwise well designed device. This interaction is also a known source of reduced comfort [1, 35]. The traditional approach to addressing these issues focus on the device alone. However, complicated mechanical design makes the device bulky, and advanced feedback control increases power consumption and makes the system bulky. Another approach to designing high performance and comfortable wearable devices is to account for the properties of the human body early in the design process. While this idea makes intuitive sense, little is understood about what properties of the human can be leveraged to simplify design, or how they can be used to improve design. This is the gap in knowledge that we explored in this dissertation. We examined the utility of characterizing mechanical and perceptual properties of the human in improving the performance and comfort of wearable devices coupled to the hand and wrist.

We measured the torque about the MCP joint, and demonstrated for the first time that the torque required to open the fingers is low and scales with finger size and weight. This finding quantifies MCP torque profiles for umimpaired individuals as a normative band. This description of passive extension torque can be used to quantify an important, commonplace and yet qualitative aspect of hand examination in the clinic. We can compare impaired hand function data to the normative torque band to assess hand function after neurological injuries such as spinal cord injuries, strokes and in cases of cerebral palsy. This approach is necessary to quantitatively prescribe treatment and exercise, and for designing devices such as hand exoskeletons.

Hand exoskeletons applying extension torques to the fingers are typically attached to the dorsal aspect of the hand, where they give rise to parasitic reaction pressures responsible for discomfort. Also, the uneven distribution of pressure leads to poor anchoring between the wearable device and the hand. However we could not find any prior literature that explored the hand dorsum to address this issue. By characterizing the first ever map of dorsal stiffness variability across bony and soft tissue regions, we demonstrated how this map is necessary for designing optimal HDI focused on improving both comfort and performance. We concluded from our exploration of hand exoskeletons that to design wearable devices that optimize comfort and performance, measuring the response to applied force over the tissue structures and measuring the torque required about joints are both important.

To understand the role of measuring biomechanical and perceptual characteristics on the design of wearable devices, we embarked on a journey of studying vibrotactile haptic wrist worn devices. Vibrotactile devices rely on coupling to the body to transmit cues to the user. The increasing coupling pressure is known to improve perception, but the relationship between pressure and perception of vibrotactile signals is unknown. Also applying high coupling pressures causes discomfort. However, the comfort as well as the perception of the cues are non identical at all locations about the wrist, but we don't understand why. To examine these issues, we characterized the tissue stiffness and vibrotactile detection thresholds around the wrist. We found that the tissue property of mechanical impedance correlated with the measured displacement detection threshold. Increasing coupling pressure increased the mechanical impedance and decreased the displacement detection threshold. Further we discovered for the first time, that by quantifying detection thresholds in power units we can simplify the relationship, since we find that power required for a stimulus or cue to be detectable by the user is independent of the coupling pressure. This greatly simplifies the design criteria for vibrotactile haptic devices, which until now could not target perceptual thresholds and were always designed to be louder and therefore, consume more power.

This dissertation demonstrates the intuitively appreciated benefits of measuring the human, explicitly. It broadens the goals for wearable device design from improving device performance alone to also include considerations of coupled performance and comfort with the human, early in the design loop. Finally, this work tackles the persistent and challenging question of how we can utilize the measured data from the human to improve the design of the human device interface by sharing methods and metrics as design targets for the wearable engineer.

The Bionic Human, 2050: The design of intelligent Human Device Interfaces

The human device interfaces of the future will come in many different shapes and sizes - From shoes and helmets that can metamorphose their materials to provide performance and comfort, to clothes which change fits based on body type and augment our mobility and strength. In the future, our garments will intelligently sense the appropriate loading paths through the body that would maximize our task performance, enabling us to carry more loads. The same clothes will change subtly to convey our moods depending on features such as the co-contraction of antagonistic muscles. These garments will also serve as communication portals, where people at a distance will be able to interact more personally, and subtle cues will appear more naturalistic. Prostheses will become true extensions of the body, where the human device interface will convey the afferent stimuli perceived at the distal limb back to the brain. These dreams of amalgamating the human with wearable devices will soon become reality as we extend our design thinking to incorporate the human more closely early on in the process of building the human device interface.

BIBLIOGRAPHY

[1] A. Schiele, “Ergonomics of exoskeletons: Subjective performance metrics,” *2009 IEEE/RSJ International Conference on Intelligent Robots and Systems, IROS 2009*, pp. 480–485, 2009.

[2] M. B. Yandell, B. T. Quinlivan, D. Popov, C. Walsh, and K. E. Zelik, “Physical interface dynamics alter how robotic exosuits augment human movement: implications for optimizing wearable assistive devices,” *Journal of NeuroEngineering and Rehabilitation*, vol. 14, no. 1, p. 40, 2017.

[3] A. J. Petron, “Prosthetic Socket Design: From a Multi-Indenter Device for in vivo Biomechanical Tissue Measurement to a Quasi-passive Transtibial Socket Interface,” p. 197, 2016.

[4] R. J. Varghese, G. Mukherjee, R. King, S. Keller, and A. D. Deshpande, “Designing Variable Stiffness Profiles to Optimize the Physical Human Robot Interface of Hand Exoskeletons,” *Proceedings of the IEEE RAS and EMBS International Conference on Biomedical Robotics and Biomechatronics*, vol. 2018-Augus, pp. 1101–1108, 2018.

[5] J. Lindsay, R. J. Adams, and B. Hannaford, “Improving tactile feedback with an impedance adapter,” in *2013 World Haptics Conference, WHC 2013*, 2013.

[6] A. D. Deshpande, N. Gialias, and Y. Matsuoka, “Contributions of intrinsic visco-elastic torques during planar index finger and wrist movements,” *IEEE Transactions on Biomedical Engineering*, vol. 59, no. 2, pp. 586–594, 2012.

[7] J. S. Knutson, K. L. Kilgore, J. M. Mansour, and P. E. Crago, “Intrinsic and extrinsic contributions to the passive moment at the metacarpophalangeal joint,” *Journal of biomechanics*, vol. 33, no. 12, pp. 1675–1681, 2000.

[8] J. M. McNeil, “Current population reports,” *Household Economic Studies. Americans with Disabilities: 1994*, vol. 95, 1997.

[9] P. C. Innis, G. L. Clark, and R. M. Curtis, “Management of the stiff hand,” *Rehabilitation of the Hand*, vol. 2, 1995.

[10] J. W. Brandsma, T. A. R. Schreuders, J. A. Birke, A. Piefer, and R. Oostendorp, “Manual muscle strength testing: intraobserver and interobserver reliabilities for the intrinsic muscles of the hand,” *Journal of Hand therapy*, vol. 8, no. 3, pp. 185–190, 1995.

[11] T. A. R. Schreuders, R. W. Selles, M. E. Roebroeck, and H. J. Stam, "Strength measurements of the intrinsic hand muscles: a review of the development and evaluation of the Rotterdam intrinsic hand myometer," *Journal of Hand Therapy*, vol. 19, no. 4, pp. 393–402, 2006.

[12] Z. M. Li, V. M. Zatsiorsky, and M. L. Latash, "Contribution of the extrinsic and intrinsic hand muscles to the moments in finger joints," *Clinical biomechanics*, vol. 15, no. 3, pp. 203–211, 2000.

[13] P.-H. Kuo and A. D. Deshpande, "Muscle-tendon units provide limited contributions to the passive stiffness of the index finger metacarpophalangeal joint," *Journal of biomechanics*, vol. 45, no. 15, pp. 2531–2538, 2012.

[14] V. Wright and R. J. Johns, "Observations on the measurement of joint stiffness," *Arthritis & Rheumatism: Official Journal of the American College of Rheumatology*, vol. 3, no. 4, pp. 328–340, 1960.

[15] L. E. Edsberg, R. E. Mates, R. E. Baier, and M. Lauren, "Mechanical characteristics of human skin subjected to static versus cyclic normal pressures," *Journal of rehabilitation research and development*, vol. 36, no. 2, 1999.

[16] K. Hagberg, E. Häggström, M. Uden, and R. Brånemark, "Socket versus bone-anchored trans-femoral prostheses: hip range of motion and sitting comfort," *Prosthetics and orthotics international*, vol. 29, no. 2, pp. 153–163, 2005.

[17] T. Lenzi, N. Vitiello, S. M. M. D. Rossi, A. Persichetti, F. Giovacchini, S. Roccella, F. Vecchi, and M. C. Carrozza, "Measuring human-robot interaction on wearable robots: A distributed approach," *Mechatronics*, vol. 21, no. 6, pp. 1123–1131, 2011.

[18] M. Cempini, A. Marzegan, M. Rabuffetti, M. Cortese, and N. Vitiello, "Analysis of relative displacement between the HX wearable robotic exoskeleton and the user's hand," 2014.

[19] A. Petron, J.-F. Duval, and H. Herr, "Multi-Indenter Device for in vivo Biomechanical Tissue Measurement," *IEEE Transactions on Neural Systems and Rehabilitation Engineering*, vol. 25, no. 5, p. 1, 2016.

[20] T. A. Krouskop, R. Williams, M. Krebs, I. Herszkowicz, and S. Garber, "Effectiveness of mattress overlays in reducing interface pressures during recumbency.," *Journal of rehabilitation research and development*, vol. 22, pp. 7–10, jul 1985.

[21] M. J. Belda-Lois, J.M.; Poveda, R.; Vivas, *Analysis of Pressure Distribution and Tolerance Areas for Wearable Robots*. 2008.

[22] Y. Yun, S. Dancausse, P. Esmatloo, A. Serrato, C. A. Merring, P. Agarwal, and A. D. Deshpande, "Maestro: An EMG-driven assistive hand exoskeleton for spinal cord in-

jury patients," in *Robotics and Automation (ICRA), 2017 IEEE International Conference on*, pp. 2904–2910, IEEE, 2017.

[23] P. Agarwal, J. Fox, Y. Yun, M. K. OMalley, and A. D. Deshpande, "An index finger exoskeleton with series elastic actuation for rehabilitation: Design, control and performance characterization," *The International Journal of Robotics Research*, vol. 34, no. 14, pp. 1747–1772, 2015.

[24] R. J. Varghese, "Physical Human-Robot Interaction (pHRI) Interfaces: A Simulation Based Design Method," Master's thesis, The University of Texas at Austin, 2017.

[25] F. Udwadia and R. E. Kalaba, "What is the General Form of the Explicit Equations of Motion for Constrained Mechanical Systems?," *Journal of Applied Mechanics*, vol. 69, no. 3, p. 335, 2002.

[26] T. Feix, J. Romero, H. B. Schmiedmayer, A. M. Dollar, and D. Kragic, "The GRASP Taxonomy of Human Grasp Types," *IEEE Transactions on Human-Machine Systems,*, 2015.

[27] A. Mujibiya, X. Cao, D. S. Tan, D. Morris, S. N. Patel, and J. Rekimoto, "The sound of touch," in *Proceedings of the 2013 ACM international conference on Interactive tabletops and surfaces - ITS '13*, 2013.

[28] S. Portnoy, Z. Yizhar, N. Shabshin, Y. Itzchak, A. Kristal, Y. Dotan-Marom, I. Siev-Ner, and A. Gefen, "Internal mechanical conditions in the soft tissues of a residual limb of a trans-tibial amputee," *Journal of Biomechanics*, 2008.

[29] F. Pece, J. J. Zarate, V. Vechev, N. Besse, O. Gudozhnik, H. Shea, and O. Hilliges, "MagTics," in *Proceedings of the 30th Annual ACM Symposium on User Interface Software and Technology - UIST '17*, 2017.

[30] K. A and L. A, "Mechanical Behaviour of Skin: A Review," *Journal of Material Science & Engineering*, 2016.

[31] D. G. Pelli, "The videotoolbox software for visual psychophysics: Transforming numbers into movies," *Spatial vision*, vol. 10, no. 4, pp. 437–442, 1997.

[32] D. H. Brainard, "The psychophysics toolbox," *Spatial vision*, vol. 10, no. 4, pp. 433–436, 1997.

[33] M. Kleiner, D. Brainard, and D. Pelli, "What's new in psychtoolbox-3?," 2007.

[34] P. Agarwal, J. Fox, Y. Yun, M. K. O'Malley, and A. D. Deshpande, "An index finger exoskeleton with series elastic actuation for rehabilitation: Design, control and performance characterization," *The International Journal of Robotics Research*, 2015.

[35] A. M. Gcorgarakis, R. Stampfli, P. Wolf, R. Riener, and J. E. Duartc, "A Method for Quantifying Interaction Forces in Wearable Robots," *Proceedings of the IEEE RAS*

and EMBS International Conference on Biomedical Robotics and Biomechatronics, vol. 2018-August, pp. 789–794, 2018.

[36] H.-Y. Chen, J. Santos, M. Graves, K. Kim, and H. Z. Tan, "Tactor localization at the wrist," in *Haptics: Perception, Devices and Scenarios* (M. Ferre, ed.), (Berlin, Heidelberg), pp. 209–218, Springer Berlin Heidelberg, 2008.

[37] H. C. Fischer, K. M. Triandafilou, K. O. Thielbar, J. M. Ochoa, E. D. C. Lazzaro, K. A. Pacholski, and D. G. Kamper, "Use of a Portable Assistive Glove to Facilitate Rehabilitation in Stroke Survivors with Severe Hand Impairment," *IEEE Transactions on Neural Systems and Rehabilitation Engineering*, vol. 24, no. 3, 2016.

[38] A. Biswas, M. Manivannan, and M. A. Srinivasan, "Vibrotactile Sensitivity Threshold: Nonlinear Stochastic Mechanotransduction Model of the Pacinian Corpuscle," *IEEE Transactions on Haptics*, vol. 8, no. 1, pp. 102–113, 2015.

[39] P. Agarwal, R. R. Neptune, and A. D. Deshpande, "A Simulation Framework for Virtual Prototyping of Robotic Exoskeletons.," *Journal of biomechanical engineering*, vol. 138, no. 6, p. 061004, 2016.

[40] R. A. Bos and C. J. Haarman, "A structured overview of trends and technologies used in dynamic hand orthoses," *Journal of NeuroEngineering and Rehabilitation*, vol. 13, no. 1, p. 62, 2016.

[41] P. Heo, G. M. Gu, S. jin Lee, K. Rhee, and J. Kim, "Current hand exoskeleton technologies for rehabilitation and assistive engineering," *International Journal of Precision Engineering and Manufacturing*, vol. 13, no. 5, pp. 807–824, 2012.

[42] L. Roberson and D. J. Giurintano, "Objective measures of joint stiffness," *Journal of Hand Therapy*, vol. 8, no. 2, pp. 163–166, 1995.

[43] A. Unsworth, P. M. A. Bey, and I. Haslock, "Stiffness in the metacarpo-phalangeal joints of young adults," *Clinical Physics and Physiological Measurement*, vol. 2, no. 2, p. 123, 1981.

[44] D. G. Kamper, R. L. Harvey, S. Suresh, and W. Z. Rymer, "Relative contributions of neural mechanisms versus muscle mechanics in promoting finger extension deficits following stroke," *Muscle & Nerve: Official Journal of the American Association of Electrodiagnostic Medicine*, vol. 28, no. 3, pp. 309–318, 2003.

[45] J. D. Given, J. P. Dewald, and W. Z. Rymer, "Joint dependent passive stiffness in paretic and contralateral limbs of spastic patients with hemiparetic stroke.," *Journal of Neurology, Neurosurgery & Psychiatry*, vol. 59, no. 3, pp. 271–279, 1995.

[46] B. Quinlivan, A. Asbeck, D. Wagner, T. Ranzani, S. Russo, and C. J. Walsh, "Force Transfer Characterization of a Soft Exosuit for Gait Assistance," *Volume 5A: 39th Mechanisms and Robotics Conference*, p. V05AT08A049, 2015.

[47] E. R. Kandel, *Principles of Neural Science, Fifth Edition.* Principles of Neural Science, McGraw-Hill Education, 2013.

[48] E. W. Obropta and D. J. Newman, *A comparison of human skin strain fields of the elbow joint for mechanical counter pressure space suit development.*

[49] H. Culbertson, S. B. Schorr, and A. M. Okamura, "Annual Review of Control, Robotics, and Autonomous Systems Haptics: The Present and Future of Artificial Touch Sensation," *Annu. Rev. Control Robot. Auton. Syst. 2018*, vol. 1, pp. 385–409, 2018.

[50] E. Sandford, Y. Chen, I. Hunter, G. Hillebrand, and L. Jones, "Capturing skin properties from dynamic mechanical analyses," *Skin Research and Technology*, vol. 19, no. 1, pp. 339–348, 2013.

[51] K. Allan, T. White, L. Jones, J. Merlo, E. Haas, G. Zets, and A. Rupert, "GETTING THE BUZZ: WHAT'S NEXT FOR TACTILE INFORMATION DELIVERY?," *PROCEEDINGS of the HUMAN FACTORS and ERGONOMICS SOCIETY.*

[52] R. Maiti, L. C. Gerhardt, Z. S. Lee, R. A. Byers, D. Woods, J. A. Sanz-Herrera, S. E. Franklin, R. Lewis, S. J. Matcher, and M. J. Carré, "In vivo measurement of skin surface strain and sub-surface layer deformation induced by natural tissue stretching," *Journal of the Mechanical Behavior of Biomedical Materials*, 2016.

[53] T. Soneda and K. Nakano, "Investigation of vibrotactile sensation of human fingerpads by observation of contact zones," 2009.

[54] R. Lukdstr&, "LOCAL VIBRATIONS-MECHANICAL IMPEDANCE OF THE HUMAN HAND'S GLABROUS SKIN," tech. rep.

[55] R. Hoffmann, V. Vala Valgeirsdóttir, ·. Ómar, I. Jóhannesson, R. Unnthorsson, and ·. Á. Kristjánsson, "Measuring relative vibrotactile spatial acuity: effects of tactor type, anchor points and tactile anisotropy," *Experimental Brain Research*, vol. 236, pp. 3405–3416, 2018.

[56] K. . Sofia, *Mechanical and Psychophysical Studies of Surface Wave Propagation during Vibrotactile Stimulation.* PhD thesis, MIT, 2012.

[57] K. O. Sofia and L. Jones, "Mechanical and psychophysical studies of surface wave propagation during vibrotactile stimulation," *IEEE Transactions on Haptics*, vol. 6, no. 3, pp. 320–329, 2013.

[58] M. D. Hill and G. Niemeyer, "Real-time estimation of human impedance for haptic interfaces," *Proceedings - 3rd Joint EuroHaptics Conference and Symposium on Haptic Interfaces for Virtual Environment and Teleoperator Systems, World Haptics 2009*, pp. 440–445, 2009.

[59] S. E. Robbins, A. Hanna, and L. A. Jones, "Sensory Attenuation Induced by Modern Athletic Footwear," Tech. Rep. 4, 1988.

[60] L. A. Jones and N. B. Sarter, "Tactile Displays: Guidance for Their Design and Application," 2008.

[61] B. Bordoni and M. Simonelli, "The Awareness of the Fascial System.," *Cureus*, vol. 10, no. 10, p. e3397, 2018.

[62] A. Moscatelli, M. Bianchi, A. Serio, A. Terekhov, V. Hayward, M. O. Ernst, and A. Bicchi, "The Change in Fingertip Contact Area as a Novel Proprioceptive Cue.," *Current biology : CB*, vol. 26, no. 9, pp. 1159–1163, 2016.

[63] L. R. Manfredi, A. T. Baker, D. O. Elias, J. F. Dammann III, M. C. Zielinski, V. S. Polashock, and S. J. Bensmaia, "The Effect of Surface Wave Propagation on Neural Responses to Vibration in Primate Glabrous Skin," *PLoS ONE*, vol. 7, no. 2, p. 31203, 2012.

[64] K. O. Johnson, "The roles and functions of cutaneous mechanoreceptors," *Current Opinions in Neurobiology*, vol. 11, pp. 455–461, 2001.

[65] S. D. Novich and D. M. Eagleman, "Using space and time to encode vibrotactile information: toward an estimate of the skin's achievable throughput," *Experimental Brain Research*, vol. 233, pp. 2777–2788, 2015.

[66] A. R. Lam, "Vibrotactile Pattern Recognition on the Torso with One and Two Dimensional Displays," *Mechanical Engineering*, pp. 1–28, 2006.

[67] E. Biddiss and T. Chau, "Upper-Limb Prosthetics: Critical Factors in Device Abandonment," *American Journal of Physical Medicine & Rehabilitation*, vol. 86, pp. 977–987, jan 2007.

[68] M. Azadi and L. A. Jones, "Vibrotactile actuators: Effect of load and body site on performance," *IEEE Haptics Symposium, HAPTICS*, pp. 351–356, 2014.

[69] L. A. Jones and D. A. Held, "Characterization of Tactors Used in Vibrotactile Displays," *Journal of Computing and Information Science in Engineering*, vol. 8, no. 4, p. 044501, 2008.

[70] T. J. Moore, J. R. Mundie, T. J. Moobe, and J. R. Munme, "Measurement of Specific Mechanical Impedance of the Skin: Effects of Static Force, Site of Stimulation, Area of Probe, and Presence of a Surround," *Citation: The Journal of the Acoustical Society of America*, vol. 52, p. 61901, 1972.

[71] M. Wiertlewski and V. Hayward, "Mechanical behavior of the fingertip in the range of frequencies and displacements relevant to touch," 2012.

[72] V. G. Macefield, “Physiological characteristics of low-threshold mechanoreceptors in joints, muscle and skin in human subjects,” *Clinical and Experimental Pharmacology and Physiology*, vol. 32, pp. 135–144, jan 2005.

[73] E. Pezent, A. Israr, M. Samad, S. Robinson, P. Agarwal, H. Benko, and N. Colonnese, “Submitted - Tasbi: Multisensory Squeeze and Vibrotactile Wrist Haptics for Augmented and Virtual Reality,” in *IEEE World Haptics Conference (WHC)*, 2019.

[74] A. Petron, “We Suck At Attaching Objects To People,” 2015.